HIGH DETECTIVE QUANTUM EFFICIENCY ELECTRONIC PORTAL IMAGING DEVICES BASED ON SEGMENTED CRYSTALLINE SCINTILLATORS AND MERCURIC IODIDE PHOTOCONDUCTORS

by

Yi Wang

A dissertation submitted in partial fulfillment
of the requirements for the degree of
Doctor of Philosophy
(Biomedical Engineering)
in The University of Michigan
2009

Doctoral Committee:

Professor Larry E. Antonuk, Co-Chair
Emeritus Professor W. Leslie Rogers, Co-Chair
Professor Roy Clarke
Professor Neal H. Clinthorne

Be prepared when opportunity knocks.

Dedicated to my parents and my wife –
my loved ones who are always supporting me.

ACKNOWLEDGEMENTS

I would like to first express my profound gratitude to my advisor, Professor Larry E Antonuk for his supervision and support in the past seven years. His dedication, energy, professionalism and enthusiasm have strongly motivated me to push this project, as well as my academic career forward. Also, I would thank my co-chair Professor Leslie Rogers, as well as committee members Professor Roy Clarke and Professor Neal Clinthorne, for their significant efforts in helping me to improve this dissertation.

My great appreciation goes to my mentors, Dr. Youcef El-Mohri and Dr. Qihua Zhao, who have made significant contributions to the success of this project. I also thank my colleagues, Dr. Amit Sawnt, Dr. Hong Du, Mike Yeakey, Alan Young, Chuck Martelli, Martin Koniczek and John McDonald for their academic and technical support. I greatly appreciate our collaborators at Saint-Gobain Crystals, Dr. Mike Mayhugh, Dr. Peter Menge and Lou Perna for producing the segmented scintillators. I also thank Dr. Aldo Badano at the U.S. FDA for providing the MANTIS code and Dr. Jeffrey Fessler at the EECS department of UM for providing the algorithm for CBCT reconstruction.

I also want to thank my parents for their physical, fiscal and emotional support in the three decades. Finally, I give my greatest gratitude to my wife Ying, who is always standing behind me in time of hardship, challenge, success and pleasure. The love and support from my family are my most valuable assets.

TABLE OF CONTENTS

LIST OF FIGURES

Figure

LIST OF TABLES

Table

LIST OF APPENDICES

APPENDIX

GLOSSARY

Symbol/Abbreviation	Description
AED	Absorbed energy distribution
AMFPI	Active matrix, flat panel imager
a-Si:H	hydrogenated amorphous silicon
BGO	Bismuth Germanate
CBCT	Cone-beam computed tomography
cGy	Centigray
CNR	Contrast to noise ratio
CRT	Conformal radiation therapy
CT	Computed tomography
CTN	CT number
CsI:Tl	Thallium-doped cesium iodide
DQE	Detective quantum efficiency
DQE_{RAD}	Radiation DQE
EPD	Electric pulse distribution
EPID	Electronic portal imaging device
GOS	Gd_2O_2S:Tb, terbium-activated gadolinium oxysulfide
HgI_2	Mercuric iodide

Symbol/Abbreviation	Description
HU	Hounsfield unit
I	Swank factor
I_{ELE}	Electric Swank factor
I_{OPT}	Optical Swank factor
I_{RAD}	Radiation Swank factor
IGRT	Image-guided radiation therapy
IMRT	Intensity-modulated radiation therapy
In	Intensity signal
kV	Kilovoltage
l	Line integral
LINAC	Linear accelerator
LSF	Line spread function
M_i	i^{th} moment of a distribution
MTF	Modulation transfer function
MTF_{RAD}	Radiation MTF
MU	Monitor unit
MV	Megavoltage
NNPS	Normalized NPS
$NNPS_{RAD}$	Normalized radiation NPS
NPS	Noise power spectrum
NPS_{RAD}	Radiation NPS

Symbol/Abbreviation	Description
OPD	Optical pulse distribution
P(x)	A distribution
PHD	Pulse height distribution
PIB	Particle in binder
PVD	Physical vapor deposition
QE	Quantum efficiency
RED	Relative electron density
SNR	Signal to noise ratio

CHAPTER 1

INTRODUCTION

I. OVERVIEW

The central aim of this dissertation project is to develop high-efficiency electronic portal imaging devices (EPIDs) based on active matrix, flat-panel imager (AMFPI) technology. This work is motivated by the strong desire in the field of radiation therapy to obtain soft-tissue information in the radiation treatment room. Such information is important for assuring accurate delivery of the high-energy radiation to the tumor volume while sparing surrounding normal tissues.[1]

In order to assist the reader in understanding the main context of this work, background information on external photon beam therapy and megavoltage (MV) x-ray imaging is reviewed in this chapter. After identifying the motivations and strategies to significantly improve the detective quantum efficiency (DQE) for AMFPI-based EPIDs, the various approaches to realize such strategies are summarized. Finally, the organization of this dissertation is presented.

II. PHOTON BEAM RADIOTHERAPY

Since their initial discovery by Dr. Röntgen in 1895,[2] X rays have been widely used in many medical applications. X rays at keV energies are used in diagnostic imaging procedures, such as mammography, radiography, fluoroscopy, angiography, and computed tomography (CT). X rays (and γ rays) at MeV energies are used for cancer treatment. Such radiation can be delivered either by implantation of radioactive sources (i.e., brachytherapy)[3] or by an external x-ray source (i.e., external photon beam therapy). In addition, MV x-ray beams can be used to image patients in the radiation treatment room, so as to assure accurate execution of the planned treatment.[1]

External photon beam therapy is commonly performed using medical linear accelerators (LINACs), which can produce X rays up to 25 MeV. Modern medical LINACs use accelerated, high-energy electrons to hit a heavy-metal target to generate bremsstrahlung x-ray beams. Before exiting the LINAC, such beams are attenuated by means of a flattening filter to achieve a flat and symmetric beam profile.

Historically, medical LINACs have been used to deliver collimated photon beams with a homogenous intensity from different angles (i.e., ports) focusing on the tumor volume. In these conventional treatments, the normal tissues surrounding the tumor also receive a significant amount of dose. In order to minimize radiation exposure to normal tissues, advanced treatment techniques, such as 3D conformal radiation therapy (CRT) and intensity-modulated radiation therapy (IMRT), have been employed to precisely conform the dose distribution to the 3D shape of the tumor volume.[4-6] The accurate

execution of these conformal and modulated treatment plans requires setting up the patient precisely to the planned position prior to the treatment, and monitoring patient motion and dose delivery during the treatment.

III. MEGAVOLTAGE X-RAY IMAGING

In addition to therapeutic applications, MV X rays can also be used to localize the treatment volume immediately prior to the treatment so as to accurately set up the patient to the planned position (*localization imaging*), and to verify the dose delivery during the treatment (*verification imaging*).[1] Such localization and verification images, referred to as *portal images*, can be obtained with the treatment beam using portal imagers, such as portal films and EPIDs.

A. PORTAL FILMS AND EARLY EPIDS

Historically, portal imaging has been performed using film cassettes. Conventional portal film systems consist of a film sandwiched between a front metal plate and a rear metal or plastic plate, whereas enhanced contrast localization systems consist of a film sandwiched between two phosphor screens along with a front metal plate.[1] After an x-ray exposure, the film is extracted, developed in a processing room, and viewed on a back-illuminated viewing box. Portal films provide images of clinical value, and thus were previously considered as the gold standard for portal imaging. However, portal films have to be removed from the treatment room for development. During this period, the patient may move, making the imaging information less useful.

In order to provide real-time portal imaging with electronic readout, EPIDs have been explored since the 1950s. Two early examples of successful EPIDs are based on camera systems and a scanning matrix system.[7-15] The camera-based systems utilize a copper plate and a phosphor screen to convert radiation energy to light photons. The light emerging from the screen is reflected by a mirror, a fraction of which enters the lens of a camera, generating a video signal. This signal is digitalized, processed and stored on a host computer. A major disadvantage of these EPIDs is that only ~0.01% to 0.1% of the light emerging from the phosphor screen can be detected. This loss of quanta causes degradation in image quality that cannot be recovered through amplification. In addition, the imaging performance of camera-based systems is degraded by glare.[1, 16] The scanning matrix system consists of an overlying plastoferrite plate and a matrix of 256 × 256 ionization cells filled with a liquid medium that generates ions when irradiated. Compared to the camera-based system, this system is much more compact in size, approaching the dimension of film cassettes. However, constrained by the recombination time of the ions in the liquid, this system can only collect imaging signal generated ~0.5 seconds prior to readout – a period that is much shorter than the time required to scan the whole matrix (at least 1.5 seconds). As a result of this signal loss, the DQE of this system is limited to ~0.5%.

B. AMFPI-BASED EPIDS

1. Overview of AMFPI technology

AMFPIs, employing large-area, hydrogenated amorphous silicon (a-Si:H) thin-film transistor (TFT) arrays, were initially developed in the 1980s.[17-20] Since then, AMFPIs

have been widely used for mammography, radiography, fluoroscopy, angiography and radiotherapy imaging. More recently, AMFPIs have been introduced for volumetric image acquisition such as tomosynthesis and cone-beam CT.

In general, an AMFPI system consists of four components: (1) an x-ray detector that converts radiation energy to secondary imaging quanta; (2) a large area, pixelated flat-panel array that can collect the imaging signal emerging from the x-ray detector; (3) an electronic acquisition interface that controls the image acquisition, extracts signal from the flat-panel array and converts the analog signal to a digital format; and (4) a host computer that sends commands to and receives the digital data from the acquisition interface, as well as processes, displays and stores the digital images.[16]

Based on how the radiation energy is converted to secondary imaging quanta, AMFPIs can be categorized into two groups – indirect and direct detection AMFPIs.[16] An indirect detection MV AMFPI utilizes a scintillating detector (typically, a scintillator covered by a metal plate) to convert radiation energy to optical photons. A fraction of the light escapes from the scintillator and enters the underlying, indirect detection flat-panel array. Each pixel of the array consists of an a-Si:H photodiode (also serving as signal storage capacitor) gated by an a-Si:H TFT switch. Optical photons detected by the photodiode generate electrical signal that is temporarily stored in the photodiode. For a direct detection MV AMFPI, a photoconductive detector (a photoconductor covered by a metal plate) is used to convert radiation energy directly into electron-hole pairs. Typically, the photoconductor is coated onto a direct detection flat-panel array

comprising a storage capacitor at each pixel. Electron-hole pairs created by incident radiation are swept by an externally applied electric field across the photoconductor. This induces electrical signal that is temporarily stored in the storage capacitor, which is gated by a pixel TFT. In both indirect and direct detection arrays, the gate and drain contacts of the pixel TFTs are connected to gate lines and data lines, respectively. During radiation signal collection, the TFTs are made non-conducting (i.e., off state). During readout, the TFTs are made conducting (i.e., on state), allowing pixel signal to be read out via the data lines. The signal is then amplified, digitized, and stored on the host computer. For this dissertation work, the electronic interface used for image acquisition corresponds to the 3rd generation of our fully customized acquisition system – referred to as the G3 system.[21]

2. Performance metrics for AMFPIs

The performance of x-ray imaging systems, such as AMFPIs, can be quantitatively evaluated using observer independent metrics, including modulation transfer function (MTF), noise power spectrum (NPS) and detective quantum efficiency (DQE). These metrics are functions of spatial frequency (f). MTF, as a measure of spatial resolution, is determined from the 1D Fourier transform of the line spread function (LSF). MTF is normalized to 1 at zero spatial frequency and typically falls off at higher frequencies. NPS represents the noise properties of an imaging system. The magnitude of NPS depends on many factors including the number of incident and interacting X rays, Swank noise in the converter, and MTF. For example, systems with more stochastic spatial spreading results in stronger pixel-to-pixel noise correlations, which in turn leads to a

steeper drop of NPS as a function of spatial frequency.[22] DQE, a widely accepted metric for overall performance evaluation of a system, represents the ability of the system to transfer signal-to-noise ratio (SNR) information from the input to the output. Quantitatively, DQE can be determined from:[23]

$$DQE(f) = \frac{S^2 \times MTF^2(f)}{\bar{q}_0 \times NPS(f)} \tag{1.1}$$

where S is the average pixel signal and $\bar{q}_0$ is the incident x-ray fluence (i.e., the number of incident X rays per unit area of the x-ray detector). In the absence of secondary effects (i.e., generation and transport of the secondary imaging quanta), radiation DQE (DQE_{RAD}) can be obtained using:

$$DQE_{RAD}(f) = \frac{S_{RAD}^2 \times MTF_{RAD}^2(f)}{\bar{q}_0 \times NPS_{RAD}(f)} \tag{1.2}$$

where S_{RAD}, MTF_{RAD} and NPS_{RAD} are signal, MTF and NPS resulting from radiation transport in the x-ray detector.

The Swank factor (I) is a quantitative representation of Swank noise, which corresponds to the variation in the pulse height distribution (PHD) – a distribution of the number of detected secondary imaging quanta for each interacting X ray. The Swank factor may be considered to consist of a radiation component and a secondary component, both of which degrade DQE. The radiation Swank factor (I_{RAD}) is determined from the absorbed energy distribution (AED) – a distribution of the amount of energy absorbed in the x-ray converter for each interacting X ray. In this representation, I_{RAD} includes the contribution due to the polyenergetic nature of the incident beam. The secondary Swank factor (optical Swank factor, I_{OPT}, for indirect

detection and electric Swank factor, I_{ELE}, for direct detection) is calculated from the secondary pulse distribution (optical pulse distribution, OPD, for indirect detection and electrical pulse distribution, EPD, for direct detection). OPD (EPD) is a distribution of the number of optical photons (electrons-hole pairs) detected for each unit absorbed energy in the scintillator (photoconductor). The Swank factors (i.e., I, I_{RAD}, I_{OPT} and I_{ELE}) are calculated using:[24]

$$I = \frac{M_1^2}{M_0 \times M_2}, \tag{1.3}$$

where M_i is the *ith* order moment of the distribution (i.e., PHD, AED, OPD and EPD). M_i is obtained from:[25]

$$M_i = \int x^i \times P(x)\, dx. \tag{1.4}$$

where $P(x)$ corresponds to the distribution. With such a definition, a higher Swank factor indicates a lower Swank noise.

Quantum efficiency (QE) corresponds to the fraction of incident X rays that deposit radiation energy in the x-ray converter. In the absence of electronic noise and noise power aliasing, at zero spatial frequency, DQE can be expressed as:[24, 26]

$$DQE = QE \times I, \tag{1.5}$$

and DQE_{RAD} can be expressed as:[27]

$$DQE_{RAD} = QE \times I_{RAD}. \tag{1.6}$$

3. Conventional AMFPI-based EPIDs

Since the early 2000s, AMFPI-based EPIDs have become the gold standard for portal imaging. Presently, major LINAC vendors all offer EPIDs based on indirect detection AMFPIs. Examples of the latest commercial EPIDs include PortalVision aS1000 from Varian Medical Systems, OPTIVUE 1000 from Siemens Healthcare and iViewGT from Elekta. The flat-panel array used in the Varian EPID has 1024 × 768 pixels with a pixel pitch of 0.392 mm, resulting in an active area of ~40 × 30 cm^2. [28] The arrays used in the Siemens and Elekta EPIDs both have 1024 × 1024 pixels with a pixel pitch of 0.4 mm, leading to an active area of ~40 × 40 cm^2.[29-31] These commercial EPIDs (referred to as *conventional EPIDs* in this dissertation) utilize a phosphor screen detector, which consists of a Gd_2O_2S:Tb (GOS) screen and an overlying 1 mm thick metal plate (e.g., copper), to indirectly detect incident X rays. The GOS screen has properties similar to the Lanex Fast B screen (Eastman Kodak, Rochester) with a surface density of ~133 mg/cm^2 and a thickness of ~0.36 mm.

The performance of conventional EPIDs is demonstrated in the present work as well as in previous studies[23, 32] by an AMFPI prototype employing a phosphor screen detector (a Lanex Fast B screen and a 1 mm thick copper plate) and a Cyclops II flat-panel array (512 × 512 pixels with a pixel pitch of 0.508 mm). Details of the general structure and operation of the array can be found in a previous publication.[23]

C. VOLUMETRIC IMAGING BASED ON AMFPI TECHNOLOGY

The last decade witnessed the rapid development of image-guided radiation therapy (IGRT) technology, which aims at providing precise patient position information in the treatment room so as to assure accurate execution of advanced treatment plans for 3D CRT and IMRT. For this purpose, a variety of 3D imaging techniques, involving non-radiation[33-36] and radiation imaging modalities,[37-46] have been extensively examined. In particular, both kV and MV AMFPIs have been investigated for providing cone-beam CT (CBCT) images in the treatment room.

The last few years have witnessed the commercialization and clinical implementation of on-board kV imaging systems, which consists of a kV x-ray source and a kV AMFPI orthogonally mounted to the treatment gantry. This type of systems can rotate with the gantry, acquiring CBCT images with soft-tissue information using a dose of a few cGy.[47-49] Alternatively, CBCT images can be acquired using the MV treatment beam.[39, 44] Compared to kV, the MV technique has distinct advantages. For example, MV CBCT can be performed using the treatment beams and the already-installed EPID, requiring no additional equipment. Moreover, the MV imaging system shares the same isocenter with the treatment system, eliminating the need for additional geometric calibration.[50] Furthermore, MV CBCT images are almost free of streak artifacts (present in the vicinity of metal objects such as dental implant) and less affected by radiation scattering, both of which can significantly degrade the quality of kV CBCT images.[39, 51, 52] Finally, MV CT numbers extracted from the reconstructed images are directly related to the electron

density of the treated volume, and thus can be used for more accurate dose calculations [39, 53-55] and inhomogeneity corrections.[56]

Despite these advantages, tissue contrast is much lower for MV beams compared to kV beams, due to the high penetration of MV X rays. Moreover, the phosphor screen detector used in conventional EPIDs can only utilize ~2% of the incident radiation for a 6 MV photon beam (compared to up to ~80% for kV AMFPIs). Consequently, MV CBCT requires higher dose for soft-tissue visualization. For example, Groh *et al.* reported the use of a dose of 32 cGy to delineate ~4% density differences.[57] Also, Morin *et al.* reported using 14.4 MU to obtain pelvic images with visible soft tissues (*e.g.*, prostate, rectum, fat, and muscle),[39] and 9 MU to obtain pelvic images with sufficient soft-tissue information to guide 3D positioning.[54]

IV. MOTIVATIONS AND STRATEGIES TO IMPROVE EPID DQE

Although conventional AMFPI-based EPIDs have largely replaced portal films and have become the new gold standard for portal imaging, their DQE is relatively low at radiotherapy energies (~1% at 6 MV) due to the very low QE (~2% at 6 MV). This low DQE limits the performance of portal imaging and makes it impractical to obtain soft-tissue information through MV CBCT at clinically acceptable doses (e.g., a few cGy). In order to circumvent these limitations, it is necessary to significantly improve DQE for EPIDs.

DQE depends upon QE, MTF and NPS in the following manner:

$$DQE(f) \propto QE \times \frac{MTF^2(f)}{NPS(f)}, \tag{1.7}$$

where f is spatial frequency. In order to significantly improve DQE, the most efficient strategy is to greatly increase detector QE, while maintaining or improving MTF and limiting additional noise contributions (e.g., Swank noise). For these reasons, a number of high-efficiency detector approaches have been investigated by different research groups.

A. THICK, SEGMENTED PHOSPHORS

The most straightforward way to increase the QE for conventional EPIDs is to increase the thickness of the phosphor screen. However, increasing screen thickness would result in degraded MTF due to increased lateral spreading of optical photons and reduced Swank factor due to increased variation of collection efficiency for light generated at different depths in the screen. Indeed, after decades of implementation, the current configuration of the phosphor screen detector has been proven to provide optimal DQE performance.

The loss of spatial resolution for thicker phosphors can be limited through the use of a segmented geometry – in which septal walls are used to segment an x-ray converter (e.g., phosphor) into a 2D matrix of individual elements. Sawant *et al*. evaluated segmented phosphors up to 1.7 mm thick.[58] Compared to conventional EPIDs, prototype EPIDs employing these segmented phosphors showed higher QE (up to 3 times) and x-ray sensitivity, as well as similar MTF. However, the increase in QE was mitigated by a

large reduction in Swank factor, leading to no improvement in DQE. While the concept of segmentation has been shown to be successful for preserving spatial resolution, the observed reduction in optical Swank factor is detrimental, but could be overcome by substituting the granular phosphor with more transparent crystalline scintillators.

B. THICK PHOTOCONDUCTORS

Direct detection EPIDs utilizing thick photoconductors have also been examined. In photoconductors, the absorbed radiation energy is converted directly to electron-hole pairs, which are swept by an externally applied electric field, resulting in limited lateral spreading and reduced Swank noise – thereby minimizing degradation in DQE. A photoconductor material that has been commercially used for diagnostic imaging is amorphous selenium (a-Se), which can be made up to ~1 mm thick. While investigational EPIDs based on ~0.5 mm thick a-Se photoconductors showed DQE values comparable to that of conventional EPIDs,[59-62] the availability of a-Se layers much thicker than 1 mm suitable for portal imaging is hampered by manufacturing difficulties. Our group has investigated an alternative photoconductor material, polycrystalline mercuric iodide (HgI_2), which provides a higher mass density of 6.36 cm/g^3 (4.27 cm/g^3 for a-Se) and higher effective atomic number of 66 (34 for a-Se), resulting in higher x-ray stopping power. More importantly, HgI_2 only requires an electric field of ~0.5 to 1V/μm for efficient signal collection,[63] which is over an order of magnitude lower than that required for a-Se.[62] In addition, HgI_2 photoconductors can be made much thicker while requiring lower bias voltage than a-Se.

C. THICK, SEGMENTED CRYSTALLINE SCINTILLATORS

The use of segmented crystalline scintillators is a highly promising alternative for providing significantly improved DQE at radiotherapy energies. Compared to phosphors, crystalline scintillators are much more transparent, offering the possibility to greatly reduce the optical Swank noise. Compared to photoconductors, much thicker bulk crystal layers (e.g., over 10 mm) can be grown with high quality. In addition, using segmented configurations, lateral optical spreading due to the use of thick scintillators can be significantly limited, or even eliminated. As a result of these favorable properties (greatly increased QE, preserved or improved MTF, as well as increased optical Swank factor), EPIDs employing thick, segmented crystalline scintillators could provide significantly improved DQE (see Eq. 1.7).

Table 1.1 summarizes the physical properties of several crystalline scintillator materials that have been investigated, or hold potential, for megavoltage x-ray imaging.[64-66] While CsI:Tl has been widely examined for radiation detection, the non-alkali scintillators have higher mass density, resulting in higher QE per unit thickness.

Table 1.1. Physical properties of crystalline scintillators that are of interest for MV radiation detection.[64, 67-71]

	Mass Density (g/cm^3)	Light yield (photons/ keV)	Peak emission wavelength (nm)	Refractive index at emission peak	Primary decay time (ns)
CsI:Tl	4.51	54	550	1.79	1000
$CaWO_4$	6.10	16	420	1.93	9000
$ZnWO_4$	7.87	29	480	2.10	21000
$CdWO_4$	7.90	12-15	475	2.30	14000
$Bi_4Ge_3O_{12}$ (BGO)	7.13	8-10	480	2.15	300

1D linear arrays of segmented BGO and $ZnWO_4$ scintillators were initially developed in the early 1990s for MV CT application.[72, 73] In addition, a 1D arc array of segmented $CdWO_4$ scintillator was also reported.[74-76] The first 2D matrix of segmented CsI:Tl scintillator was built in 1998.[77-79] This scintillator was 10 mm thick and consisted of 200 × 150 elements with an element-to-element pitch of 3 mm (resulting in an active area of 60 × 45 cm^2). These elements were separated by 0.3 mm thick epoxy resin walls coated with titanium dioxide (TiO_2). A TV camera-based EPID employing this scintillator, demonstrating a QE of ~18% at 6 MV, could delineate small objects (~2 mm) with a low contrast of ~1.3% using a dose of only ~1 cGy.[77] As an initial investigation, our group developed a 2 mm thick segmented CsI:Tl scintillator matrix, which has 40 × 40 elements with an element-to-element pitch of 1 mm.[80] The scintillating crystals were separated by 0.05 mm thick tungsten walls. An AMFPI-based EPID employing this scintillator offered a QE of ~7%. However, this approach was not further pursued since it is extremely difficult to produce such a tungsten matrix with good quality over a large area.

The segmented scintillators examined in this dissertation study were produced at SGC (Hiram, OH) using a proprietary assembly technique. These segmented scintillators consist of a 2D matrix of scintillating crystals (e.g., CsI:Tl) separated by septal walls (thin reflectors glued to the crystals). Figure 1.1 schematically illustrates a representative part of an EPID employing a segmented scintillating detector (segmented scintillators with an overlying Cu plate). Using optically opaque septal walls, the optical photons generated in a scintillator element can only be detected by the underlying array pixel, preventing MTF and DQE degradation induced by lateral optical spreading. However,

since the treatment beams typically employ a divergent point source, the performance of thick, segmented scintillators can be constrained by spatial resolution degradation due to off-axis radiation, where primary radiation is attenuated by multiple elements. A strategy to overcome this limitation involves the implementation of a focused geometry,[80] allowing scintillator elements to be focused towards the radiation source. Although scintillators with such a high degree of complexity are presently very difficult to fabricate, it might become feasible in the future with improved fabrication techniques.

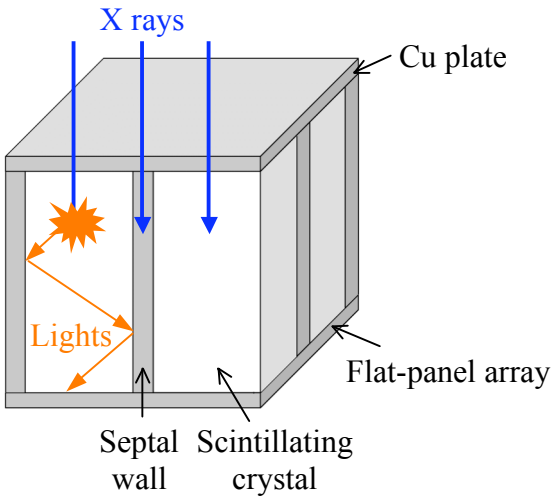

Figure 1.1. Three-dimensional schematic drawing, not to scale, of a representative portion of an EPID employing a segmented scintillator. The arrowed blue lines represent MV X rays, whereas the arrowed orange lines represent transport of optical photons in a scintillator element.

Since 2003, our group has collaborated with SGC to build segmented CsI:Tl and BGO scintillators with thicknesses up to 40 mm. Previous Monte Carlo studies based on radiation transport using the EGSnrc [81] and DOSXYZnrc [82] codes have shown that 40 mm thick segmented CsI:Tl and BGO scintillators (assuming a 0.508 mm element pitch and 0.05 mm thick polymer walls) can provide DQE_{RAD} values up to ~30 and 40 times,

respectively, higher than the DQE of conventional EPIDs.[80] In 2005, a 40 mm thick segmented CsI:Tl scintillator was built and evaluated under radiotherapy conditions. This initial engineering prototype consists of 160 × 160 elements with an element pitch of 1.016 mm, resulting in an active area of ~ 16.25 × 16.25 cm^2. The CsI:Tl crystals are separated by 0.1 mm thick polymer walls. A prototype EPID incorporating this scintillator exhibited a DQE of ~22% at zero spatial frequency. However, the MTF and DQE performance for this initial prototype was far from optimum at higher spatial frequencies due to insufficient optical isolation between scintillator elements.

D. OTHER HIGH-EFFICIENCY DETECTORS

In addition to the AMFPI-based approaches employing scintillators and photoconductors, other high-efficiency x-ray detectors were examined by other groups for MV fan-beam and cone-beam CT. For example, in a Monte Carlo study of radiation transport, Keller *et al.* examined a 1D arc detector consisting of chambers filled with high-pressure xenon gas (5 atm) located between front and back aluminum plates.[83] Using a 4 MV photon beam, this detector exhibited a QE of ~29%.

Pang et al. proposed a 2D flat detector consisting of gas cavities formed by metal substrates (along the x direction) and micro-structured metal spacer plates (along the y direction).[84] Ideally, the cavities should be focused towards the radiation source. The x-ray interaction with the metal plates (substrates and spacers) generates Compton electrons which create ions in the cavities. The ions are guided by an externally applied electric field, then collected by an underlying anisotropic conductive film, and finally read out by

a direct detection flat-panel array. Under a 6 MV beam, a QE of 60% could be achieved if tungsten were used for substrates and spacer plates. Although, in principle, this approach can lead to significant QE improvement, given the great difficulties in construction, no prototype has yet been built.

Mei et al. studied the feasibility of using thick optical fibers to detect Cerenkov radiation.[85] The proposed array of fibers, which is ~100 to 300 mm long, is focused towards the radiation source. Light generated in the fibers is collected by the underlying indirect detection flat-panel array. Although the QE can be increased up to 100% by using very long fibers, such a detector is bulky in the vicinity of a patient. Moreover, focusing the fibers towards the radiation source will be increasingly challenging for longer fibers.

V. ORGANIZATION OF DISSERTATION

With the improvement of fabrication techniques, it has become feasible to produce direct detection EPIDs employing thick HgI_2 photoconductors in the form of particle in binder (PIB). While the maximum thickness of a single layer of this photoconductor is limited to ~0.5 mm thick, much greater thicknesses can be achieved through stacking multiple PIB-HgI_2 layers. The potential portal imaging performance of such EPIDs was theoretically examined using Monte Carlo simulation of radiation transport in Chapter 2.

Although previous simulations have shown that EPIDs employing thick, segmented scintillators can provide significantly improved DQE_{RAD}, such improvement can be offset

by the optical Swank noise resulting from optical absorption and scattering. In Chapter 3, a recently implemented Monte Carlo code, MANTIS (v 2.0), which combines a radiation transport code (PENELOPE-2005) and an optical transport code (DETECT-II), was used to investigate the optical Swank factor and zero-frequency DQE as a function of various material, geometric and optical properties of the segmented scintillating detectors. The results obtained from this study provide important guidance for future scintillator development.

Encouraged by previous theoretical and empirical findings, a segmented BGO scintillator (11.3 mm thick) and three segmented CsI:Tl scintillators (11.4, 25.6 and 40.0 mm thick) were constructed. Each scintillator consists of 120 × 60 scintillator elements with an element pitch of 1.016 mm and polymer septal wall with a thickness of 0.05 mm. These scintillators, coupled to a Cyclops II array, were evaluated under radiotherapy conditions, and the results are reported in Chapter 4.

Given the impressive portal imaging performance provided by thick, segmented scintillators, it is interesting to examine their potential for MV CBCT. In Chapter 5, the EGSnrc and DOSXYZnrc codes were used to study the contrast-to-noise performance provided by hypothetical MV CBCT systems employing thick, segmented BGO and CsI:Tl scintillators. For comparison, performance was also simulated for a phosphor screen detector used in conventional EPIDs.

Note that the language and many of the figures and tables appearing in Chapters 3 to 5 have been adapted from three articles that have been published in, or submitted to the *International Journal of Medical Physics Research and Practice* by the author of this dissertation.[86-88] In addition to some revision and reorganization of these materials, further details have been added to provide the reader with a more comprehensive view of these studies. Finally, the summary and conclusions for this dissertation are presented in Chapter 6.

REFERENCES

[1] L. E. Antonuk, "Electronic portal imaging devices: a review and historical perspective of contemporary technologies and research," Physics in Medicine and Biology **47**, R31-R65 (2002).

[2] W. C. Roentgen, "On a new kind of rays," (1895).

[3] J. F. Williamson, "Brachytherapy technology and physics practice since 1950: a half-century of progress," Phys Med Biol **51**, R303-325 (2006).

[4] J. A. Purdy, "3-D radiation treatment planning: a new era," Front Radiat Ther Oncol **29**, 1-16 (1996).

[5] J. A. Purdy, "Intensity-modulated radiation therapy.," International Journal of Radiation Oncology, Biology, Physics **35**, 845-846 (1996).

[6] T. R. Mackie, J. Kapatoes, K. Ruchala, W. Lu, C. Wu, G. Olivera, L. Forrest, W. Tome, J. Welsh, R. Jeraj, P. Harari, P. Reckwerdt, B. Paliwal, M. Ritter, H. Keller, J. Fowler and M. Mehta, "Image guidance for precise conformal radiotherapy," International Journal of Radiation Oncology, Biology, Physics **56**, 89-105 (2003).

[7] M. Strandqvist and B. Rosengren, "Television-controlled pendulum therapy," Br J Radiol **31**, 513-514 (1958).

[8] J. R. Andrews, R. W. Swain and P. Rubin, "Continuous visual monitoring of 2 mev. roentgen therapy," Am J Roentgenol Radium Ther Nucl Med **79**, 74-78 (1958).

[9] N. A. Baily, R. A. Horn and T. D. Kampp, "Fluoroscopic visualization of megavoltage therapeutic x ray beams," Int J Radiat Oncol Biol Phys **6**, 935-939 (1980).

[10] P. Munro, J. A. Rawlinson and A. Fenster, "Therapy imaging: a signal-to-noise analysis of a fluoroscopic imaging system for radiotherapy localization," Med Phys **17**, 763-772 (1990).

[11] P. Munro, J. A. Rawlinson and A. Fenster, "A digital fluoroscopic imaging device for radiotherapy localization," Int J Radiat Oncol Biol Phys **18**, 641-649 (1990).

[12] H. Meertens, M. van Herk, J. Bijhold and H. Bartelink, "First clinical experience with a newly developed electronic portal imaging device," Int J Radiat Oncol Biol Phys **18**, 1173-1181 (1990).

[13] H. Meertens, M. van Herk and J. Weeda, "A liquid ionisation detector for digital radiography of therapeutic megavoltage photon beams," Phys Med Biol **30**, 313-321 (1985).

[14] M. van Herk, "Physical aspects of a liquid-filled ionization chamber with pulsed polarizing voltage," Med Phys **18**, 692-702 (1991).

[15] M. van Herk and H. Meertens, "A matrix ionisation chamber imaging device for on-line patient setup verification during radiotherapy," Radiother Oncol **11**, 369-378 (1988).

[16] L. E. Antonuk, "a-Si:H TFT-based active matrix flat-panel imagers for medical x-ray applications," in *Thin Film Transistors, Materials and Processes, Volume 1: Amorphous Silicon Thin Film Transistors*, *Vol. 1,* edited by Y. Kuo (Kluwer Academic Publishers, Boston, 2004), pp. 395-484.

[17] L. E. Antonuk, J. Boudry, C. W. Kim, M. J. Longo, E. J. Morton, J. Yorkston and R. A. Street, "Signal, noise, and readout considerations in the development of amorphous silicon photodiode arrays for radiotherapy and diagnostic x-ray imaging," Proceedings of SPIE Conference on Medical Imaging V: Image Physics **1443**, 108-119 (1991).

[18] L. E. Antonuk, C. W. Kim, J. Boudry, J. Yorkston, M. J. Longo and R. A. Street, "Development of hydrogenated amorphous silicon sensors for diagnostic x-ray imaging," IEEE Transactions on Nuclear Science **38**, 636-640 (1991).

[19] L. E. Antonuk, J. Yorkston, J. Boudry, M. J. Longo and R. A. Street, "Large area amorphous silicon photodiode arrays for radiotherapy and diagnostic imaging," Nuclear Instruments & Methods in Physics Research Section A **310**, 460-464 (1991).

[20] R. A. Street, S. Nelson, L. Antonuk and V. Perez Mendez, "Amorphous silicon sensor arrays for radiation imaging," Materials Research Society Symposium Proceedings **192**, 441-452 (1990).

[21] W. Huang, L. E. Antonuk, J. Berry, M. Maolinbay, C. Martelli, P. Mody, S. Nassif and M. Yeakey, "An asynchronous, pipelined, electronic acquisition system for active matrix flat-panel imagers (AMFPIs)," Nuclear Instruments & Methods in Physics Research Section A **431**, 273-284 (1999).

[22] I. A. Cunningham, "Applied linear-system theory," in *Handbook of medical imaging*, *Vol. 1,* edited by J. Beutel, H. L. Kundel and R. L. van Metter (SPIE, Bellingham, WA, 2000), pp. 79-160.

[23] Y. El-Mohri, K.-W. Jee, L. E. Antonuk, M. Maolinbay and Q. Zhao, "Determination of the detective quantum efficiency of a prototype, megavoltage indirect detection, active matrix flat-panel imager," Medical Physics **28**, 2538-2550 (2001).

[24] R. K. Swank, "Absorption and Noise in X-Ray Phosphors," Journal of Applied Physics **44**, 4199-4203 (1973).

[25] I. M. Blevis, D. C. Hunt and J. A. Rowlands, "X-ray imaging using amorphous selenium: determination of Swank factor by pulse height spectroscopy," Med Phys **25**, 638-641 (1998).

[26] C. Kausch, B. Schreiber, F. Kreuder, R. Schmidt and O. Dossel, "Monte Carlo simulations of the imaging performance of metal plate/phosphor screens used in radiotherapy," Medical Physics **26**, 2113-2124 (1999).

[27] D. A. Jaffray, J. J. Battista, A. Fenster and P. Munro, "Monte Carlo studies of x-ray energy absorption and quantum noise in megavoltage transmission radiography," Medical Physics **22**, 1077-1088 (1995).

[28] G. Nicolini, A. Fogliata, E. Vanetti, A. Clivio, D. Vetterli and L. Cozzi, "Testing the GlaaS algorithm for dose measurements on low- and high-energy photon beams using an amorphous silicon portal imager," Med Phys **35**, 464-472 (2008).

[29] S. M. Nijsten, W. J. van Elmpt, M. Jacobs, B. J. Mijnheer, A. L. Dekker, P. Lambin and A. W. Minken, "A global calibration model for a-Si EPIDs used for transit dosimetry," Med Phys **34**, 3872-3884 (2007).

[30] J. Chen, C. F. Chuang, O. Morin, M. Aubin and J. Pouliot, "Calibration of an amorphous-silicon flat panel portal imager for exit-beam dosimetry," Med Phys **33**, 584-594 (2006).

[31] P. Winkler, A. Hefner and D. Georg, "Dose-response characteristics of an amorphous silicon EPID," Med Phys **32**, 3095-3105 (2005).
[32] L. E. Antonuk, Y. El-Mohri, W. Huang, K.-W. Jee, J. H. Siewerdsen, M. Maolinbay, V. E. Scarpine, H. Sandler and J. Yorkston, "Initial performance evaluation of an indirect-detection, active matrix flat-panel imager (AMFPI) prototype for megavoltage imaging," International Journal of Radiation Oncology Biology Physics **42**, 437-454 (1998).
[33] P. Kupelian, T. Willoughby, A. Mahadevan, T. Djemil, G. Weinstein, S. Jani, C. Enke, T. Solberg, N. Flores, D. Liu, D. Beyer and L. Levine, "Multi-institutional clinical experience with the Calypso System in localization and continuous, real-time monitoring of the prostate gland during external radiotherapy," Int J Radiat Oncol Biol Phys **67**, 1088-1098 (2007).
[34] A. Y. Fung, K. M. Ayyangar, D. Djajaputra, R. M. Nehru and C. A. Enke, "Ultrasound-based guidance of intensity-modulated radiation therapy," Med Dosim **31**, 20-29 (2006).
[35] J. Lagendijk, B. Raaymakers, U. van der Heide, J. Overweg, K. Brown, C. Bakker, A. Raaijmakers, M. Vulpen, J. Welleweerd and I. Jürgenliemk-Schulz, "In room magnetic resonance imaging guided radiotherapy (MRIgRT)," Medical Physics **32**, 2067 (2005).
[36] S. Huh, D. Kahler, Z. Li, Z. Zhao, R. Malyapa and J. Palta, "Phantom study of evaluating the geometrical accuracy of stereotactic radiosurgery sysetm using CBCT and AlignRTTM," Medical Physics **35**, 2773 (2008).
[37] D. E. Heron, R. P. Smith and R. S. Andrade, "Advances in image-guided radiation therapy--the role of PET-CT," Med Dosim **31**, 3-11 (2006).
[38] C. M. Ma and K. Paskalev, "In-room CT techniques for image-guided radiation therapy," Med Dosim **31**, 30-39 (2006).
[39] O. Morin, A. Gillis, J. Chen, M. Aubin, M. K. Bucci, M. Roach, 3rd and J. Pouliot, "Megavoltage cone-beam CT: system description and clinical applications," Med Dosim **31**, 51-61 (2006).
[40] U. Oelfke, T. Tucking, S. Nill, A. Seeber, B. Hesse, P. Huber and C. Thilmann, "Linac-integrated kV-cone beam CT: technical features and first applications," Med Dosim **31**, 62-70 (2006).
[41] S. P. Sorensen, P. E. Chow, S. Kriminski, P. M. Medin and T. D. Solberg, "Image-guided radiotherapy using a mobile kilovoltage x-ray device," Med Dosim **31**, 40-50 (2006).
[42] M. Descovich, O. Morin, J. F. Aubry, M. Aubin, J. Chen, A. Bani-Hashemi and J. Pouliot, "Characteristics of megavoltage cone-beam digital tomosynthesis," Med Phys **35**, 1310-1316 (2008).
[43] J. Maurer, D. Godfrey, Z. Wang and F. F. Yin, "On-board four-dimensional digital tomosynthesis: first experimental results," Med Phys **35**, 3574-3583 (2008).
[44] G. Pang, A. Bani-Hashemi, P. Au, P. F. O'Brien, J. A. Rowlands, G. Morton, T. Lim, P. Cheung and A. Loblaw, "Megavoltage cone beam digital tomosynthesis (MV-CBDT) for image-guided radiotherapy: a clinical investigational system," Phys Med Biol **53**, 999-1013 (2008).

[45] C. Amies, A. Bani-Hashemi, J. C. Celi, G. Grousset, F. Ghelmansarai, D. Hristov, D. Lane, M. Mitschke, A. Singh, H. Shukla, J. Stein and M. Wofford, "A multi-platform approach to image guided radiation therapy (IGRT)," Med Dosim **31**, 12-19 (2006).

[46] W. C. Lavely, C. Scarfone, H. Cevikalp, R. Li, D. W. Byrne, A. J. Cmelak, B. Dawant, R. R. Price, D. E. Hallahan and J. M. Fitzpatrick, "Phantom validation of coregistration of PET and CT for image-guided radiotherapy," Med Phys **31**, 1083-1092 (2004).

[47] D. A. Jaffray and J. H. Siewerdsen, "Cone-beam computed tomography with a flat-panel imager: Initial performance characterization," Medical Physics **27**, 1311-1323 (2000).

[48] D. A. Jaffray, J. H. Siewerdsen, J. W. Wong and A. A. Martinez, "Flat-panel cone-beam computed tomography for image-guided radiation therapy," International Journal of Radiation Oncology*Biology*Physics **53**, 1337-1349 (2002).

[49] J. H. Siewerdsen and D. A. Jaffray, "Cone-beam computed tomography with a flat-panel imager: Magnitude and effects of x-ray scatter," Medical Physics **28**, 220-231 (2001).

[50] Y. Cho, D. J. Moseley, J. H. Siewerdsen and D. A. Jaffray, "Accurate technique for complete geometric calibration of cone-beam computed tomography systems," Med Phys **32**, 968-983 (2005).

[51] J. Pouliot, A. Bani-Hashemi, J. Chen, M. Svatos, F. Ghelmansarai, M. Mitschke, M. Aubin, P. Xia, O. Morin, K. Bucci, M. Roach, 3rd, P. Hernandez, Z. Zheng, D. Hristov and L. Verhey, "Low-dose megavoltage cone-beam CT for radiation therapy," International Journal of Radiation Oncology, Biology, Physics **61**, 552-560 (2005).

[52] F. F. Yin, H. Guan and W. Lu, "A technique for on-board CT reconstruction using both kilovoltage and megavoltage beam projections for 3D treatment verification," Medical Physics **32**, 2819-2826 (2005).

[53] K. M. Langen, S. L. Meeks, D. O. Poole, T. H. Wagner, T. R. Willoughby, P. A. Kupelian, K. J. Ruchala, J. Haimerl and G. H. Olivera, "The use of megavoltage CT (MVCT) images for dose recomputations," Physics in Medicine & Biology **50**, 4259-4276 (2005).

[54] O. Morin, A. Gillis, M. Descovich, J. Chen, M. Aubin, J. Aubry, H. Chen, A. Gottschalk, P. Xia and J. Pouliot, "Patient dose considerations for routine megavoltage cone-beam CT imaging," Medical Physics **34**, 1819-1827 (2007).

[55] O. Morin, J. Chen, M. Aubin, S. Bose, A. Gillis, M. Bucci and J. Pouliot, "Dose Calculation Using Megavoltage Cone Beam CT Imaging," International Journal of Radiation Oncology Biology Physics **63**, S62-S63 (2005).

[56] H. Guan, F. F. Yin and J. H. Kim, "Accuracy of inhomogeneity correction in photon radiotherapy from CT scans with different settings," Physics in Medicine and Biology **47**, N223-N231 (2002).

[57] B. A. Groh, J. H. Siewerdsen, D. G. Drake, J. W. Wong and D. A. Jaffray, "A performance comparison of flat-panel imager-based MV and kV cone-beam CT," Medical Physics **29**, 967-975 (2002).

[58] A. Sawant, L. E. Antonuk, Y. El-Mohri, Y. Li, Z. Su, Y. Wang, J. Yamamoto, Q. Zhao, H. Du, J. Daniel and R. A. Street, "Segmented phosphors – MEMS-based high quantum efficiency detectors for megavoltage x-ray imaging," Medical Physics **32**, 553-565 (2005).
[59] T. Falco, H. Wang and B. G. Fallone, "Preliminary study of a metal/a-Se-based portal detector," Med Phys **25**, 814-823 (1998).
[60] M. Lachaine and B. G. Fallone, "Monte Carlo detective quantum efficiency and scatter studies of a metal/a-Se portal detector," Med Phys **25**, 1186-1194 (1998).
[61] M. Lachaine, E. Fourkal and B. G. Fallone, "Detective quantum efficiency of a direct-detection active matrix flat panel imager at megavoltage energies," Med Phys **28**, 1364-1372 (2001).
[62] G. Pang, D. L. Lee and J. A. Rowlands, "Investigation of a direct conversion flat panel imager for portal imaging," Med Phys **28**, 2121-2128 (2001).
[63] H. Du, L. E. Antonuk, Y. El-Mohri, Q. Zhao, Z. Su, J. Yamamoto and Y. Wang, "Investigation of the signal behavior at diagnostic energies of prototype, direct detection, active matrix, flat-panel imagers incorporating polycrystalline HgI2," Physics in Medicine and Biology **53**, 1325-1351 (2008).
[64] H. Kraus, V. B. Mikhailik, Y. Ramachers, D. Day, K. B. Hutton and J. Telfer, "Feasibility study of a ZnWO4 scintillator for exploiting materials signature in cryogenic WIMP dark matter searches," Physics Letters B **610**, 37-44 (2005).
[65] D. J. Krus, W. P. Novak and L. Perna, presented at the Hard X-Ray, Gamma-Ray, and Neutron Detector Physics, Denver, CO, USA, 1999 (unpublished).
[66] C. W. van Eijk, "Inorganic scintillators in medical imaging," Phys Med Biol **47**, R85-106 (2002).
[67] C. W. E. v. Eijk, "Inorganic scintillators in medical imaging," Physics in Medicine and Biology **47**, R85-R106 (2002).
[68] Product data sheet for Cesium Iodide scintillation material, Saint-Gobain Crystals, OH, U.S.
[69] Product data sheet for Bismuth Germanate scintillation material, Saint-Gobain Crystals, OH, U.S.
[70] Product data sheet for Prelude 420 scintillation material, Saint-Gobain Crystals, OH, U.S.
[71] Product data sheet for Cadmium Tungstate scintillation material, Saint-Gobain Crystals, OH, U.S.
[72] D. G. Lewis, W. Swindell, E. J. Morton, P. M. Evans and Z. R. Xiao, "A megavoltage CT scanner for radiotherapy verification," Physics in Medicine & Biology **37**, 1985-1999 (1992).
[73] E. J. Morton, W. Swindell, D. G. Lewis and P. M. Evans, "A linear array, scintillation crystal-photodiode detector for megavoltage imaging," Medical Physics **18**, 681-691 (1991).
[74] T. T. Monajemi, B. G. Fallone and S. Rathee, "Thick, segmented CdWO4-photodiode detector for cone beam megavoltage CT: a Monte Carlo study of system design parameters," Medical Physics **33**, 4567-4577 (2006).
[75] T. T. Monajemi, D. Tu, B. G. Fallone and S. Rathee, "A bench-top megavoltage fan-beam CT using CdWO4-photodiode detectors. II. Image performance evaluation," Medical Physics **33**, 1090-1100 (2006).

[76] S. Rathee, D. Tu, T. T. Monajemi, D. W. Rickey and B. G. Fallone, "A bench-top megavoltage fan-beam CT using CdWO4-photodiode detectors. I. System description and detector characterization," Medical Physics **33**, 1078-1089 (2006).

[77] M. A. Mosleh-Shirazi, P. M. Evans, W. Swindell, J. R. Symonds-Tayler, S. Webb and M. Partridge, "Rapid Portal Imaging with a High-Efficiency, Large Field-of-View Detector," Medical Physics **25**, 2333-2346 (1998).

[78] M. A. Mosleh-Shirazi, P. M. Evans, W. Swindell, S. Webb and M. Partridge, "A cone-beam megavoltage CT scanner for treatment verification in conformal radiotherapy," Radiotherapy & Oncology **48**, 319-328 (1998).

[79] M. A. Mosleh-Shirazi, W. Swindell and P. M. Evans, "Optimization of the Scintillation Detector in a Combined 3D Megavoltage CT Scanner and Portal Imager," Medical Physics **25**, 1880-1890 (1998).

[80] A. Sawant, L. E. Antonuk, Y. El-Mohri, Q. Zhao, Y. Li, Z. Su, Y. Wang, J. Yamamoto, H. Du, I. Cunningham, M. Klugerman and K. Shah, "Segmented crystalline scintillators: an initial investigation of high quantum efficiency detectors for megavoltage x-ray imaging," Medical Physics **32**, 3067-3083 (2005).

[81] I. Kawrakow and D. W. O. Rogers, "The EGSnrc Code System: Monte Carlo Simulation of Electron and Photon Transport," Ottawa, Canada (2000).

[82] J. A. Treurniet, B. R. B. Walters and D. W. O. Rogers, "BEAMnrc, DOSXYZnrc and BEAMDP GUI User's Manual," Ottawa, Canada (2001).

[83] H. Keller, M. Glass, R. Hinderer, K. Ruchala, R. Jeraj, G. Olivera and T. R. Mackie, "Monte Carlo study of a highly efficient gas ionization detector for megavoltage imaging and image-guided radiotherapy," Medical Physics **29**, 165-175 (2002).

[84] G. Pang and J. A. Rowlands, "Development of high quantum efficiency, flat panel, thick detectors for megavoltage x-ray imaging: a novel direct-conversion design and its feasibility," Medical Physics **31**, 3004-3016 (2004).

[85] X. Mei, J. A. Rowlands and G. Pang, "Electronic portal imaging based on Cerenkov radiation: A new approach and its feasibility," Medical Physics **33**, 4258-4270 (2006).

[86] Y. Wang, L. E. Antonuk, Y. El-Mohri and Q. Zhao, "A Monte Carlo investigation of Swank noise for thick, segmented, crystalline scintillators for radiotherapy imaging," Medical Physics, accepted for publication (2009).

[87] Y. Wang, Q. Zhao, L. E. Antonuk, Y. El-Mohri and L. Perna, "High-DQE EPIDs based on thick, segmented BGO and CsI:Tl scintillators: Performance evaluation at extremely low dose," Medical Physics, under review (2009).

[88] Y. Wang, L. E. Antonuk, Y. El-Mohri, Q. Zhao, A. Sawant and H. Du, "Monte Carlo investigations of megavoltage cone-beam CT using thick, segmented scintillating detectors for soft tissue visualization," Medical Physics **35**, 145-158 (2008).

CHAPTER 2

MERCURIC IODIDE PHOTOCONDUCTORS: A MONTE CARLO INVESTIGATION OF PORTAL IMAGING PERFORMANCE

I. INTRODUCTION

As explained in the previous chapter, direct detection EPIDs hold distinct advantages for radiotherapy imaging. Given that the transfer of the electrical charge in the photoconductor is regulated by an externally applied electric field, the photoconductor can be made relatively thick to improve QE, without significant degradation in MTF and Swank factor. These favorable properties make it possible for the direct detection EPIDs based on thick photoconductors to provide much higher DQE than conventional EPIDs.

A highly promising photoconductor material, mercuric iodide (HgI_2), has been investigated by our group for diagnostic and radiotherapy imaging.[1-3] Thus far, a large number of AMFPI arrays have been coated with HgI_2 and evaluated. HgI_2 deposition was previously provided by Real-Time Radiography, Ltd. (RTR, Israel). The evaluation results for some of those arrays under diagnostic and radiotherapy conditions can be found in previous publications.[2, 3] More recent arrays have been coated with HgI_2 provided by Radiation Monitoring Devices, Inc. (RMD, Boston).

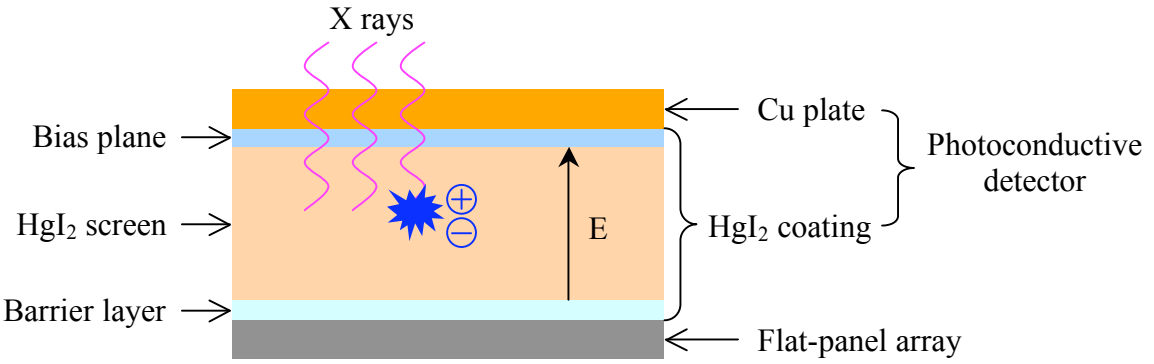

Figure 2.1. Schematic side view of a direct detection EPID employing a HgI_2 photoconductive detector. The drawing is not to scale.

Figure 2.1 shows a schematic view of an EPID based on a HgI_2 photoconductive detector deposited on a direct detection flat-panel array. The detector consists of a HgI_2 coating with an overlying 1 mm thick Cu plate (used to absorb low-energy scattered radiation and to enhance QE). The HgI_2 coating consists of three layers – a polymer barrier layer, a bias plane and a HgI_2 screen sandwiched in between. The barrier layer (~1.5 to 3 μm thick) is deposited on the array prior to the deposition of the screen to protect the exposed metals (e.g., Al) of the array from the highly reactive HgI_2. This layer facilitates vertical charge transfer and inhibits lateral charge conduction. The HgI_2 screen can be either deposited through physical vapor deposition (PVD) or using a screen-printing technique with the material in the form of particle in binder (PIB).[2] PVD is performed in a vacuum reactor in which HgI_2 is deposited over the barrier-layer-coated array. With this type of deposition, the packing density of the PVD screens, defined as the mass density of the HgI_2 material in the screen relative to the density of the single crystal form of HgI_2, is ~90%. For the PIB screens, HgI_2 grains and the polymer binder material (having a density of ~1.05 g/cm^3) are blended in a 9:1 weight ratio in a solvent to form a mixture. A layer of the mixture is screen-printed on the barrier-layer-coated array.

Using a low-temperature sintering process, the solvent is evaporated from the mixture, forming a PIB-HgI_2 screen with a packing density of ~50%. After screen deposition, an ~0.1 μm thick layer of palladium is coated on the screen, serving as a top electrode.

In a previous study, prototype EPIDs coated with a PVD-HgI_2 screen (~0.3 mm thick) and a PIB-HgI_2 screen (~0.46 mm thick) were evaluated using a 6 MV photon beam.[3] Compared to a conventional, indirect detection EPID, these prototypes exhibit higher MTF and similar DQE. Moreover, both prototypes show input-quantum-limited performance at extremely low dose (i.e., 0.008 cGy).[3] Encouraged by the results from these early prototypes, it would be interesting to next examine HgI_2 screens with larger thicknesses. This can be achieved by stacking multiple layers of PIB-HgI_2 material, given that it is very difficult to deposit a single layer of PVD or PIB screen thicker than ~0.5 mm with good properties over a large area. Presently, prototype arrays employing multi-layer PIB-HgI_2 screens are being investigated in collaboration with RMD. In this chapter, the potential performance of such screens is examined using a Monte Carlo method.

II. SIMULATION METHODS

Monte Carlo simulations of radiation transport were performed to examine QE, MTF_{RAD}, normalized NPS_{RAD} ($NNPS_{RAD}$) and DQE_{RAD} for photoconductive detectors employing a 1 mm thick copper plate and a PIB-HgI_2 screen at different thicknesses. The imaging signal corresponds to the radiation energy deposited in the screen layer. The simulated PIB-HgI_2 material had a mass density of 3.18 g/cm^3, which corresponds to 50%

of that of the single crystalline HgI_2 density. Polymer binders were not included in the simulations. The radiation source was simulated as a 6 MV photon beam, the spectrum for which is shown in Fig. 2.2. This spectrum was used for all simulational work presented in this dissertation.

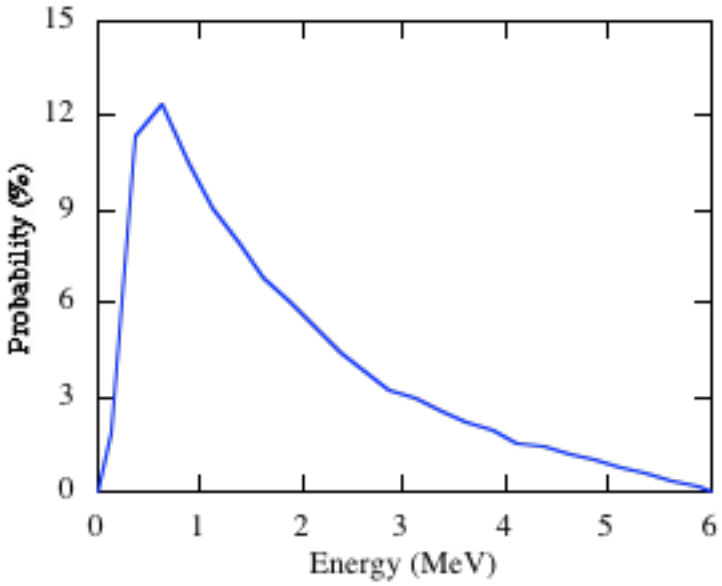

Figure 2.2. 6 MV photon beam spectrum used in the simulations, representing the spectral output of a Varian LINAC used in radiotherapy.[4] The size of each energy bin is 0.25 MeV. The data points correspond to the center of the energy bins.

A. QE

The QE of the photoconductive detectors was examined as a function of PIB-HgI_2 screen thickness. The radiation source was simulated as a pencil beam incident on the center of the detector. These simulations were conducted using the EGS4 code,[5] with a total of one million x-ray histories for each screen thickness.

B. MTF_{RAD}

MTF_{RAD} and $NNPS_{RAD}$ were simulated for various screen thicknesses, using the EGSnrc [6] and DOSXYZnrc [7] codes. Fig. 2.3 shows a top view of the detector geometry

used in the simulations to determine the MTF of the photoconductive detector (MTF_{DET}). The detector, which consists of a 1 mm thick copper plate overlying a screen layer of PIB-HgI_2, has an area of 40 × 40 mm^2, with a 1 mm wide strip running along the center. The strip was divided into 8000 cells, each having an area of 0.005 × 1 mm^2. In the simulations, a parallel radiation beam with 100 million x-ray histories and dimensions of 0.004 × 40 mm^2 was generated incident on the center of the detector along the direction perpendicular to the strip. The energy deposited in the cells in the screen layer along the strip was used to determine the detector LSF (LSF_{DET}), whose Fourier transform yielded MTF_{DET}. The MTF_{RAD} of the hypothetical EPIDs was determined from the product of MTF_{DET} and the sinc function corresponding to a pixel pitch values of 0.508 mm (which is equal to the pixel pitch of an indirect detection flat-panel array used for our radiotherapy research).[8-11]

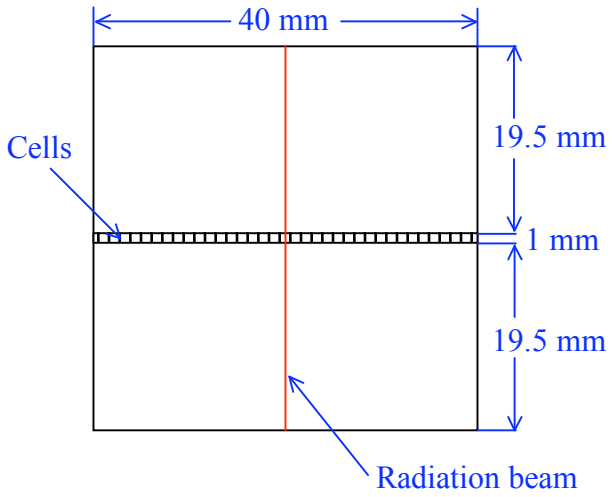

Figure 2.3. Top view of the detector geometry for the MTF_{DET} simulations. The detector has an area of 40 × 40 cm^2 and consists of a strip of cells from which radiation signal deposition is extracted. The red line superimposed on the detector represents the radiation beam falling perpendicular to the detector plane and to the direction of the strip of cells. Note that the illustration is not to scale.

C. $NNPS_{RAD}$ and DQE_{RAD}

For the $NNPS_{RAD}$ simulations, the detector was divided into 600 × 600 voxels with a voxel pitch of 0.508 mm (resulting in an area of 30.48 × 30.48 cm^2). The radiation source was a 30 × 30 cm^2 parallel beam. For each screen thickness, 50 such simulations were conducted, with 900 million histories carried out for each set. From each simulation, ten blocks, each consisting of 250 × 100 voxels, were obtained from the central 500 × 500 voxels – avoiding the edges of the detector. In this way, the 50 simulations yielded 500 independent slits. Each slit was averaged along the shorter dimension to form a 250-point realization. A 1D Fourier transform was applied to each of the 500 realizations. The resulting 500 power spectra were appropriately normalized and averaged to yielded NPS_{RAD}.[12] The normalized NPS_{RAD}, $NNPS_{RAD}$, is expressed as:

$$NNPS_{RAD}(f) = \frac{\bar{q}_0 \times NPS_{RAD}(f)}{S_{RAD}^2}, \tag{2.1}$$

where S_{RAD} is the amount of radiation energy deposited in each screen voxel and $\bar{q}_0$ is the incident x-ray fluence which is equal to 10,000 X rays/mm^2.

DQE_{RAD} is calculated using MTF_{RAD} and $NNPS_{RAD}$:

$$DQE_{RAD}(f) = \frac{MTF_{RAD}^2(f)}{NNPS_{RAD}(f)}. \tag{2.2}$$

The MTF_{RAD} and DQE_{RAD} results correspond to theoretical upper limits for the EPIDs employing the corresponding PIB-HgI_2 screens, and thus do not include effects of secondary quanta in the photoconductor. However, in actual PIB-HgI_2 screens, the presence of the externally applied electric field across the photoconductor restricts the lateral spreading of secondary quanta, as well as ensures efficient charge collection.

Therefore, the overall MTF and DQE for the corresponding direct detection EPIDs are not expected to be significantly lower than these theoretical expectations.

III. RESULTS

In this section, the simulated MTF_{RAD} and DQE_{RAD} results for hypothetical EPIDs employing PIB-HgI_2 screens are compared to measured results from a conventional EPID (with a pixel pitch of 0.508 mm) obtained from Ref. 9.

A. QE

Figure 2.4 shows QE as a function of PIB-HgI_2 screen thickness. QE is seen to increase approximately linearly with increasing screen thickness in this range. An EPID employing a 6 mm thick PIB-HgI_2 screen offers a QE of ~14%, which is approximately seven times higher than that provided by conventional EPIDs.

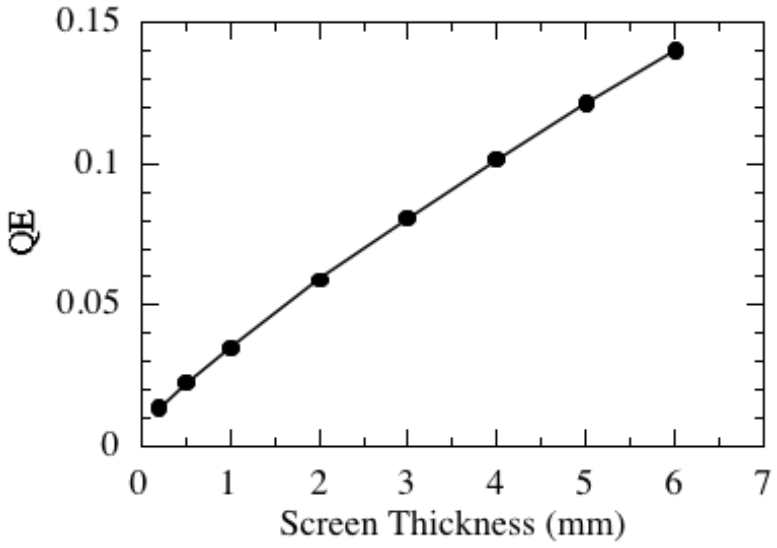

Figure 2.4. QE plotted as a function of thickness of the PIB-HgI_2 screen.

B. MTF_{RAD}

Figure 2.5 shows the MTF_{RAD} for EPIDs employing PIB-HgI_2 screens of various thicknesses, along with the measured MTF from a conventional EPID (which includes the spreading of secondary optical quanta). The results indicate that all simulated direct detection EPIDs (employing PIB-HgI_2 screens up to 6 mm thick) can provide higher MTF than the conventional EPID at all spatial frequencies. However, as screen thickness increases, MTF_{RAD} degrades due to increased lateral spreading of secondary radiation (i.e., electrons and X rays) in the screen. It is also interesting to note that the decrease in MTF_{RAD} becomes gradually less significant as screen thickness increases, possibly the result of the limited range for the scattered radiation in the PIB-HgI_2 screen.

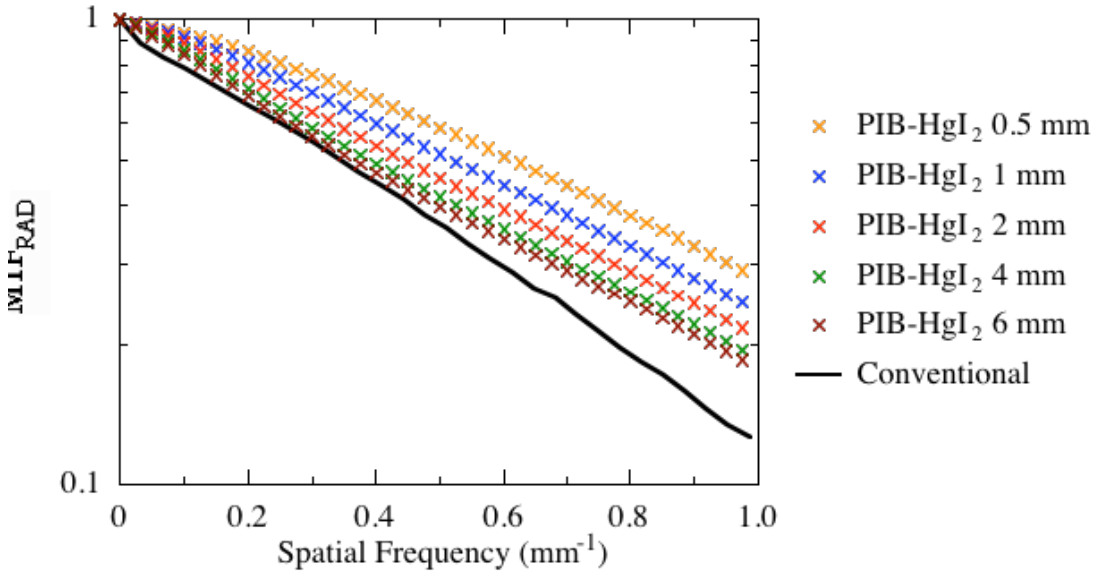

Figure 2.5. Simulated MTF_{RAD} for EPIDs employing PIB-HgI_2 screens of various thicknesses, compared to the measured MTF for a conventional EPID.

C. $NNPS_{RAD}$

Figure 2.6 shows simulated $NNPS_{RAD}$ for EPIDs employing PIB-HgI_2 screens of different thicknesses. The magnitude of $NNPS_{RAD}$ is found to decrease with increasing

screen thickness due to the increased number of X rays sampled (i.e., higher QE) and more complete absorption of radiation energy (i.e., lower radiation Swank noise). In addition, all $NNPS_{RAD}$ results are seen to drop with increasing spatial frequency, due to the presence of noise correlation induced by lateral radiation spreading. Such a drop is observed to be more significant for thicker screens due to stronger noise correlation.

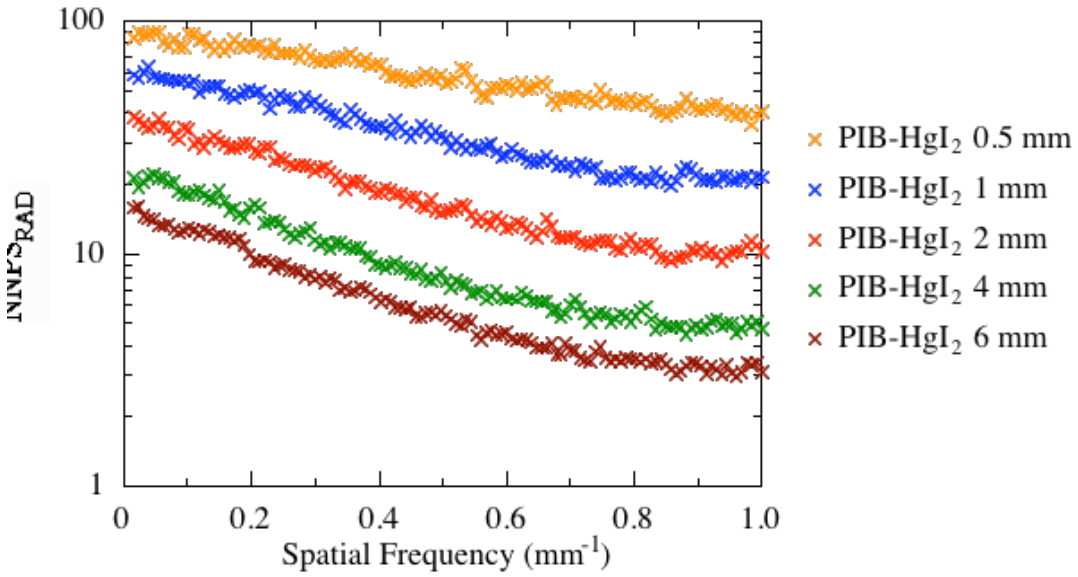

Figure 2.6. Simulated $NNPS_{RAD}$ for EPIDs employing PIB-HgI_2 screens of different thicknesses.

D. DQE_{RAD}

Figure 2.7 shows simulated DQE_{RAD} for EPIDs incorporating PIB-HgI_2 screens of different thicknesses, along with the measured DQE for the conventional EPID. The EPID employing a 0.5 mm thick PIB-HgI_2 screen exhibits a DQE_{RAD} comparable to that of conventional EPIDs. Moreover, thicker screens result in higher DQE_{RAD} at all spatial frequencies. The direct detection EPIDs employing a 6 mm thick PIB-HgI_2 screen offers

a DQE_{RAD} value of ~6% at zero spatial frequency – a value ~ 5 times higher than that measured from the conventional EPID.

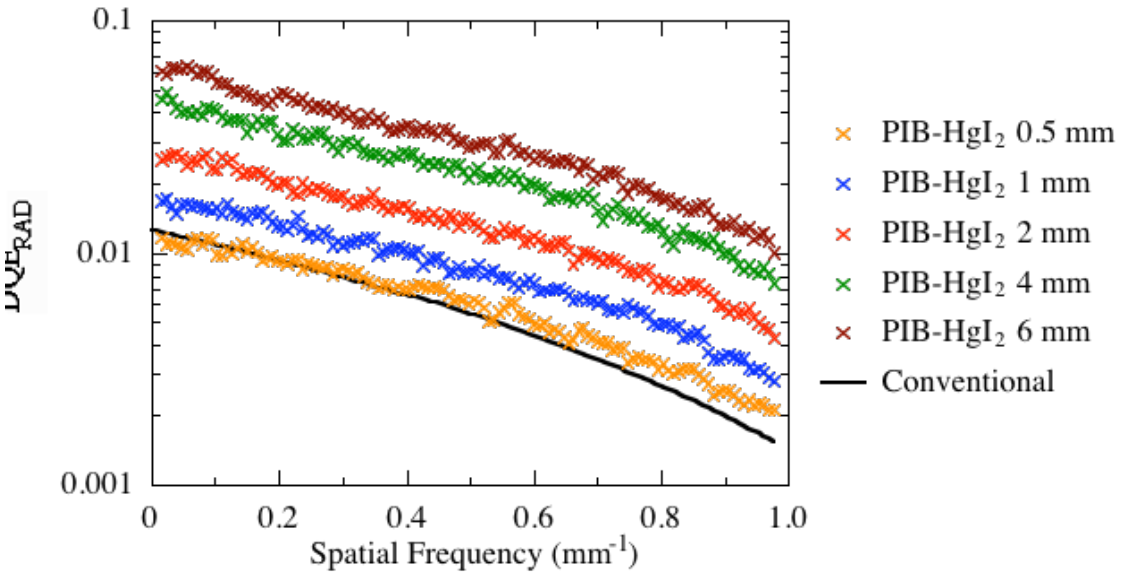

Figure 2.7. Simulated DQE_{RAD} for EPIDs employing PIB-HgI_2 screens of different thicknesses, compared to the measured DQE from the conventional EPID.

IV. SUMMARY

The simulation results reported in this chapter indicate that direct detection EPIDs employing PIB-HgI_2 screens up to 6 mm thick have the potential to provide up to a factor of ~5 improvement in DQE compared to conventional EPIDs, while providing similar MTF. Although such potential improvements are modest compared to those for indirect detection EPIDs based on thick, segmented scintillators (as shown in Chapters 3 and 4), the cost for coating PIB-HgI_2 screens would possibly be lower than for fabricating segmented scintillators.

REFERENCES

[1] Z. Su, L. E. Antonuk, Y. El-Mohri, L. Hu, H. Du, A. Sawant, Y. Li, Y. Wang, J. Yamamoto and Q. Zhao, "Systematic investigation of the signal properties of polycrystalline HgI2 detectors under mammographic, radiographic, fluroroscopic and radiotherapy irradiation conditions," Physics in Medicine and Biology **50**, 2907-2928 (2005).

[2] H. Du, L. E. Antonuk, Y. El-Mohri, Q. Zhao, Z. Su, J. Yamamoto and Y. Wang, "Investigation of the signal behavior at diagnostic energies of prototype, direct detection, active matrix, flat-panel imagers incorporating polycrystalline HgI2," Physics in Medicine and Biology **53**, 1325-1351 (2008).

[3] Q. Zhao, L. E. Antonuk, Y. El-Mohri, Y. Wang, H. Du, A. Sawant, Z. Su and J. Yamamoto, "Performance evaluation of polycrystalline HgI2 photoconductors for radiotherapy imaging," to be submitted for peer-review.

[4] D. Sheikh-Bagheri, Ph.D. Thesis, Carleton University, 1999.

[5] D. A. Jaffray, J. J. Battista, A. Fenster and P. Munro, "Monte Carlo studies of x-ray energy absorption and quantum noise in megavoltage transmission radiography," Med Phys **22**, 1077-1088 (1995).

[6] I. Kawrakow and D. W. O. Rogers, "The EGSnrc Code System: Monte Carlo Simulation of Electron and Photon Transport," Ottawa, Canada (2000).

[7] J. A. Treurniet, B. R. B. Walters and D. W. O. Rogers, "BEAMnrc, DOSXYZnrc and BEAMDP GUI User's Manual," Ottawa, Canada (2001).

[8] L. E. Antonuk, Y. El-Mohri, W. Huang, K.-W. Jee, J. H. Siewerdsen, M. Maolinbay, V. E. Scarpine, H. Sandler and J. Yorkston, "Initial performance evaluation of an indirect-detection, active matrix flat-panel imager (AMFPI) prototype for megavoltage imaging," International Journal of Radiation Oncology Biology Physics **42**, 437-454 (1998).

[9] Y. El-Mohri, K.-W. Jee, L. E. Antonuk, M. Maolinbay and Q. Zhao, "Determination of the detective quantum efficiency of a prototype, megavoltage indirect detection, active matrix flat-panel imager," Medical Physics **28**, 2538-2550 (2001).

[10] A. Sawant, L. E. Antonuk, Y. El-Mohri, Y. Li, Z. Su, Y. Wang, J. Yamamoto, Q. Zhao, H. Du, J. Daniel and R. A. Street, "Segmented phosphors – MEMS-based high quantum efficiency detectors for megavoltage x-ray imaging," Medical Physics **32**, 553-565 (2005).

[11] A. Sawant, L. E. Antonuk, Y. El-Mohri, Q. Zhao, Y. Wang, Y. Li, H. Du and L. Perna, "Segmented crystalline scintillators: empirical and theoretical investigation of a high quantum efficiency EPID based on an initial engineering prototype CsI(Tl) detector," Medical Physics **33**, 1053-1066 (2006).

[12] A. Sawant, L. E. Antonuk, Y. El-Mohri, Q. Zhao, Y. Li, Z. Su, Y. Wang, J. Yamamoto, H. Du, I. Cunningham, M. Klugerman and K. Shah, "Segmented crystalline scintillators: an initial investigation of high quantum efficiency detectors for megavoltage x-ray imaging," Medical Physics **32**, 3067-3083 (2005).

CHAPTER 3

SEGMENTED SCINTILLATORS: A MONTE CARLO INVESTIGATION OF SWANK NOISE

I. INTRODUCTION

Monte Carlo simulation has proven to be a very useful tool to predict the performance of AMFPI-based EPIDs employing thick, segmented scintillators.[1] Simulation results provide valuable guidance for optimization of imaging performance. For example, previous Monte Carlo simulations of radiation transport have predicted that EPIDs employing 10 to 40 mm thick, segmented CsI:Tl and BGO scintillators could offer zero-frequency DQE_{RAD} values of ~10% to ~50%, corresponding to values ~10 to 50 times higher than the DQE measured from conventional EPIDs.[1] Given these encouraging early theoretical findings, it is interesting to next investigate how the generation and transport of secondary optical photons affect the DQE performance of such EPIDs. In particular, one optical effect that degrades DQE is the optical component of Swank noise.

The Swank noise for indirect detection EPIDs consists of two main components: radiation and optical Swank noise. The total Swank noise and its two components can be quantified by Swank factors (I, I_{RAD} and I_{OPT}), with a smaller value indicating a higher Swank noise. Descriptions of Swank noise and definition of Swank factors are detailed in Sec. III.D.2 of Chapter 1. Given that the performance of AMFPI-based EPIDs is

generally not limited by noise power aliasing or electronic noise, zero-frequency DQE and zero-frequency DQE_{RAD} can be determined using the formulas shown in Eqs. (1.5) and (1.6), respectively. Note that all DQE and DQE_{RAD} results reported in this chapter correspond to their values at zero frequency.

In principle, increasing scintillator thickness will lead to higher QE (due to greater radiation attenuation) and larger I_{RAD} (due to more complete absorption of the x-ray energy), resulting in higher DQE_{RAD}. However, when scintillator thickness increases, optical photons have to traverse longer paths, on average, to reach the underlying flat-panel array, leading to more light loss and thus a smaller I_{OPT} that results in a smaller I. Such decreases in I_{OPT} will, at least partially, offset the potential gains in DQE_{RAD} obtained through increasing scintillator thickness.[2]

In this chapter, Monte Carlo simulations of radiation and optical transport were performed to investigate Swank noise and DQE for hypothetical EPIDs employing thick, segmented scintillators. This study was conducted as part of a research program to support the development of high-efficiency x-ray detectors for radiotherapy imaging. Note that most of the figures shown in this chapter were obtained from a manuscript that the author of this dissertation submitted to the *International Journal of Medical Physics Research and Practice*,[3] with the exception of Figs. 3.5(a), 3.5(b) and 3.6(b).

II. TECHNICAL BACKGROUND: MANTIS

A. OVERVIEW

The simulations presented in this chapter were performed using a recently implemented Monte Carlo package, MANTIS (v2.0),[4] which is a combination of a radiation transport code (PENELOPE-2005)[5] and an optical transport code (DETECT-II).[6] The MANTIS code was developed by Dr. Badano at the U.S. Food and Drug Administration (FDA), and was initially used to simulate the light transport in needle-like CsI:Tl screens for diagnostic imaging.[7, 8] The input and output files used in MANTIS are briefly summarized in APPENDIX A, whereas the method for parallel processing (developed by the author) is described in APPENDIX B. In addition, a glossary of symbols and functions specifically used in this chapter appears in Table 3.1.

Table 3.1. Glossary of the symbols and functions used in this chapter.

Detector optical properties			
μ_A	Material absorption coefficient	θ_{MAX}	Surface Roughness
μ_{A-SCI}	Absorption coefficient: scintillator	$\theta_{MAX-0.9}$	Roughness resistance
μ_S	Material scattering coefficient	G	Scintillator conversion gain
μ_{S-SCI}	Scattering coefficient: scintillator	$G_{CsI:Tl}$	Conversion gain of CsI:Tl
α	Surface absorptivity	E	Energy deposited in scintillator
α_{TOP}	Absorptivity: top reflector	N	# of photons generated per E
α_{WALL}	Absorptivity: septal walls	E_A	Absorbed energy per X ray
β	User-selected scalar for roughness	N_G	# of generated photons per X ray
$\vec{n}_0$	Normal to a surface	N_D	# of detected photons per X ray
$\vec{n}_R$	Normal to a local micro-facet	N_E	# of detected photons per MeV
$\vec{v}$	Unit vector with random direction	η	Optical detection efficiency
θ	Angular tilt of $\vec{n}_R$ from $\vec{n}_0$	γ	Critical angle
Detector geometric properties		**Functions**	
T_{SCI}	Scintillator thickness	*Round*	Rounding to nearest integers
W_{SCI}	Width of scintillating crystals	*Poisson*	Generating Poisson integers
ϕ_{SCI}	Scintillating crystal aspect ratio	*Norm*	Normalizing vectors
P_E	Element-to-element pitch		
W_{WALL}	Width of septal walls		

B. SIMULATION OF RADIATION AND OPTICAL TRANSPORT

PENELOPE simulates the energy deposition for each incident X ray. Once x-ray energy is deposited in the scintillator, DETECT-II is triggered to isotropically generate optical photons at the point of energy deposition. For the amount of energy E deposited in the scintillating crystal, N optical photons are generated using the following expression:

$$N = Poisson\left[Round[E \times G]\right], \tag{3.1}$$

where $Poisson$ is a function to generate integers with a Poisson distribution, $Round$ is a rounding function and G is the average optical conversion gain of the scintillator material (i.e., 54,000 and 8,500 photons/MeV for CsI:Tl and BGO, respectively).[9, 10] DETECT-II simulates the transport of each of the N photons. The optical simulation of a photon is terminated once the optical photon is absorbed in the detector or detected by the underlying photodiode array.

C. OPTICAL SURFACE MODELS

In MANTIS, optical surfaces can be defined as partially or totally absorptive, with a user-defined surface absorptivity, α, ranging from 0 to 1. Optical photons that are not absorbed at the surface will either be reflected back to the original medium, or transmitted into the next medium (i.e., refraction). For surfaces allowing light transmission, the code determines if a light photon is reflected or refracted using Fresnel's law. For surfaces not allowing light transmission (referred to as "reflectors"), all photons that are not absorbed will be reflected back toward the original medium.

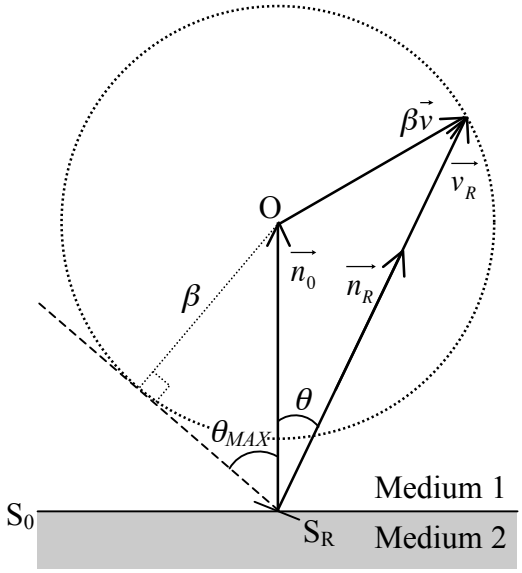

Figure 3.1. Illustration of the surface roughness model used by DETECT-II. S_0 is an interface plane adjoining media 1 and 2, and S_R is a local micro-facet that is tilted at an angle θ with respect to S_0. The definitions of $\vec{n_0}$, β, $\vec{v}$ and θ_{MAX} are given in the main text. Note that $\vec{v_R}$ is equal to the vector sum of $\vec{n_0}$ and $\beta\vec{v}$. Since $\vec{v}$ is a unit vector with random direction, the possible end points of $\vec{v_R}$ are located at points along a dotted circle of radius β, centered at point O. The dashed line, originating from the point of optical interaction, is tangent to the circle. Note that this model can generate non-physical solutions for which the vector representing the reflected or refracted photon points towards the wrong medium. In such cases, the code will abandon the solution and repeat the calculation by generating a new $\vec{v}$ until a physical solution is obtained.

In addition, optical surfaces can be defined as smooth or rough. For a smooth surface, the direction of reflected photons is determined using the normal to the surface, $\vec{n_0}$, and the rule for specular reflection. The direction of refracted photons is calculated using $\vec{n_0}$ and Snell's law. As illustrated in Fig. 3.1, for each optical reflection or refraction occurring at a rough surface S_0, the code calculates a normal, $\vec{n_R}$, to a local micro-facet, S_R, having an angle θ with respect to $\vec{n_0}$. The distribution of θ is determined by a user-selected scalar, β, which can range from 0 to 1. For each optical

interaction, the code generates a unit vector with random direction, $\vec{v}$, and calculates $\overrightarrow{n_R}$ as follows:

$$\overrightarrow{n_R} = Norm[\overrightarrow{n_0} + \beta\vec{v}], \tag{3.2}$$

where $Norm$ is the normalization function for vectors. In this chapter, surface roughness is expressed in terms of the maximum value of θ, θ_{MAX}. The correspondence between the selected value of β and θ_{MAX} is given by:

$$\theta_{MAX} = \arcsin(\beta). \tag{3.3}$$

III. SIMULATION METHODS

A. SIMULATED EPIDS EMPLOYING SEGMENTED SCINTILLATORS

Figure 3.2 shows a schematic view of a portion of the general structure of the simulated EPIDs, each of which consists of a segmented scintillating detector coupled to a photodiode array (represented in the simulation by a layer of 0.001 mm thick a:Si-H). The detector also includes a 1 mm thick copper plate (serving as both radiation build-up layer and optical top reflector) coupled to the incident x-ray side of the scintillator.

The scintillator consists of 81 × 81 scintillating crystals separated by polystyrene septal walls. The width of the septal walls, W_{WALL}, is 0.05 mm throughout this study. Monte Carlo simulations were performed for a variety of segmented BGO and CsI:Tl detector designs with scintillator thicknesses, T_{SCI}, of 10 to 40 mm, and element-to-element pitches, P_E (the distance between the centers of two adjacent crystals), of 0.508 to 1.016 mm. The pitch values of 0.508 and 1.016 mm correspond to the multiple of the

pixel pitch (0.508 mm) for the Cyclops II array presently used for evaluation of prototype scintillators.[11] The aspect ratio of the scintillating crystals, ϕ_{SCI}, is defined as:

$$\phi_{SCI} = \frac{T_{SCI}}{W_{SCI}} \tag{3.4}$$

$$= \frac{T_{SCI}}{P_E - W_{WALL}},$$

where W_{SCI} is the width of the scintillating crystal.

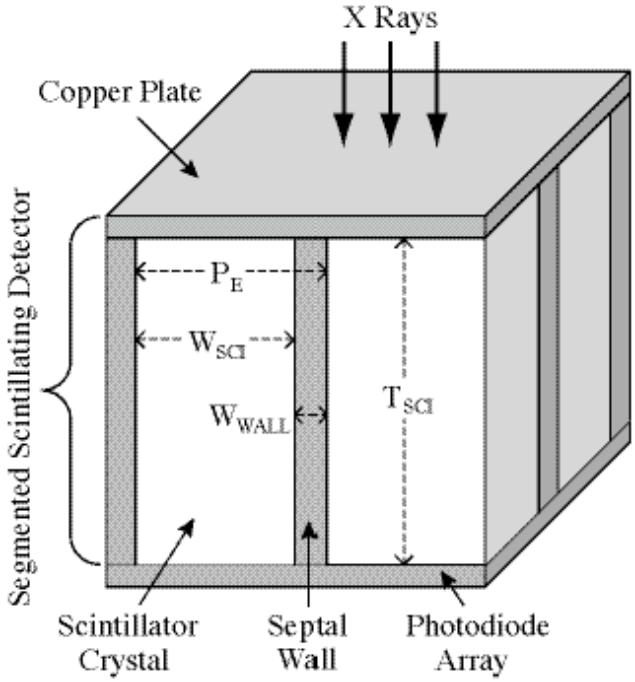

Figure 3.2. Three-dimensional schematic drawing, not to scale, of a representative portion of the megavoltage active matrix, flat-panel imagers (AMFPIs) simulated in this study. Each simulated detector consists of a 2D matrix of scintillating crystals, separated by septal walls, with an overlying top copper plate. The detector is coupled to a photodiode array, which is represented in the simulation by a thin layer of silicon. See main text for further details.

B. MONTE CARLO SIMULATIONS

In this chapter, the phrase "scintillator design" will refer to a collection of segmented scintillator configurations for a specific combination of scintillator material (i.e., BGO or CsI:Tl) and geometries (i.e., T_{SCI}, P_E and W_{WALL}). All scintillator configurations (having different optical properties) corresponding to the same design have the same radiation transport properties, and thus the same QE, I_{RAD} and DQE_{RAD}. These metrics were obtained for each design from simulations using a customized version of MANTIS in which optical transport is disabled. For radiation simulations, the kinetic cut-off energies for electrons, X rays and positrons (the minimum energy below which tracking of a quantum is terminated) were set to a common value of 0.01 MeV. The simulations employed a 6 MV parallel photon beam [12] with an area of 10×10 mm^2. The beam area is large enough to accurately simulate the effects occurring at the septal walls and small enough compared to detector area to ensure containment of lateral secondary radiation. QE was determined from the fraction of the incident X rays that deposit energy in the scintillating crystals and I_{RAD} was determined from the absorbed energy distribution. DQE_{RAD} was calculated as the product of QE and I_{RAD}. For a given detector design, 10^6 x-ray histories were used in the determination of QE and I_{RAD} whereas, for a given detector configuration, 10^5 histories were used in the determination of I_{OPT} (note that optical simulations were more computationally intensive and thus necessitated fewer histories). The simulations reported in this article were performed using a 64-bit Linux cluster with up to two hundred 1.8 GHz AMD Opteron processors and consumed a total of ~350,000 CPU hours.

For selected designs, I_{OPT} was studied as a function of the various detector optical properties, which include absorption and scattering in the scintillating crystals, absorption at the top reflector and at the septal walls, as well as scattering at the side surfaces of the crystals. The refractive indices of BGO, CsI:Tl and photodiode were assumed to be 2.15, 1.79 and 1.70, respectively.[9, 10] The absorption and scattering coefficients for both scintillators (μ_{A-SCI} and μ_{S-SCI}) were assumed to be 0.02 and 0 cm^{-1}, respectively,[13] unless otherwise stated. All surfaces were assumed to be smooth, unless otherwise stated. The top reflector and septal walls were simulated as reflectors (prohibiting optical transmission) with absorption characterized by absorptivity of α_{TOP} and α_{WALL}, respectively. The bottom surface of the scintillating crystals was assumed to allow light transmission with no absorption. In the simulations, no optical coupling medium (e.g., glue) is used between the crystals and the photodiode. Although such a medium is necessary for crystalline scintillators for nuclear medicine (e.g., PET) to preserve signal, it is not needed for portal imaging due to the very large light output from scintillators under radiotherapy conditions. All light photons entering the photodiode layer are counted as detected signal.

IV. RESULTS

A. QE, I_{RAD} AND DQE_{RAD}

Figure 3.3 shows results for QE, I_{RAD} and DQE_{RAD} as a function of scintillator thickness (T_{SCI}) for segmented BGO and CsI:Tl scintillators with element pitches (P_E) of 1.016 and 0.508 mm. As observed, scintillator designs with greater T_{SCI} and higher scintillator density (i.e., BGO) exhibit higher QE, due to increased x-ray attenuation, and

larger I_{RAD}, due to more efficient absorption of x-ray energy. Moreover, designs with larger P_E show slightly higher QE and I_{RAD}, by virtue of their larger scintillator fill factor (90% at 1.016 mm versus 81% at 0.508 mm). Note that a large component of Swank

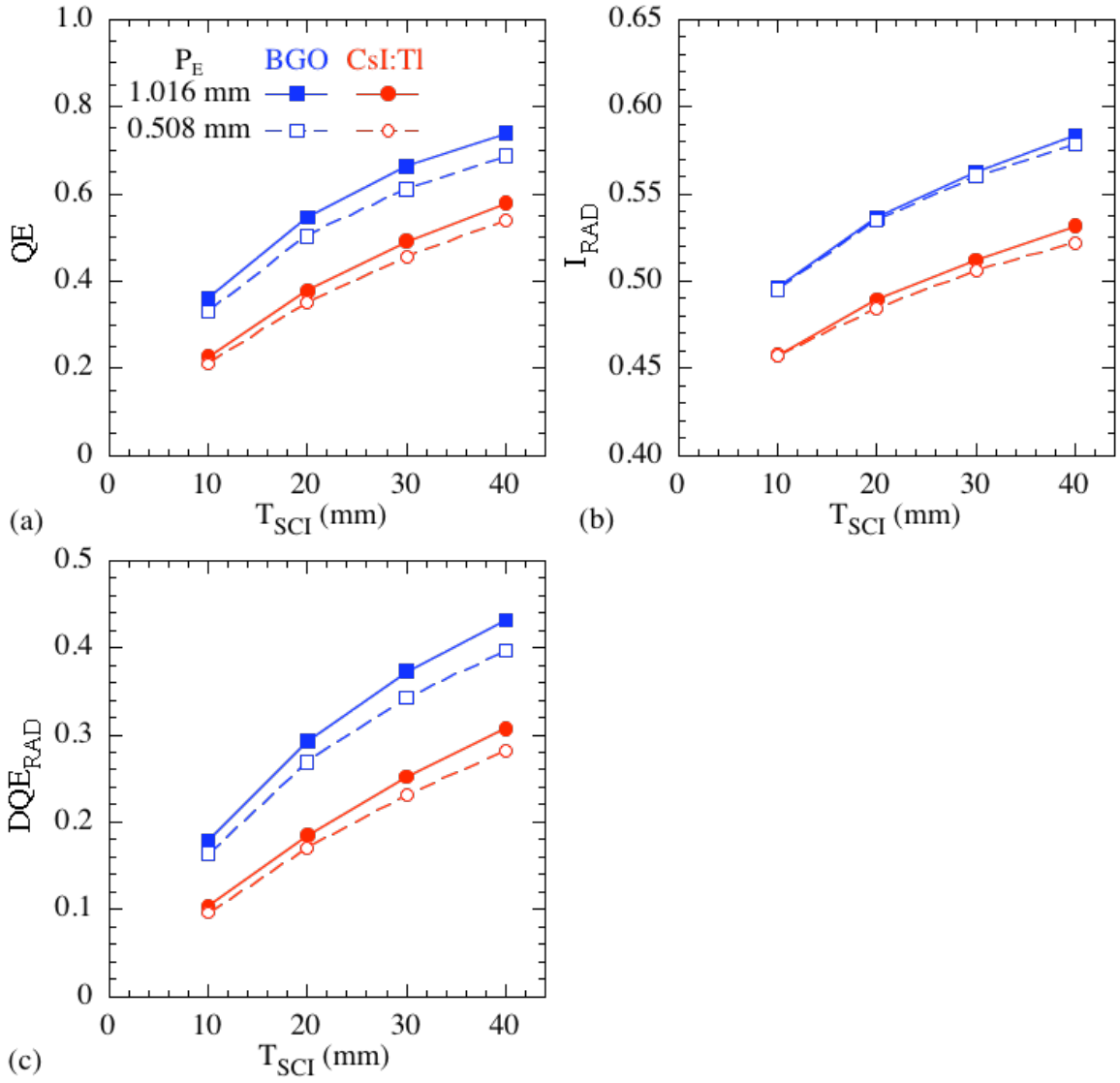

Figure 3.3. Simulation results for (a) quantum efficiency, QE, (b) radiation Swank factor, I_{RAD}, and (c) radiation DQE, DQE_{RAD}. The results are plotted as a function of scintillator thickness, T_{SCI}, for segmented BGO and CsI:Tl detectors at pitches of 1.016 and 0.508 mm. In this and the remaining figures, lines are drawn between the points to guide the eye, unless otherwise indicated.

noise that is included in the determination of I_{RAD} is due to the significant spread of the 6 MV poly-energetic spectrum. Estimate of the Swank factor for this component alone is ~0.66. Finally, the trends for DQE_{RAD} are similar to those for QE and I_{RAD}.

B. VALIDATION OF THE USE OF REDUCED GAIN FOR CsI:Tl

The amount of computational time required for the intended systematic examination of I_{OPT} for the various CsI:Tl scintillator configurations would exceed that available for this study if the nominal conversion gain for that material, $G_{CsI:Tl}$ (54,000 photons/MeV), were used. In order to overcome this limitation, a reduced value for conversion gain, $0.1 \times G_{CsI:Tl}$, was used. The conditions under which such a reduction will still lead to a correct determination of I_{OPT} are described in APPENDIX C.

In order to validate the use of this reduction, a comparison of I_{OPT} values determined through simulations of 10 to 40 mm thick CsI:Tl scintillators at pitches of 1.016 and 0.508 mm was performed using $G_{CsI:Tl}$ and $0.1 \times G_{CsI:Tl}$. In these simulations, α_{TOP}, α_{WALL} and θ_{MAX} were assumed to be 100%, 4% and 0°, respectively. The results of the simulations, shown in Fig. 3.4, demonstrate that the use of reduced gain results in negligible underestimation of I_{OPT} for the examined scintillator designs. Moreover, given these results, it is reasonable to expect that the use of reduced gain should also be valid for CsI:Tl scintillators at pitches between 0.508 and 1.016 mm. Therefore, reduced gain was used for all remaining simulations involving CsI:Tl scintillators. In the case of the BGO simulations, a reduction in conversion gain is not required due to the more modest magnitude of that parameter (i.e., 8,500 photons/MeV).

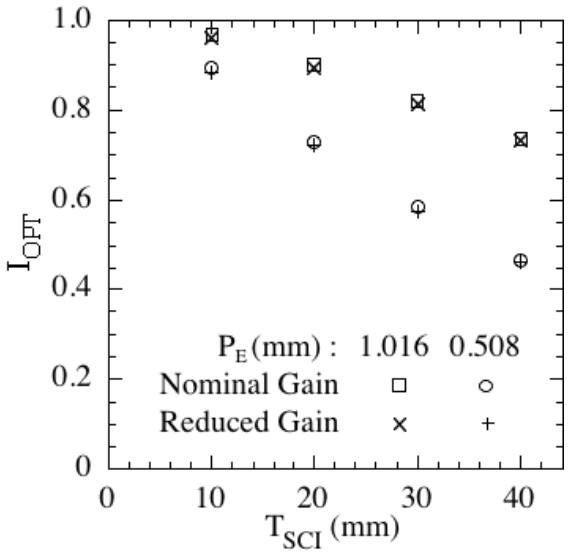

Figure 3.4. Simulation results for optical Swank factor, I_{OPT}, plotted as a function of T_{SCI}. The results were obtained using the nominal and a reduced conversion gain, $G_{CsI:Tl}$ and $0.1 \times G_{CsI:Tl}$, respectively. Results are shown for 10 to 40 mm thick segmented CsI:Tl detectors at pitches of 1.016 and 0.508 mm.

C. I_{OPT} AND DQE

In this section, simulation results for I_{OPT} and DQE are reported as a function of various optical properties for selected scintillator designs. A summary of the comparative behaviors of I_{OPT} for the EPIDs employing BGO and CsI:Tl scintillators appears in Sec. IV.C.5.

1. Absorption and scattering in scintillating crystals

In Figs. 3.5(a) and 3.5(c), I_{OPT} results are plotted as a function of μ_{A-SCI} (assuming μ_{S-SCI} is 0 cm^{-1}) and μ_{S-SCI} (assuming μ_{A-SCI} is 0 cm^{-1}), respectively, for segmented CsI:Tl scintillators at different values of T_{SCI} and P_E. In these simulations, α_{TOP}, α_{WALL} and θ_{MAX} were assumed to be 100%, 2% and 0°, respectively. The results indicate that I_{OPT} decreases with increasing μ_{A-SCI} and μ_{S-SCI}. Moreover, the rate of decrease is

steeper for scintillators with greater thickness, but not obviously different for the two pitches. Furthermore, the drop of I_{OPT} with increasing μ_{A-SCI} is found to be approximately linear. As shown in Fig. 3.5(b) and 3.5(d), the effects of μ_{A-SCI} and μ_{S-SCI} on DQE are minimal for detectors thinner than 20 mm (where the drop is less than 0.008) and are modest for detectors between 20 and 40 mm thick (where the decrease is less than 0.03).

In the simulations reported in the remainder of this chapter, for both BGO and CsI:Tl scintillators, μ_{A-SCI} and μ_{S-SCI} are assumed to be fixed at 0.02 and 0 cm^{-1}, respectively, unless otherwise stated. For our previous [14] and current prototype scintillators (which are reported in Chapter 4), the extinction (absorption plus scattering) length for CsI:Tl and BGO is at least 50 and 700 cm (corresponding to coefficients of 0.02 and 0.0014 cm^{-1}), respectively, according to measurements conducted by SGC. For simplicity, all interactions in the scintillating crystals are considered absorptive in the reminder of this study. In addition, although BGO is a less absorptive material than CsI:Tl, the use of the same μ_{A-SCI} and μ_{S-SCI} values for both scintillators allows direct comparison of the behavior of the corresponding I_{OPT} as a function of other optical properties (e.g., α_{WALL}). Slightly overestimating the value of μ_{A-SCI} for BGO results in a small underestimate of I_{OPT} and DQE.

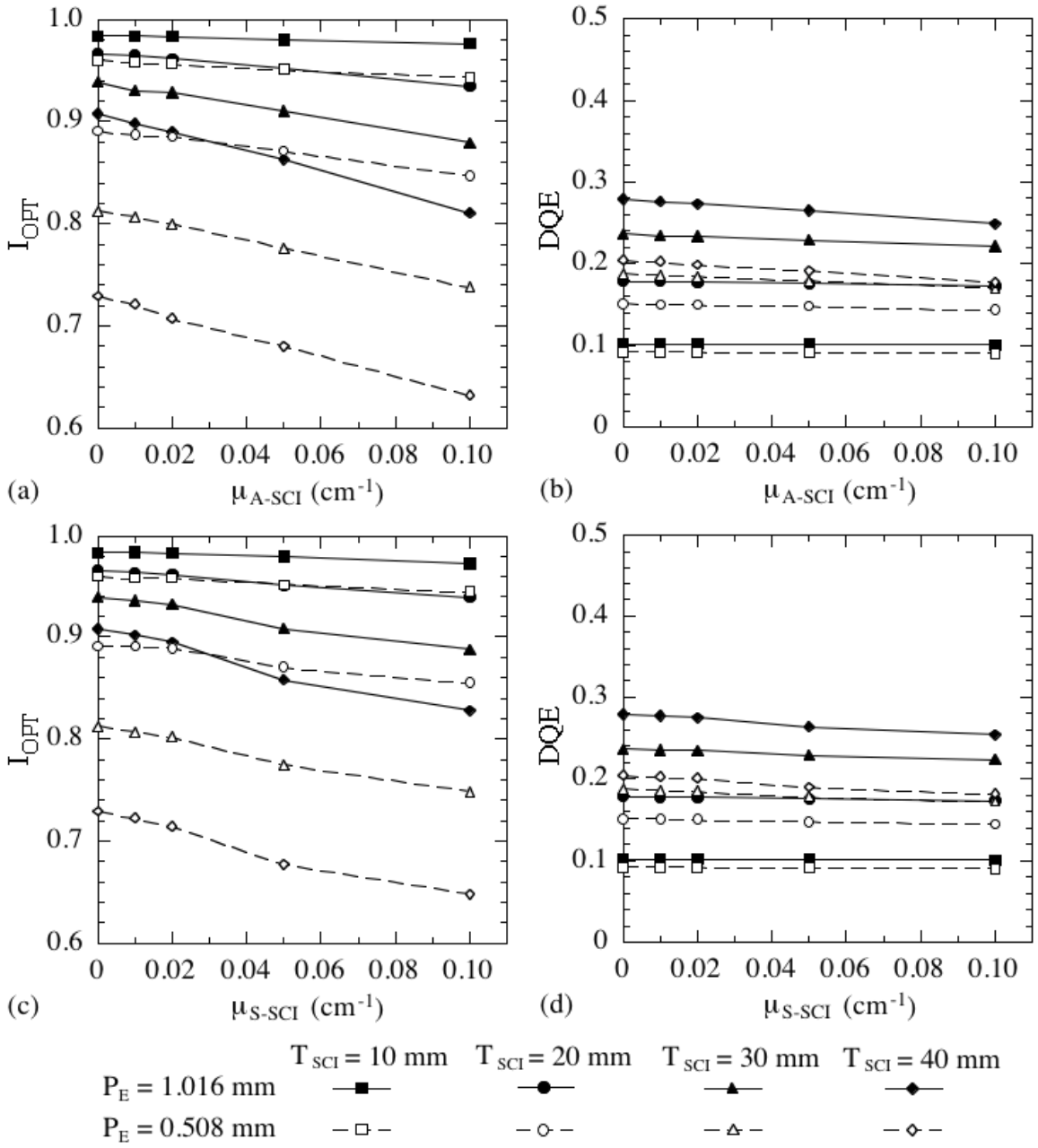

Figure 3.5. Simulation results for I_{OPT} and DQE plotted as a function of scintillator absorption coefficient (μ_{A-SCI}) in (a) and (b), and as a function of scintillator scattering coefficient (μ_{S-SCI}) in (c) and (d), respectively. Results are shown for 10 to 40 mm thick segmented CsI:Tl scintillators at pitches of 1.016 and 0.508 mm.

2. Absorption at top reflector

Figure 3.6(a) shows simulation results for I_{OPT} as a function of α_{TOP} for 20 and 40 mm thick segmented BGO and CsI:Tl scintillators at pitches of 1.016 and 0.508 mm. In these simulations, α_{WALL} and θ_{MAX} were assumed to be 2% and 0°, respectively. For all examined scintillator designs, I_{OPT} decreases approximately linearly with increasing α_{TOP}. This decline is explained in the discussion of the results for Fig. 3.8 in Sec. IV.C.3. Moreover, I_{OPT} for each BGO configuration is higher than that for its CsI:Tl counterpart. The same trends were also found for the 10 and 30 mm thick detectors, the results for which are not shown. In addition, as shown in Fig. 3.6(b), the reduction of DQE caused by increasing α_{TOP} is less than ~0.017 for the examined scintillator configurations.

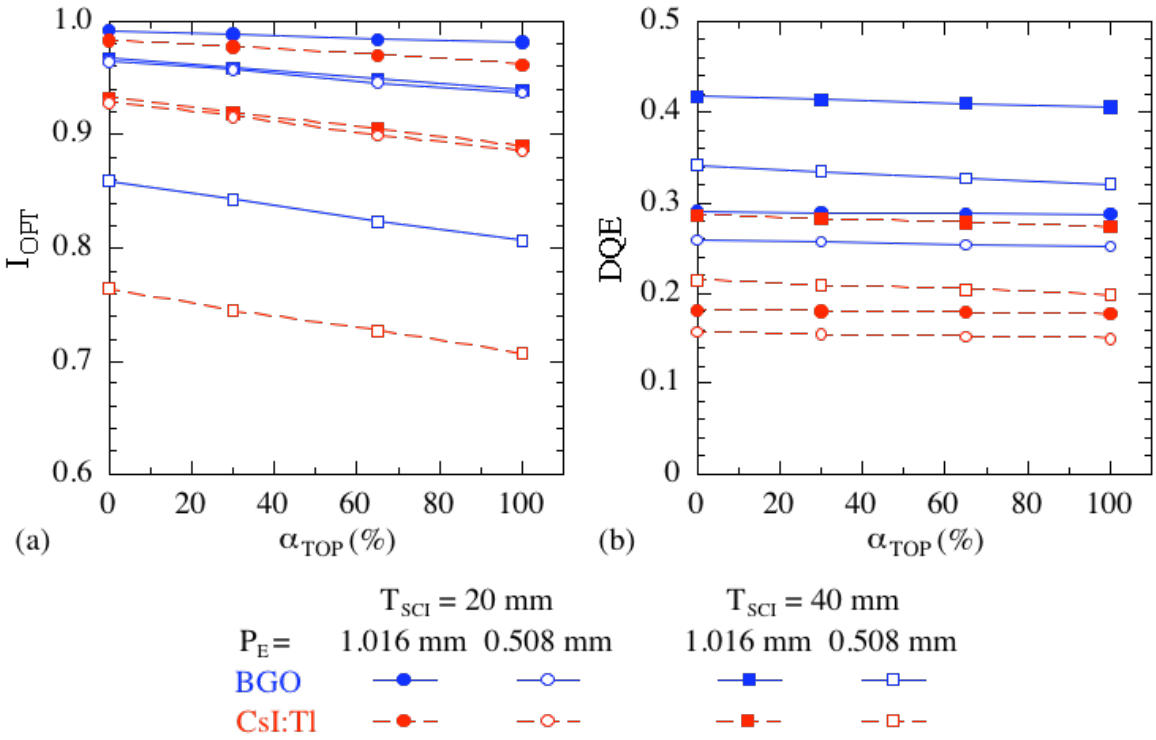

Figure. 3.6. Simulation results for (a) I_{OPT} and (b) DQE plotted as a function of top reflector absorptivity, α_{TOP}. Results are shown for 20 and 40 mm thick segmented BGO and CsI:Tl detectors at pitches of 1.016 and 0.508 mm.

3. Absorption at septal walls

Figure 3.7 shows simulation results for I_{OPT} and DQE as a function of α_{WALL} for 10 to 40 mm thick segmented BGO and CsI:Tl scintillators at pitches of 1.016 and 0.508 mm. In these simulations, α_{TOP} and θ_{MAX} were set to be 100% and 0°, respectively. As seen in Figs. 3.7(a) and 3.7(c), I_{OPT} decreases with increasing α_{WALL} for all examined scintillator designs. Moreover, this decline is more pronounced for scintillators with greater thickness and smaller pitch, the reason for which is explained in the discussion of the Fig. 3.8 results below. In addition, I_{OPT} for each BGO configuration is higher than that for its CsI:Tl counterpart. The results shown in Figs. 3.7(b) and 3.7(d) indicate that DQE generally decreases with increasing α_{WALL}. Moreover, this decrease is more significant for scintillators with greater thickness and smaller pitch, diminishing the advantage of increasing scintillator thickness. In addition, at pitch values of 1.016 and 0.508 mm, the DQE is not strongly affected by increasing α_{WALL} for detectors thinner than ~20 mm and ~10 mm, respectively (at least up to an α_{WALL} value of 6%). Finally, at both pitches and at a given value of α_{WALL}, the 20 mm thick BGO scintillator generally offers higher DQE than CsI:Tl detectors up to 40 mm thick.

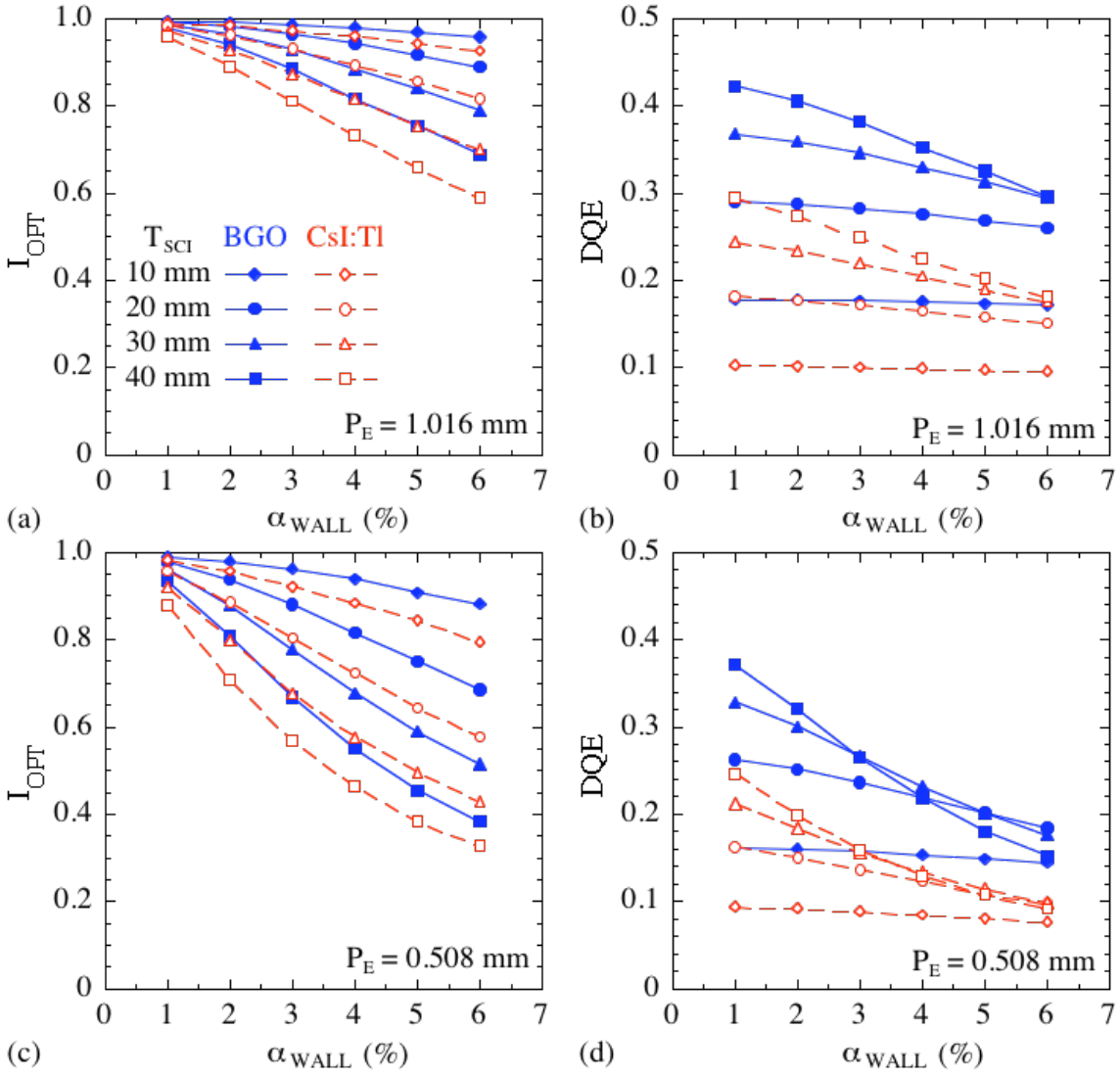

Figure 3.7. Simulation results for I_{OPT} and DQE plotted as a function of septal wall absorptivity, α_{WALL}, for 10 to 40 mm thick segmented BGO and CsI:Tl detectors. Results for I_{OPT} and DQE for detectors with 1.016 mm pitch are shown in (a) and (b), while results for detectors with 0.508 mm pitch are shown in (c) and (d), respectively.

The results shown in Figs. 3.7(a) and 3.7(c) demonstrate that I_{OPT} decreases with increasing α_{WALL} and T_{SCI}, as well as decreasing P_E. As indicated by Eq. (3.5), greater T_{SCI} and smaller P_E both result in greater ϕ_{SCI}. In order to examine the combined influence of ϕ_{SCI} and α_{WALL} on I_{OPT}, results for segmented BGO and CsI:Tl scintillators configured with an absorptive and a reflective top reflector are plotted as a function of

$\phi_{SCI} \times \alpha_{WALL}$ in Fig. 3.8. The four sets of simulation results include some of the results illustrated in Figs. 3.6 and 3.7. In addition, the two sets of results for the reflective top reflector (α_{TOP} equal to 0%) also include results obtained from simulations performed at a value of α_{WALL} equal to 4%. In all simulations, θ_{MAX} was assumed to be 0°. For a given set of results, the small difference in I_{OPT} observed for simulations corresponding to the same value of $\phi_{SCI} \times \alpha_{WALL}$ (but different ϕ_{SCI} and α_{WALL} values) is a consequence of the competing, non-linear effects of ϕ_{SCI} and α_{WALL} on I_{OPT} when there is optical absorption in the scintillating crystals (i.e., when μ_{A-SCI} is greater than 0 cm^{-1}). For example, at a $\phi_{SCI} \times \alpha_{WALL}$ value of 1.75, the configuration with a greater ϕ_{SCI} but a smaller α_{WALL}, shows slightly lower I_{OPT}.

In order to quantify the trends of the results illustrated in Fig. 3.8, a fourth-order polynomial function of the form:

$$f(x) = C_0 + C_1 \cdot x + C_2 \cdot x^2 + C_3 \cdot x^3 + C_4 \cdot x^4 \tag{3.5}$$

was used to fit each set of results. The resulting values of the coefficients, C_0, C_1, C_2, C_3 and C_4, are listed in Table 3.2. For the smallest examined value of $\phi_{SCI} \times \alpha_{WALL}$ (i.e., ~0.1), I_{OPT} is greater than 0.99 for all four sets of simulations. As $\phi_{SCI} \times \alpha_{WALL}$ increases, I_{OPT} declines in all cases mainly due to increased light loss at septal walls. Specifically, greater ϕ_{SCI} increases the number of optical interactions occurring at the walls, whereas higher α_{WALL} increases the probability of optical absorption for each interaction. Additionally, for a given type of top reflector, BGO offers higher I_{OPT} compared to CsI:Tl at the same value of $\phi_{SCI} \times \alpha_{WALL}$. This difference initially increases as $\phi_{SCI} \times \alpha_{WALL}$ increases, but remains approximately constant beyond a $\phi_{SCI} \times \alpha_{WALL}$ value of ~1.9. Also,

it is found that the use of a reflective top reflector, compared to an absorptive top reflector, results in higher I_{OPT} for all examined configurations. This difference initially increases with increasing $\phi_{SCI} \times \alpha_{WALL}$, but does not further increase beyond $\phi_{SCI} \times \alpha_{WALL}$ values of ~1.9 and 1.1 for BGO and CsI:Tl, respectively. For both scintillators, this difference remains less than ~0.06 for $\phi_{SCI} \times \alpha_{WALL}$ values up to ~3.5.

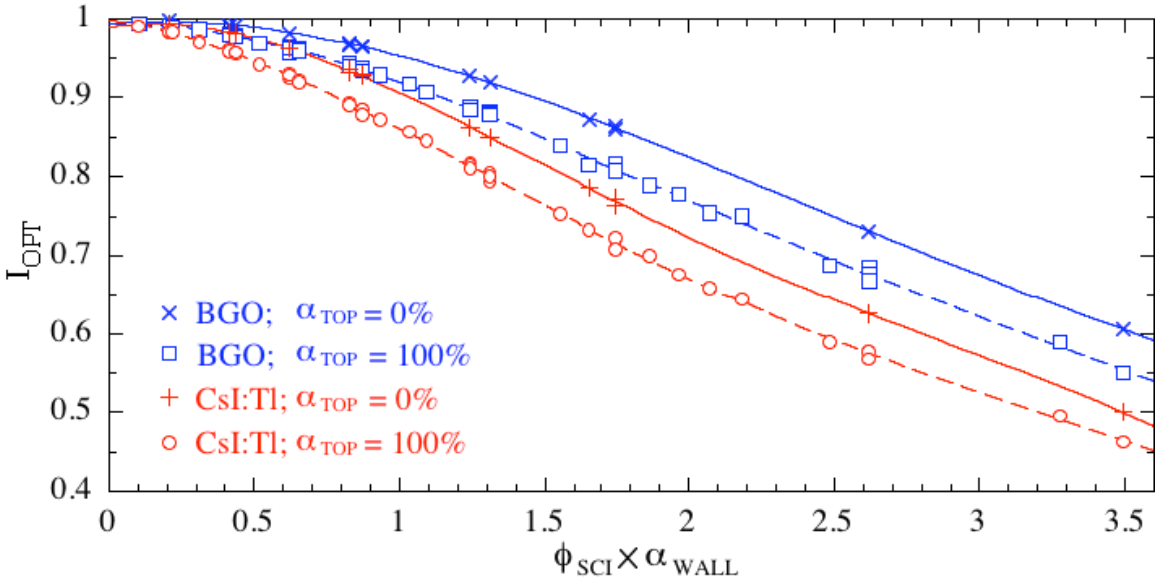

Figure 3.8. Simulation results for I_{OPT} plotted as a function of the product of the aspect ratio of the scintillating crystals, ϕ_{SCI}, and α_{WALL}. Results are shown for AMFPIs employing segmented BGO or CsI:Tl detectors configured with a reflective (α_{TOP} equal to 0%) or an absorptive (α_{TOP} equal to 100%) top reflector. The solid and dashed lines correspond to fits to the simulation results using fourth order polynomial functions.

Table 3.2. List of coefficients determined from fits to the simulation results appearing in Fig. 3.8. The fits were based on the fourth order polynomial function shown in Eq. (3.5).

	C_0	C_1	C_2	C_3	C_4
BGO; $\alpha_{TOP} = 0\%$	9.93×10^{-1}	3.04×10^{-2}	-8.61×10^{-2}	1.63×10^{-2}	-9.27×10^{-4}
BGO; $\alpha_{TOP} = 100\%$	9.92×10^{-1}	9.98×10^{-3}	-1.11×10^{-1}	3.10×10^{-2}	-2.98×10^{-3}
CsI:Tl; $\alpha_{TOP} = 0\%$	9.89×10^{-1}	5.73×10^{-2}	-2.01×10^{-1}	6.82×10^{-2}	-7.72×10^{-3}
CsI:Tl; $\alpha_{TOP} = 100\%$	9.98×10^{-1}	-4.97×10^{-2}	-1.30×10^{-1}	4.68×10^{-2}	-5.16×10^{-3}

4. Scattering at the side surfaces of the scintillating crystals

Figure 3.9 shows simulation results for I_{OPT} and DQE as a function of θ_{MAX} for 10 to 40 mm thick segmented BGO and CsI:Tl scintillators at pitches of 1.016 and 0.508 mm. In these simulations, α_{TOP} and α_{WALL} were assumed to be 100% and 2%, respectively. As shown in Figs. 3.9(a) and 3.9(c), I_{OPT} decreases with increasing θ_{MAX}, except between 0° and 5°, where a slight increase is seen for some of the 10 and 20 mm thick scintillators. Moreover, the scintillators with greater thickness and smaller pitch are more affected by increasing θ_{MAX}. In addition, although each BGO configuration offers higher I_{OPT} than its CsI:Tl counterpart at θ_{MAX} equal to 0°, this difference is reduced and, for thicker scintillators, reversed as θ_{MAX} increases. Moreover, the reversal of this difference occurs at progressively smaller θ_{MAX} values for scintillators with greater thickness and smaller pitch. As observed in Figs. 3.9(b) and 3.9(d), DQE generally decreases with increasing θ_{MAX}. This decrease is more significant for scintillators with greater thickness and smaller pitch, diminishing the DQE advantage of increasing scintillator thickness. In addition, at pitches of 1.016 and 0.508 mm, the DQE is not significantly affected by increasing θ_{MAX} (at least up to θ_{MAX} values of 20°) for scintillators thinner than ~20 mm and ~10 mm, respectively. Finally, at both pitches and for a given value of θ_{MAX}, the 20 mm thick BGO scintillators provide higher DQE than CsI:Tl scintillators up to 40 mm thick.

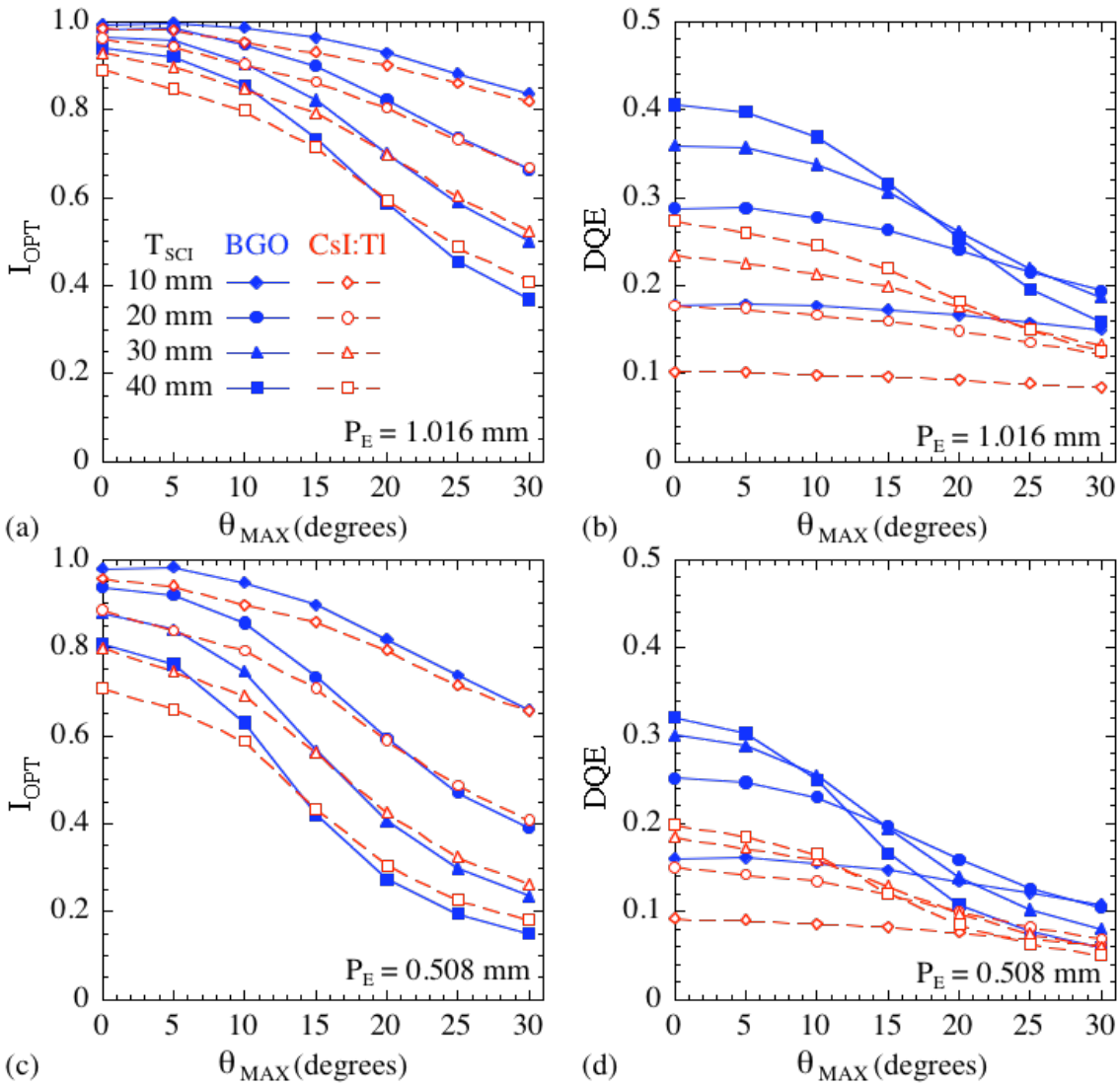

Figure 3.9. Simulation results for I_{OPT} and DQE as a function of the roughness of the side surfaces of scintillating crystals, represented by θ_{MAX}, for 10 to 40 mm thick segmented BGO and CsI:Tl detectors. Results for I_{OPT} and DQE for detectors with 1.016 mm pitch are shown in (a) and (b), while results for detectors with 0.508 mm pitch are shown in (c) and (d), respectively.

The results shown in Figs. 3.9(b) and 3.9(d) indicate that, for all the examined scintillator designs, the drop of DQE with increasing θ_{MAX} is not steep at small values of θ_{MAX}. For purposes of this study, the θ_{MAX} value at which DQE declines to 90% of its value at θ_{MAX} equal to 0° is defined as the roughness resistance of the scintillating crystal

side surfaces, $\theta_{MAX-0.9}$. Figure 3.10 illustrates $\theta_{MAX-0.9}$ values plotted as a function of T_{SCI} for BGO and CsI:Tl at pitches of 1.016 and 0.508 mm. $\theta_{MAX-0.9}$ is seen to decrease in an asymptotic-like manner as T_{SCI} increases. Moreover, at a given T_{SCI}, $\theta_{MAX-0.9}$ is significantly higher for scintillators with the larger pitch. In addition, at the larger pitch, the BGO scintillator provides a higher value of $\theta_{MAX-0.9}$ than its CsI:Tl counterpart, while at the smaller pitch, BGO offers higher $\theta_{MAX-0.9}$ only when T_{SCI} is less than ~30 mm.

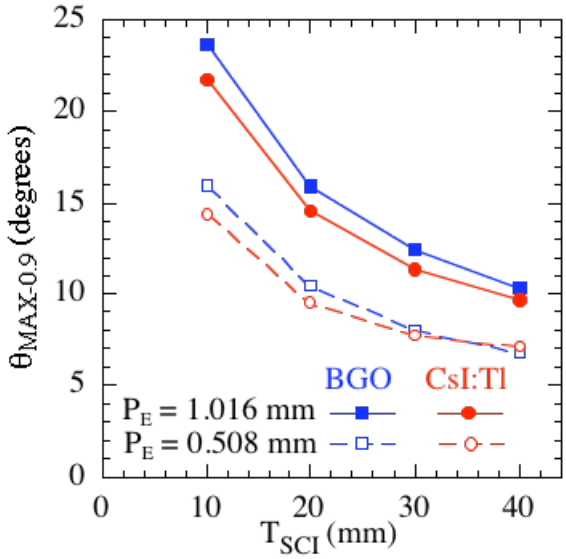

Figure 3.10. Results for the roughness resistance, $\theta_{MAX-0.9}$, of the scintillating crystal side surfaces as a function of T_{SCI}. Results, shown for 10 to 40 mm thick segmented BGO and CsI:Tl detectors at pitches of 1.016 and 0.508 mm, were obtained from the I_{OPT} results appearing in Fig. 3.9.

Figure 3.11 illustrates simulation results for I_{OPT} as a function of ϕ_{SCI} for BGO and CsI:Tl scintillators at θ_{MAX} values of 10° and 20°. The four sets of results shown in this figure were obtained using detector thicknesses varying from 10 to 40 mm and pitches of 0.508, 0.65, 0.8 and 1.016 mm (including some of the results shown in Fig. 3.9). In all simulations, α_{TOP} and α_{WALL} were assumed to be 100% and 2%, respectively. In order to

quantify the trends in these results, each set of simulation results was fit using a fourth-order polynomial function of the form given in Eq. (3.5) and the resulting values of these coefficients are listed in Table 3.3. For all four sets of simulations, I_{OPT} is seen to decrease with increasing ϕ_{SCI}. At a θ_{MAX} value of 10°, BGO consistently offers a higher I_{OPT} than CsI:Tl for all examined ϕ_{SCI}. However, at a θ_{MAX} value of 20°, BGO provides a higher I_{OPT} until ϕ_{SCI} is greater than ~40. Note that no general trends were found when the I_{OPT} results shown in Figs. 3.9 and 3.11 were plotted as a function of $\phi_{SCI} \times \theta_{MAX}$.

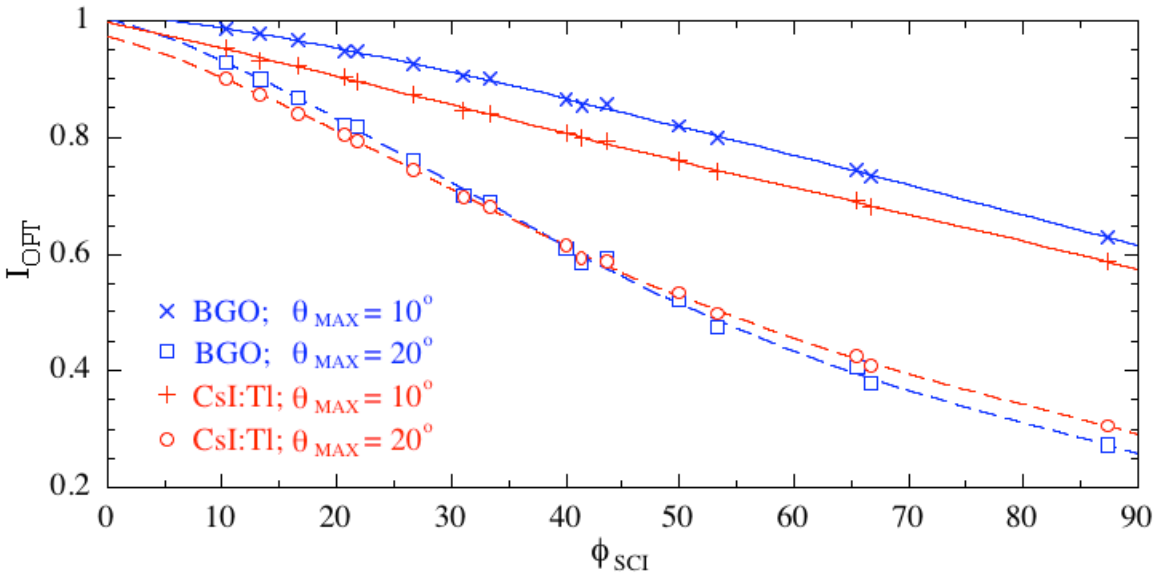

Figure 3.11. Simulation results for I_{OPT} as a function of ϕ_{SCI} for BGO and CsI:Tl detectors at θ_{MAX} of 10° and 20°. The solid and dashed lines correspond to fits to the simulation results using fourth order polynomial functions.

Table 3.3. List of coefficients determined from fits to the simulation results in Fig. 3.11. The fits were based on the fourth order polynomial function shown in Eq. (3.5).

	C_0	C_1	C_2	C_3	C_4
BGO; θ_{MAX} = 10°	1.01×10^{0}	-1.94×10^{-3}	-6.37×10^{-5}	6.30×10^{-7}	-2.53×10^{-9}
BGO; θ_{MAX} = 20°	1.00×10^{0}	-4.92×10^{-3}	-2.49×10^{-4}	3.94×10^{-6}	-1.76×10^{-8}
CsI:Tl; θ_{MAX} = 10°	9.96×10^{-1}	-4.15×10^{-3}	-3.30×10^{-5}	5.83×10^{-7}	-3.15×10^{-9}
CsI:Tl; θ_{MAX} = 20°	9.72×10^{-1}	-5.40×10^{-3}	-1.93×10^{-4}	3.21×10^{-6}	-1.48×10^{-8}

5. Comparison of I_{OPT} for BGO and CsI:Tl

The simulation results reported in Sec IV.C.2 through IV.C.4 indicate that, at a θ_{MAX} of 0°, BGO offers higher I_{OPT} than CsI:Tl. However, as θ_{MAX} increases, this difference in I_{OPT} is reduced and, for thicker scintillators, is eventually reversed. It is believed that this complex behavior is the result of the higher refractive index of BGO (2.15) than that of CsI:Tl (1.79). Since the refractive index of the photodiode array (1.70) is lower than that of both scintillators, total internal reflection occurs at the bottom surface of the scintillating crystals starting at critical angles, γ, of 52° and 72° for BGO and CsI:Tl, respectively. As a result of these different γ values, light photons incident at angles between 52° and 72° can be detected for the CsI:Tl configurations but not for the BGO configurations. For the case of θ_{MAX} equal to 0°, these photons, compared to those incident at angles smaller than 52°, have traveled through pathways that are more oblique to the photodiode array. On average, they have experienced more optical interactions at the partially absorptive septal walls. The detection of these additional photons leads to widening of the optical pulse distribution, reducing I_{OPT} for the CsI:Tl configurations. However, as θ_{MAX} increases, the aforementioned correlation between a photon's incident angle on the bottom surface of the crystals and the number of interactions it incurs is weakened, reducing the difference in I_{OPT} between BGO and CsI:Tl configurations. In the case of larger θ_{MAX} values, the CsI:Tl configuration has the advantage of a higher mean value for the optical pulse distribution, resulting in slightly higher I_{OPT} as observed in Figs. 3.9 and 3.11.

V. SUMMARY AND DISCUSSION

The theoretical investigation of optical Swank noise and DQE reported in this chapter demonstrates how Monte Carlo simulation of radiation and optical transport can be used to explore the numerous parameter choices involved in the design of segmented scintillators so as to achieve optimized prototypes that provide significantly improved DQE compared to conventional EPIDs based on AMFPI technology.

The simulation results reported in this study demonstrate that optical Swank factor (I_{OPT}) is larger for segmented scintillators with smaller scintillating crystal aspect ratio (ϕ_{SCI}), i.e. smaller scintillator thickness (T_{SCI}) and/or larger element pitch (P_E). Although larger P_E leads to higher DQE at zero spatial frequency, it is necessary to insure that the element pitch is sufficiently small so as to avoid significant loss of spatial resolution and DQE at high spatial frequencies (as described in Sec II of Chapter 2). At a given value of ϕ_{SCI}, I_{OPT} generally decreases with increasing scintillating crystal absorption and scattering coefficients (μ_{A-SCI} and μ_{S-SCI}, respectively), top reflector absorptivity (α_{TOP}), septal wall absorptivity (α_{WALL}), as well as scintillating crystal side surface roughness (θ_{MAX}). Among these five properties, only α_{WALL} and θ_{MAX} significantly degrade DQE at ϕ_{SCI} values greater than ~20 (e.g., for 10 and 20 mm thick detectors at pitches of 0.508 and 1.016 mm, respectively). In addition, the results shown in Figs. 3.7 and 3.9 can be used to determine the value of α_{WALL} and θ_{MAX} beyond which a thicker scintillator does not improve DQE. For example, for BGO at a pitch of 0.508 mm, DQE does not increase as T_{SCI} increases from 30 mm to 40 mm when α_{WALL} is greater than ~3% (at θ_{MAX} of 0°) or when θ_{MAX} is larger than ~8° (at α_{WALL} of 2%).

At θ_{MAX} equal to 0°, the results shown in Fig. 3.8 (and the corresponding fitting coefficients listed in Table 3.2) can be used to estimate I_{OPT} for EPIDs employing segmented scintillators having values of T_{SCI}, P_E and α_{WALL} that are not specifically examined in this study. Note that such estimates may not be valid beyond the examined parameter ranges. Moreover, since the results in Fig. 3.6 indicate that I_{OPT} decreases approximately linearly with increasing α_{TOP}, the results shown in Fig. 3.8 can also be used to estimate I_{OPT} for α_{TOP} values between 0% and 100%. In addition, at θ_{MAX} of 10° and 20°, the results illustrated in Fig. 3.11 (and the corresponding fitting coefficients shown in Table 3.3) can be used to estimate I_{OPT} for scintillators having values of T_{SCI} and P_E within the examined range of parameters, but not specifically studied. Finally, in the development of future prototype scintillators, the roughness resistance ($\theta_{MAX-0.9}$) values shown in Fig. 3.10 can provide guidance for avoiding significant loss of DQE due to scattering at the side surfaces of the scintillating crystals.

Note that the septal walls in actual scintillators consist of polymer reflectors glued to scintillating crystals. The probability of refraction at the surface adjoining the glue and crystal, calculated using refractive indices (~1.55, 2.15 and 1.79 for glue, BGO and CsI:Tl, respectively) and integrated over all incident angles, is ~47% and 64% for BGO and CsI:Tl scintillators, respectively. Most of the light refracted into the transparent glue layer is reflected by the polymer reflector, which typically has a reflectivity of ~90% or higher. Consequently, the probability for an optical photon to enter the polymer reflector (for a given interaction at the septal wall) is ~4.7% and 6.4% for BGO and CsI:Tl,

respectively. Photons entering the reflector are either absorbed in the reflector, with a probability determined by α_{WALL}, or transmitted into adjacent elements. Given the high level of optical crosstalk observed from the prototype CsI:Tl scintillators (results to be shown in the next chapter), it is estimated that most photons entering the reflector are transmitted and therefore α_{WALL} for polymer septal walls is significantly smaller than 6.4%.

The roughness of the crystal side surfaces can be measured by means of extracting a profile of the surface topology from which a distribution of the θ angles of local micro-facets can be determined. Such a distribution (not yet available at this stage of the project) would allow the establishment of a correspondence between the measured roughness and the θ_{MAX} value used in the simulations.

The scintillators reported in the Results section assume the use of polystyrene septal walls that have radiation properties generally consistent with the type of polymer reflectors used in recent prototype scintillators.[14, 15] Alternatively, septal walls could conceivably be made of high-density metal (e.g., silver foil or tungsten powder with reflective coating). In radiation simulations carried out for BGO and CsI:Tl scintillators involving 0.05 mm thick tungsten walls, the replacement of polymer walls with tungsten walls was found to result in higher DQE_{RAD} – by up to ~0.04 and 0.08 at pitches of 1.016 and 0.508 mm, respectively. However, metal walls are typically more absorptive (e.g., with α_{WALL} greater than 10%) than polymer walls, resulting in lower I_{OPT} that may mitigate any gain in DQE due to increase in QE. If it were possible to reduce the optical

absorption of metal walls to a level comparable to that of polymer walls, the I_{OPT} behaviors reported in the Results section should also be applicable to scintillator configurations employing metal walls.

REFERENCES

[1] A. Sawant, L. E. Antonuk, Y. El-Mohri, Q. Zhao, Y. Li, Z. Su, Y. Wang, J. Yamamoto, H. Du, I. Cunningham, M. Klugerman and K. Shah, "Segmented crystalline scintillators: an initial investigation of high quantum efficiency detectors for megavoltage x-ray imaging," Medical Physics **32**, 3067-3083 (2005).

[2] T. T. Monajemi, B. G. Fallone and S. Rathee, "Thick, segmented CdWO4-photodiode detector for cone beam megavoltage CT: a Monte Carlo study of system design parameters," Medical Physics **33**, 4567-4577 (2006).

[3] Y. Wang, L. E. Antonuk, Y. El-Mohri and Q. Zhao, "A Monte Carlo investigation of Swank noise for thick, segmented, crystalline scintillators for radiotherapy imaging," Medical Physics, under review (2009).

[4] A. Badano and J. Sempau, "MANTIS: combined x-ray, electron and optical Monte Carlo simulations of indirect radiation imaging systems," Physics in Medicine and Biology **51**, 1545-1561 (2006).

[5] F. Salvat, J. M. Fernández-Varea and J. Sempau, "PENELOPE, A code system for monte carlo simulation of electron and photon transport," (2003).

[6] A. Badano, Ph.D. Thesis, University of Michigan, 1999.

[7] A. Badano, R. M. Gagne, B. D. Gallas, R. J. Jennings, J. S. Boswell and K. J. Myers, "Lubberts effect in columnar phosphors," Med Phys **31**, 3122-3131 (2004).

[8] L. E. Antonuk, Y. Wang, M. Behravan, Y. El-Mohri, Q. Zhao, H. Du and A. Badano, "Quantitative exploration of performance enhancements offered by active matrix x-ray imagers fabricated on plastic substrates," Proceedings of SPIE Conference on the Physics of Medical Imaging **6510**, 65100P-65101 to 65100P-65110 (2007).

[9] Product data sheet for Cesium Iodide scintillation material, Saint-Gobain Crystals, OH, U.S.

[10] Product data sheet for Bismuth Germanate scintillation material, Saint-Gobain Crystals, OH, U.S.

[11] L. E. Antonuk, Y. El-Mohri, W. Huang, K.-W. Jee, J. H. Siewerdsen, M. Maolinbay, V. E. Scarpine, H. Sandler and J. Yorkston, "Initial performance evaluation of an indirect-detection, active matrix flat-panel imager (AMFPI) prototype for megavoltage imaging," International Journal of Radiation Oncology Biology Physics **42**, 437-454 (1998).

[12] D. Sheikh-Bagheri, Ph.D. Thesis, Carleton University, 1999.

[13] Private communication with Saint-Gobain Crystals, OH, U.S.

[14] A. Sawant, L. E. Antonuk, Y. El-Mohri, Q. Zhao, Y. Wang, Y. Li, H. Du and L. Perna, "Segmented crystalline scintillators: empirical and theoretical investigation of a high quantum efficiency EPID based on an initial engineering prototype CsI(Tl) detector," Medical Physics **33**, 1053-1066 (2006).

[15] Y. Wang, Q. Zhao, L. E. Antonuk, Y. El-Mohri and L. Perna, "High-DQE EPIDs based on thick, segmented BGO and CsI:Tl scintillators: Performance evaluation at extremely low dose," Medical Physics, under review (2009).

CHAPTER 4

SEGMENTED SCINTILLATORS: EMPIRICAL AND THEORETICAL INVESTIGATIONS ON PROTOTYPE EPIDS

I. INTRODUCTION

The Monte Carlo study of radiation and optical transport reported in the previous chapter indicated that EPIDs employing segmented CsI:Tl and BGO scintillators up to 40 mm thick can provide DQE of up to ~29% and 42% (corresponding to ~29 and 42 times that of the conventional EPID), respectively.[1] As an initial step in our empirical investigation, a 40 mm thick prototype CsI:Tl scintillator was evaluated using a 6 MV photon beam.[2] An EPID employing this scintillator exhibited a measured DQE of ~22% at zero spatial frequency. However, at higher spatial frequencies, the MTF and DQE of this prototype exhibited significant fall-off due to insufficient optical isolation and sub-optimal alignment between scintillator elements.

Building upon the experience gained from this earlier CsI:Tl prototype, three new CsI:Tl prototypes and one BGO prototype have been fabricated and evaluated. The signal and noise properties, as well as phantom images, acquired from these prototype EPIDs are reported in this chapter and compared to results obtained from the conventional EPID. Finally, the performance limitations for these prototype EPIDs and the direction for future scintillator development are discussed. Note that the figures and

the table used in this chapter, with the exception of Figs. 4.2 and 4.3, were taken from a manuscript submitted to the *International Journal of Medical Physics Research and Practice* by the author of this dissertation.[3]

II. METHODS AND MATERIALS

A. PHYSICAL DESCRIPTION OF PROTOTYPE EPIDS

The four prototype scintillators include an 11.3 mm thick BGO scintillator and three CsI:Tl scintillators (referred to as CsI-1, CsI-2 and CsI-3) with thicknesses of 11.4, 25.6 and 40.0 mm, respectively. (Note that CsI-1 and CsI-2 were obtained by slicing CsI-3 into two thinner, independent parts.) Each scintillator consists of 120 × 60 scintillator elements with an element pitch of 1.016 mm, offering an active area of ~12.2 × 6.1 cm^2. The septal walls are 0.05 mm thick and consist of polymer reflectors (with a reflectivity of ~90%) glued to scintillating crystals. The reflectors are not entirely opaque to optical photons, resulting in some light sharing between adjacent elements. The top and bottom surfaces of all scintillators were processed using the same polishing technique. Moreover, the BGO and CsI:Tl crystals were cut using the same saw. However, due to the higher physical hardness of BGO, all crystal surfaces of the BGO scintillator are much smoother.

Figure 4.1(a) shows a picture illustrating the high transparency of the BGO scintillator. Most of the elements of this scintillator exhibit no significant optical absorption or scattering. Figure 4.1(b) shows a picture taken with the CsI-1 scintillator against the same underlying photograph. In this case, however, the flamingos were

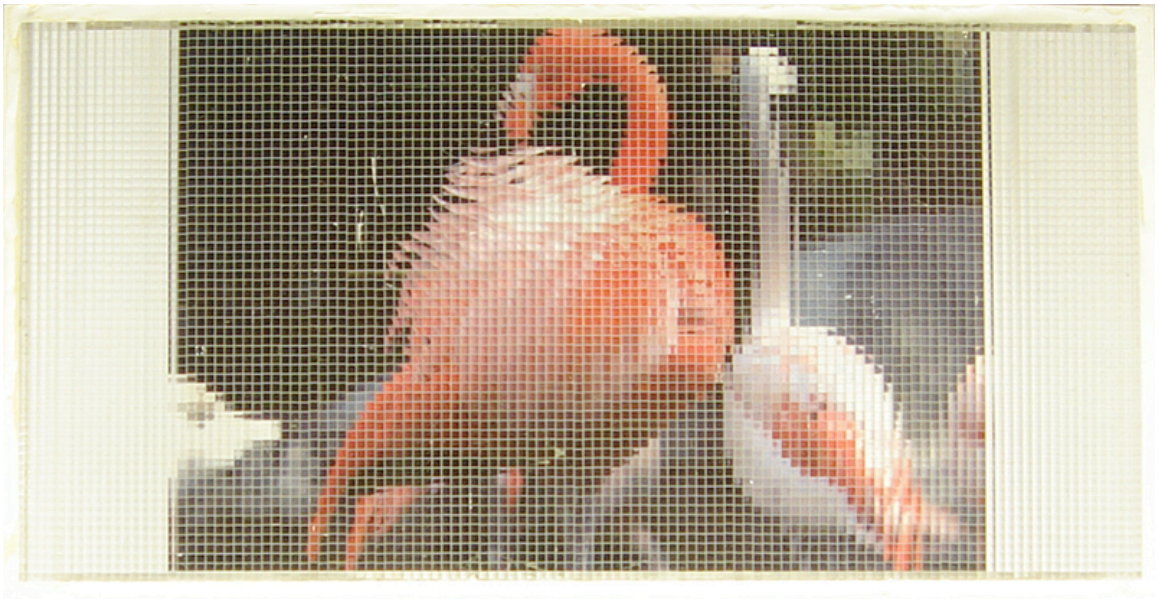

(a)

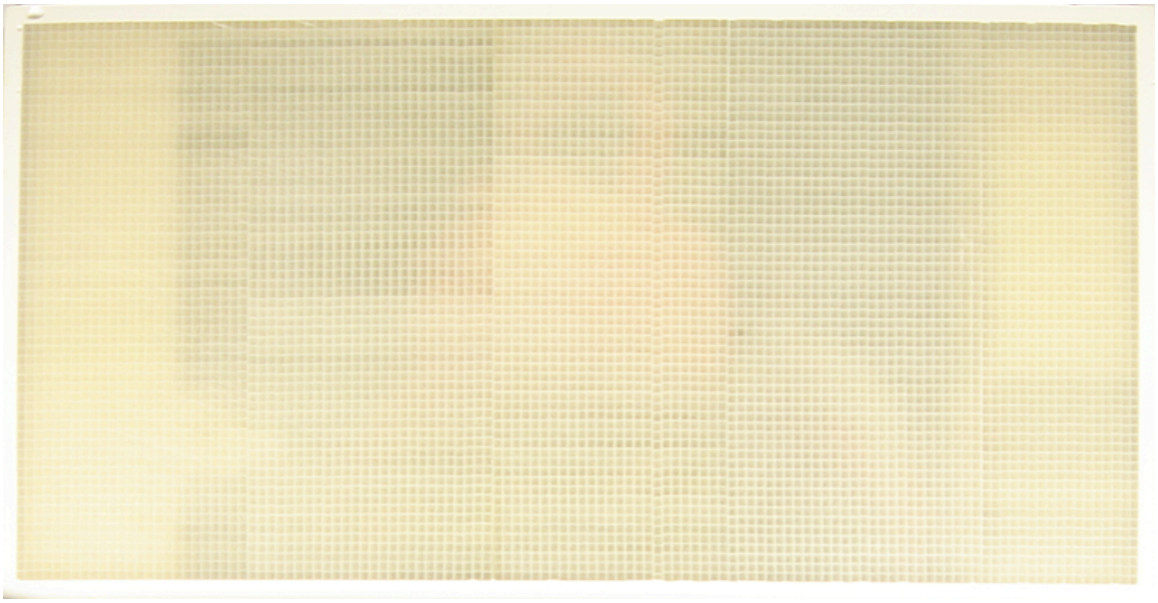

(b)

Figure 4.1. Pictures showing a top view of the segmented (a) BGO (11.3 mm thick) and (b) CsI-1 (11.4 mm thick) scintillators overlying the same photograph of two flamingos. Note that the photograph is narrower than the scintillators. The light grid of horizontal and vertical lines corresponds to the septal walls of the prototypes. The BGO scintillator is seen to be more transparent than the CsI-1 scintillator. Also note that the BGO and CsI-1 scintillators were assembled from seven and five sub-assemblies (each consisting of 60 rows of elements), respectively. Although the transparencies of the various sub-assemblies are very similar for the BGO scintillator, this is not the case for the CsI-1 scintillator.

barely visible. Moreover, the CsI-1 scintillator appears to be much less transparent than the BGO scintillator, and exhibits an ivory color. It is believed that the difference in light transmission between the two scintillators is mainly due to the difference in optical scattering. Such a difference is the consequence of the inherently higher degree of self-scattering in the CsI:Tl crystal, as well as higher scattering at the much rougher surfaces of that scintillator.

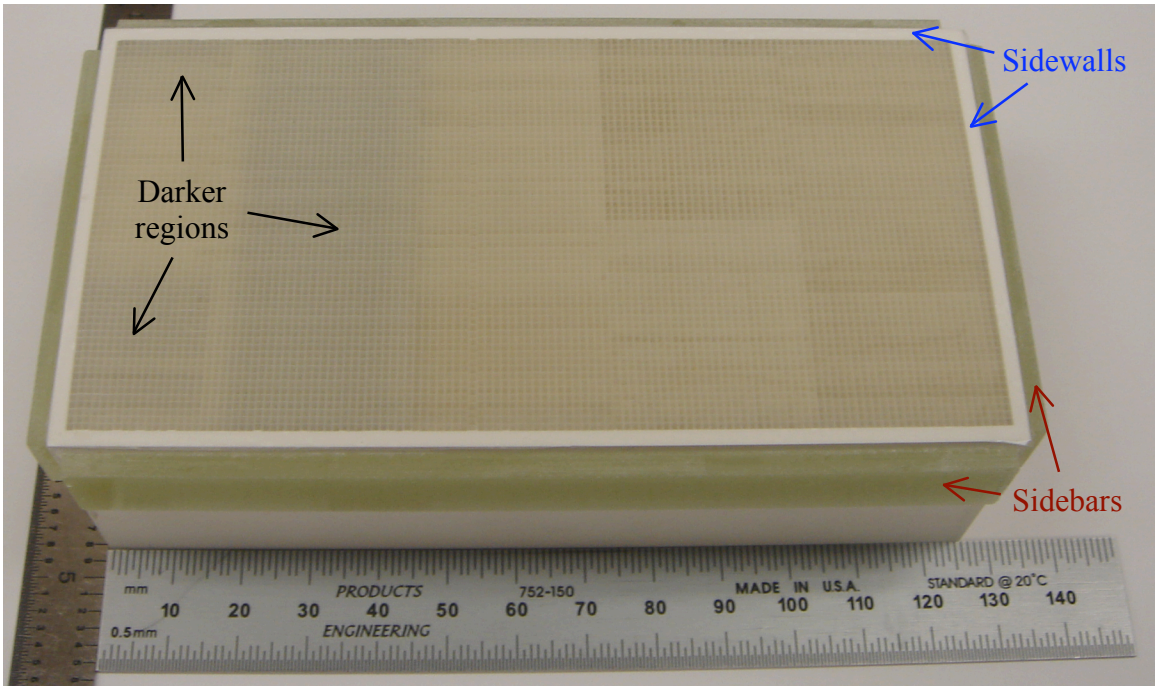

Figure 4.2. Picture of the CsI-3 scintillator placed on a uniform piece of white paper. The black arrows indicate regions in the scintillator that offer significantly lower signal response than other regions. The blue arrows indicate sidewalls surrounding the scintillator, which were used to seal and protect the scintillator. The brown arrows indicate sidebars attached to the sidewalls, which were used to mount the scintillator to a custom-built alignment jig (as shown in Fig. 4.3).

Figure 4.2 shows a picture of the CsI-3 scintillator placed on a uniform piece of white paper. Two regions of the scintillator, indicated by black arrows, appear to be slightly darker than the rest of the scintillator. Note that the same regions in the CsI-1 and CsI-2

scintillators also appear darker. The "darker regions" in the CsI:Tl scintillators are found to offer significantly lower signal response under a 6 MV photon beam. It is suspected that these regions were mistakenly fabricated with septal walls that have different properties than other regions. Note that data from these regions were not used for the performance evaluation for the prototype EPIDs.

Each segmented scintillator was covered by a 1 mm thick copper plate with a polished mirror surface, forming a segmented scintillating detector. The copper plate absorbs scattered radiation and also serves as a radiation build-up layer. Each segmented detector was configured with a mirror or a black top reflector. The mirror top reflector configuration utilizes the polished mirror surface of the copper plate, resulting in a estimated reflectivity of ~60% to 70%. The black top reflector configuration employs a sheet of black paper positioned between the copper plate and the segmented scintillator.

The segmented detectors were evaluated using the Cyclops II array (see Sec. III.B.3 in Chapter 1 for detailed specifications).[4] The detector and array were housed in a custom-built, precision alignment jig as shown in Fig. 4.3.[2] This jig allowed horizontal, vertical and rotational adjustment of the segmented scintillator with respect to the underlying array. Before x-ray measurements, each scintillator was aligned with the array so as to register each scintillator element with a block of 2 × 2 array pixels. In addition, due to the high optical conversion gain of CsI:Tl (~54,000 photons/MeV),[5] a 0.05 mm thick neutral density filter with 12% light transmission (Cinegel #3404, Rosco Laboratories Inc., Stamford, CT) was placed between the CsI:Tl scintillator and the array so as to

prevent pixel signal saturation. For comparison, x-ray measurements were also performed with the conventional EPID (see Sec. III.B.3 in Chapter 1) employing a phosphor screen detector with a black top reflector.

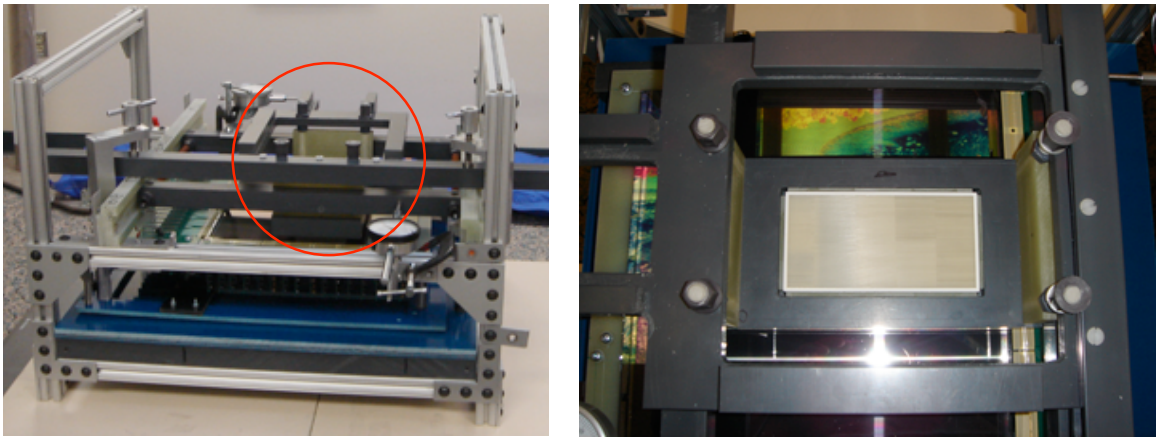

(a) (b)

Figure 4.3. (a) A side view picture of the alignment jig and (b) a top view picture of the part that holds the CsI-3 scintillator. The red circle in (a) indicates the position of the scintillator in the alignment jig.

B. MEASUREMENT METHODS

The prototype and conventional EPIDs were evaluated using a 6 MV photon beam from a Varian 21EX LINAC. The radiation output of the LINAC is measured in monitor units (MU). For each MU, the LINAC delivers ~36 beam pulses. The LINAC was calibrated so that at 6 MV with an open field of 10 × 10 cm^2, an irradiation of 1 MU deposits a dose of ~0.8 cGy in water at a source-to-detector distance (SDD) of 100 cm, with 10 cm overlying water. For all reported radiation measurements (i.e., x-ray sensitivity, MTF, NPS, DQE and phantom images), unless otherwise stated, the size of the x-ray field was 15 × 15 cm^2 at isocenter and the LINAC was operated at a dose rate of 100 MU/min.

Measurements involving the BGO prototype were immediately preceded by an irradiation of ~2000 MUs. This procedure was necessary to stabilize the sensitivity of the prototype, which exhibited a sharp decline (~17%) in response to this initial radiation to reach an asymptotic, stable level. Additional measurements indicated that this behavior is caused by short-term radiation-induced discoloration of the BGO crystal. The sensitivity recovered after approximately one week and this behavior was found to be highly reproducible.

1. X-ray sensitivity

X-ray sensitivity and NPS were determined using the same data acquired both in the presence and absence of radiation (referred to as flood and dark frames, respectively). For these measurements, the entrance surface of the EPIDs (i.e., the top surface of the copper plate) was ~130 cm from the radiation source. The flood frames were obtained in fluoroscopic mode, which involves the acquisition of consecutive data frames in synchronization with the beam pulses. The array readout was synchronized with the "Target I" output from the LINAC control logic. Flood frames were obtained under various irradiation conditions corresponding to the delivery of a constant number of beam pulses per frame (i.e., 1 to 4 pulses, corresponding to calibration doses of 0.022 to 0.089 cGy). As a result of the synchronization, the frame time, defined as the time interval between consecutive frames, varied with dose and ranged from 16.7 to 66.7 ms. For each dose, 900 flood frames, each consisting of 512 gate lines by 100 data lines, were acquired. The first 400 frames were discarded as they were only used to stabilize LINAC

output and pixel signal. The remaining 500 frames were used for sensitivity and NPS determination. Correspondingly, 500 dark frames were obtained for each dose using the same frame time to allow gain and offset corrections. A smaller region of interest (ROI), consisting of 180 × 100 and 140 × 100 pixels for the BGO and CsI:Tl prototypes, respectively, was selected away from the edges of the scintillator. The "darker regions" (see Fig. 4.2) were excluded from the selected ROI for the CsI:Tl prototypes.

As a first step in processing of the data, gain and offset corrections were applied to the ROI in the flood frames. Subsequently, defective array pixels were corrected with a 3 × 3 median filter, affecting less than 0.2% of the total number of pixels. The corrected frames were then binned in a 2 × 2 format, resulting in a synthesized pixel size equal to that of the scintillator elements. These processing steps were applied to all data frames obtained from the prototypes as well as from the conventional EPID. The signal, measured in analog-to-digital converter (ADC) units, was converted to electrons using a calibration factor of 7480 electrons/ADC.[6] For each prototype and for the conventional EPID, the average signal per binned pixel ($\bar{S}$) plotted as a function of calibration dose was fit with a linear function, the slope of which yielded the x-ray sensitivity.

2. Normalized NPS (NNPS)

NPS was determined from the processed flood frames using the synthesized slit technique.[4] For each dose, the 500 processed frames were averaged along the data line direction, forming 500 independent, 1D realizations. After removing low frequency trends and applying a Hanning window, a 1D Fourier transform was applied to each of

the 500 realizations. The resulting 500 power spectra were appropriately normalized and averaged to yield NPS. A correction for lag (i.e., frame-to-frame signal carryover, mainly caused by charge trapped in the a:Si-H photodiode) was applied to yield a lag-corrected NPS, NPS_L.[7] The normalized NPS, NNPS, was determined using:

$$NNPS(f) = \frac{NPS_L(f) \times \bar{q}_0}{\bar{S}^2}, \tag{4.1}$$

where f is spatial frequency and $\bar{q}_0$ is the incident x-ray fluence. For a calibration dose of 1 cGy, $\bar{q}_0$ is ~1.73×10^7 X rays/mm^2 at a SDD of 100 cm.

3. MTF

Spatial resolution of the prototype EPIDs was characterized in terms of the pre-sampled MTF, using the angled slit technique.[2, 8] A custom-made slit used in these measurements consists of two $4.25 \times 8.5 \times 19$ cm^3 tungsten blocks separated by a $0.01 \times 8.5 \times 19$ cm^3 polymer shim (forming a narrow gap under the therapy beam).[8] The slit was attached to the LINAC using an accessory mount, with the gap oriented along the direction of the beam. The gap was positioned at an angle of ~3° with respect to the direction of the data lines of the array. The entrance surface of the slit was ~119 cm from the radiation source (resulting in a SDD of 138 cm) and the radiation field was ~4.0×5.5 cm^2 at isocenter. The LINAC was operated at a dose rate of 600 MU/min. The slit was initially positioned at the center of the field so as to allow maximum radiation transmission through the gap. 10 images of the slit were acquired in radiographic mode (involving the acquisition of a single data frame following each x-ray irradiation). For each prototype configuration, 10 additional images, referred to as radiation dark images,

were acquired after displacing the gap by ~5 mm away from the centered position so that no direct radiation could transit the gap. These images were used to correct for the small amount of radiation penetrating through the tungsten blocks. After image processing (see the last paragraph in Sec. II.B.1 for details), the average of the radiation dark images was subtracted from the average of the slit images, and the resulting image was used to determine the line spread function (LSF). Application of a 1D Fourier transform to the LSF yielded the MTF.

4. DQE

For each dose at which NPS data were acquired, DQE was determined using the measured results for MTF and NNPS:

$$DQE(f) = \frac{MTF^2(f)}{NNPS(f)} \tag{4.2}$$

5. Phantom images

X-ray images of a contrast-detail phantom were acquired using the prototype EPIDs. This aluminum phantom consists of holes of 10 different depths and 10 different diameters.[2, 4] Due to the limited size of the prototype scintillators, only a portion of the phantom was imaged, corresponding to a set of 8 × 3 holes providing the highest contrasts (0.18% to 1.91% at 6 MV) and largest diameters (0.5 to 1.3 cm). In addition, part of a human head phantom (Model 76-018DT, Nuclear Associates, Long Island, NY) was imaged using the BGO prototype. For comparison, images of the phantoms were also obtained using the conventional EPID. For all images, the EPIDs were placed at a SDD of 130 cm with the phantoms secured ~20 cm above the EPIDs.

C. SIMULATION METHODS

In order to compare the measured performance of the prototype EPIDs to theoretical predictions, Monte Carlo simulations of radiation transport were performed to determine MTF, NNPS, and DQE, using the EGSnrc [9] and DOSXYZnrc [10] codes. Simulations of optical transport were not included. Consequently, the simulated MTF and DQE correspond to theoretical upper limits for the prototype EPIDs. Each simulated EPID consists of a segmented scintillator covered by a 1 mm thick copper plate, as shown in Fig. 3.2. Note that the flat-panel array was not included in these simulations due to its negligible impact on the radiation transport in the segmented scintillating detector. The scintillator thickness and element-to-element pitch used in the simulations correspond to those of the prototype scintillators. The septal walls were simulated as 0.05 mm thick layers of polystyrene. The simulated scintillators consist of 300 × 300 and 600 × 600 elements for simulations of MTF and NNPS, respectively. The imaging signal was obtained from the radiation energy absorbed in each scintillating crystal.

The angled slit method was used for the simulation to determine MTF.[11] A simulated parallel beam of 30 × 0.01 cm^2, perpendicularly incident on the center of each detector, formed a thin radiation slit oriented at a small angle (~1°) with respect to the column direction of the scintillators. The 1D Fourier transform of the resulting LSF, extracted from the slit image, yielded the simulated MTF.

The synthesized slit method was used in the simulation to determine NPS. A 60 × 60 cm^2 parallel beam was generated perpendicularly incident on the central part of each detector (having an area of ~61 × 61 cm^2). A total of 50 flood frames were simulated for each EPID, with 360 million x-ray histories carried out for each frame. Data from ten non-overlapping blocks, each consisting of 250 × 100 elements, were obtained from the central 500 × 500 elements of each frame. Data in each of the resulting 500 blocks was averaged along the shorter dimension, resulting in 500 realizations. A 1D Fourier transform was applied to each of the 500 realizations. The resulting 500 power spectra were appropriately normalized and averaged to yield the simulated NPS,[11] from which the simulated NNPS was determined [see Eq. (4.1)]. Given the number of simulated X rays (360 million) and the beam size (60 × 60 cm^2), $\bar{q}_0$ is equal to 1000 X rays/mm^2. Finally, simulated DQE was calculated using Eq. (4.2) and the simulated MTF and NNPS results. Due to the absence of electronic noise in the simulations, the NNPS and the associated DQE results are independent of dose.

III. RESULTS

For the various types of measurements reported for the prototype EPIDs, comparisons are made with the performance of the conventional EPID. The results for the conventional EPID were either acquired for the present study (in the case of x-ray sensitivity and phantom images) or obtained from previously published data for that EPID (in the case of MTF and DQE).[4] In all cases, the data were binned in a 2 × 2 format to match the element-to-element pitch of the segmented scintillators.

A. X-RAY SENSITIVITY

In Fig. 4.4, the average signal per binned pixel ($\bar{S}$) is presented as a function of calibration dose for the prototype EPIDs. Results are shown for the prototypes

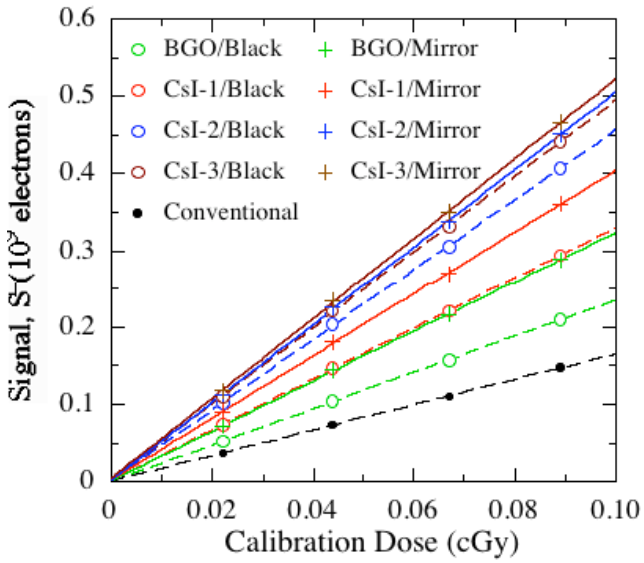

Figure 4.4. Average signal per binned pixel as a function of calibration dose for the four prototype EPIDs. Results for each prototype, configured with the black top reflector (open circles) and with the mirror top reflector (plus symbols), are shown. For comparison, the average signal for the conventional EPID is also plotted (black dots). The dashed and solid lines are linear fits to the data.

Table 4.1. X-ray sensitivities, derived from the EPID signal data appearing in Fig. 4.4, are listed in the first two rows. The percentages reported in the third row correspond to the degree of sensitivity enhancement that results from the replacement of the black top reflector with the mirror top reflector.

	BGO	CsI-1	CsI-2	CsI-3	Conventional
Black top reflector, 10^9 e/cGy	1.52	2.12	2.94	3.18	1.06
Mirror top reflector, 10^9 e/cGy	2.08	2.60	3.25	3.35	—
Sensitivity enhancement using the mirror top reflector	37%	23%	11%	5%	—

configured with the black and the mirror top reflectors, as well as for the conventional EPID. The signal response for each of the prototypes is seen to be highly linear. The corresponding x-ray sensitivities, determined from linear fits to the signal response data,

are summarized in Table 4.1. For each prototype configuration, the sensitivity is found to be higher than that for the conventional EPID, even with the neutral density filter used to attenuate signal for all CsI:Tl prototypes. In addition, for a nearly identical scintillator thickness, CsI-1 offers higher sensitivity than the BGO prototype. For BGO, CsI-1, CsI-2 and CsI-3, the replacement of the black top reflector with the mirror top reflector leads to sensitivity enhancements of ~37%, 23%, 11% and 5%, respectively. The enhancement for the CsI-1 prototype is smaller than that for the BGO prototype due to less efficient light transmission in the CsI-1 scintillator. In addition, for the three CsI:Tl prototypes, the enhancement of sensitivity decreases with increasing thickness, indicating a reduction in the efficiency of optical transport with increasing scintillator thickness.

B. MTF

Figure 4.5 shows pre-sampled MTF measured from the prototype EPIDs. Results are shown for the prototypes configured with the black and the mirror top reflectors, along with the corresponding theoretical upper limits obtained through simulation of radiation transport, as well as the MTF measured from the conventional EPID. The measured MTFs of the prototype EPIDs are seen to be much lower than both the corresponding theoretical upper limits and the MTF of the conventional EPID. The difference between the measured and the simulated prototype MTF results is believed to be the combined result of lateral optical spreading, as well as misalignment between scintillator elements and misregistration between the scintillator elements and the array pixels – none of which is accounted for in the simulations. The latter two effects will be referred to as

"misalignment" and "misregistration" in the remainder of this chapter, and those photons that enter neighboring elements will be referred to as *lateral spreading photons*.

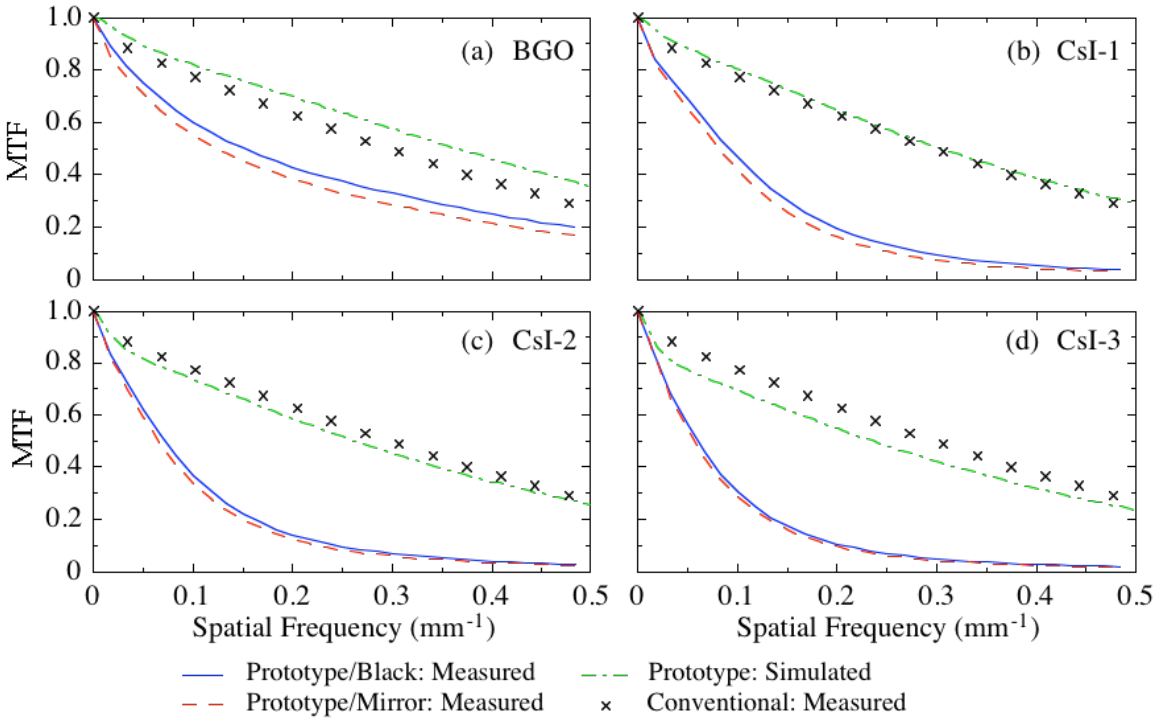

Figure 4.5. Pre-sampled MTF results obtained from the (a) BGO, (b) CsI-1, (c) CsI-2 and (d) CsI-3 prototype EPIDs. The results are shown for configurations with the black top reflector (blue lines) and the mirror top reflector (red dashed lines). The green dot-dashed lines correspond to the MTF obtained from simulation of the various prototypes. The black crosses correspond to MTF results measured from the conventional EPID (adapted from data appearing in Ref. 4).

The BGO prototype empirically exhibits significantly higher MTF than the CsI-1 prototype. Given the similar degree of misalignment and misregistration present in these two prototypes of almost identical thicknesses, the difference in MTF performance is likely due to differences in the amount of lateral optical spreading. Since the same polymer reflector and optical glue were nominally used in all prototype scintillators, it is suspected that the superior element-to-element optical isolation demonstrated by the

BGO scintillator is the combined result of its higher refractive index and lower optical scattering. Given that the refractive indices of the optical glue (~1.55) and the flat-panel array (~1.70) are both lower than that of BGO (~2.15) and CsI:Tl (~1.79), total internal reflection can occur at the scintillator-glue interface (i.e., at the side surfaces of the scintillator crystals) and the scintillator-array interface (i.e., at the bottom surfaces of the scintillator crystals). At the scintillator-glue interface, photons incident at angles larger than the critical angle (~46° and 60° for BGO and CsI:Tl, respectively) cannot exit the crystal and cannot spread into neighboring elements. This limiting effect on lateral optical spreading is stronger for the BGO scintillator due to its smaller critical angle. At the scintillator-array interface, photons incident at angles larger than the critical angle (~52° and 72° for BGO and CsI:Tl, respectively) cannot enter the flat-panel array. For the BGO scintillator (having little or no optical scattering), the lateral spreading photons (those with incident angles smaller than ~46° at the scintillator-glue interface) have incident angles larger than ~44° at the scintillator-array interface. A significant portion of those lateral spreading photons cannot enter the flat-panel array and thus do not contribute to imaging signal. This effect, which helps to improve MTF for the BGO scintillator, is strongly suppressed for the CsI:Tl prototypes due to its lower refractive index and greater optical scattering.

From Fig. 4.5, the EPID configurations with the mirror top reflector are observed to show slightly lower MTF performance than the configurations with the black top reflector. This is likely due to a greater degree of lateral spreading of those photons reflected by the mirror top reflector. In addition, as expected, the spatial resolution for

the CsI:Tl prototypes decreases with increasing scintillator thickness due to increased lateral spreading of secondary radiation and optical photons. Finally, although the MTF measured from each prototype EPID is lower than that for the conventional EPID, the BGO prototype nevertheless demonstrates relatively good performance – for example, providing an MTF of ~20% near the Nyquist frequency of 0.49 mm^{-1}.

C. NNPS

Figure 4.6 shows measured and simulated NNPS for the prototype EPIDs. For each prototype, the NNPS measured at 0.022 and 0.044 cGy (corresponding to 1 and 2 beam pulses, respectively) are generally similar, indicating a noise performance dominated by x-ray quantum noise. In addition, the configurations with the black top reflector exhibit slightly higher NNPS – likely the result of two contributing factors. The first is an increase in Swank noise at all frequencies for the black reflector configurations, originating from the increase in the difference in optical gain for photons generated at different depths in the scintillator. The second factor is a higher degree of optical spreading for the mirror reflector configurations (see Fig. 4.5), leading to stronger element-to-element signal correlation and thus lower NNPS. Compared to the CsI:Tl prototypes, the BGO prototype exhibits significantly less decline in NNPS at higher spatial frequencies, indicating a much smaller element-to-element signal correlation – a consequence of reduced lateral optical spreading. The large difference observed between the measured and simulated NNPS is the combined result of four effects that have not been included in the simulations: noise reduction caused by lateral optical spreading, optical Swank noise, as well as noise resulting from misalignment and misregistration.

While the first two effects lead to stochastic noise propagation, the latter two result in deterministic noise propagation. Finally, at four specific spatial frequencies, all NNPS results for the various prototypes show small bumps, the origin of which is not understood – but which are possibly associated with pickup of ambient electromagnetic noise.

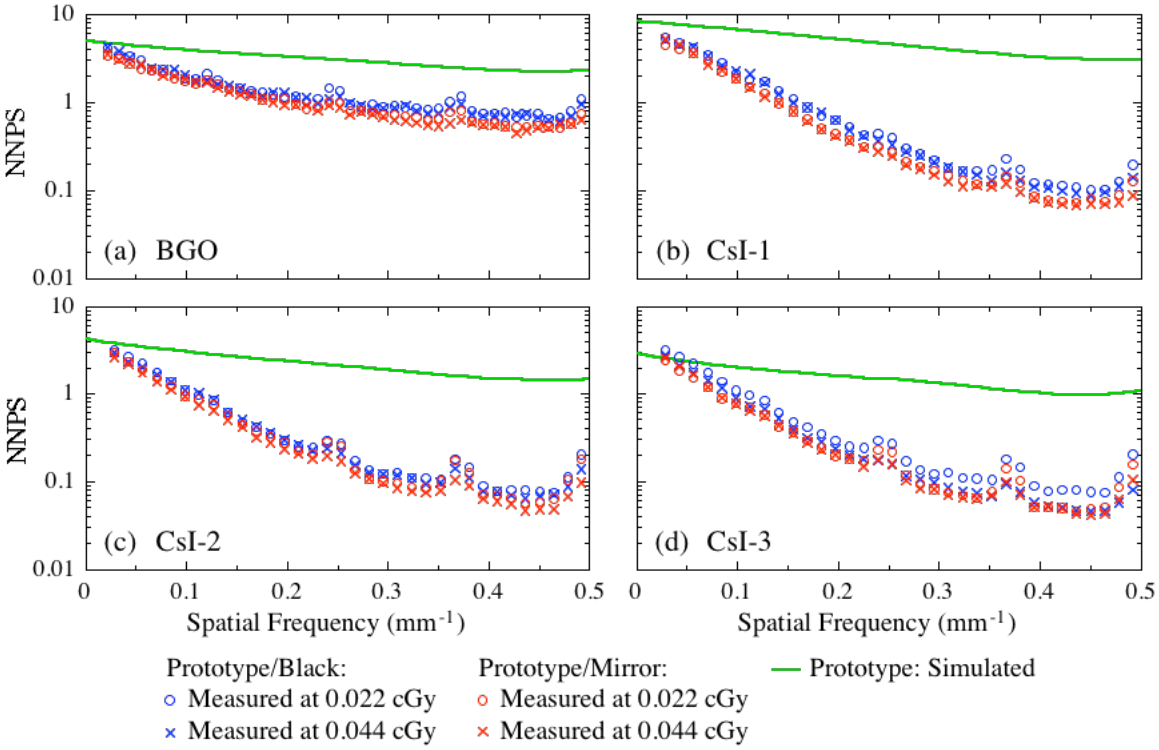

Figure 4.6. NNPS for the (a) BGO, (b) CsI-1, (c) CsI-2 and (d) CsI-3 prototype EPIDs. Results are shown for configurations with the black top reflector (blue symbols) and the mirror top reflector (red symbols), at both 0.022 and 0.044 cGy. The green lines correspond to polynomial fits to the NNPS results obtained through simulation.

D. DQE

Figure 4.7 shows measured DQE results at 0.022 and 0.044 cGy for the prototype EPIDs configured with the black and the mirror top reflectors, along with corresponding DQE values determined from Monte Carlo simulations. The DQE for the conventional

EPID, measured at 1 cGy, is also shown. (Note that this result represents the maximum DQE that can be obtained from the conventional EPID at 6 MV.) Input-quantum-limited DQE performance is observed for the prototypes at a dose as low as 0.022 cGy, as indicated by the nearly overlapping DQE results at different doses. It is also observed that the choice of the top reflector does not significantly affect the DQE results. Note that the small dips in the measured DQE for the prototypes originate from the previously noted anomalies in the NNPS results.

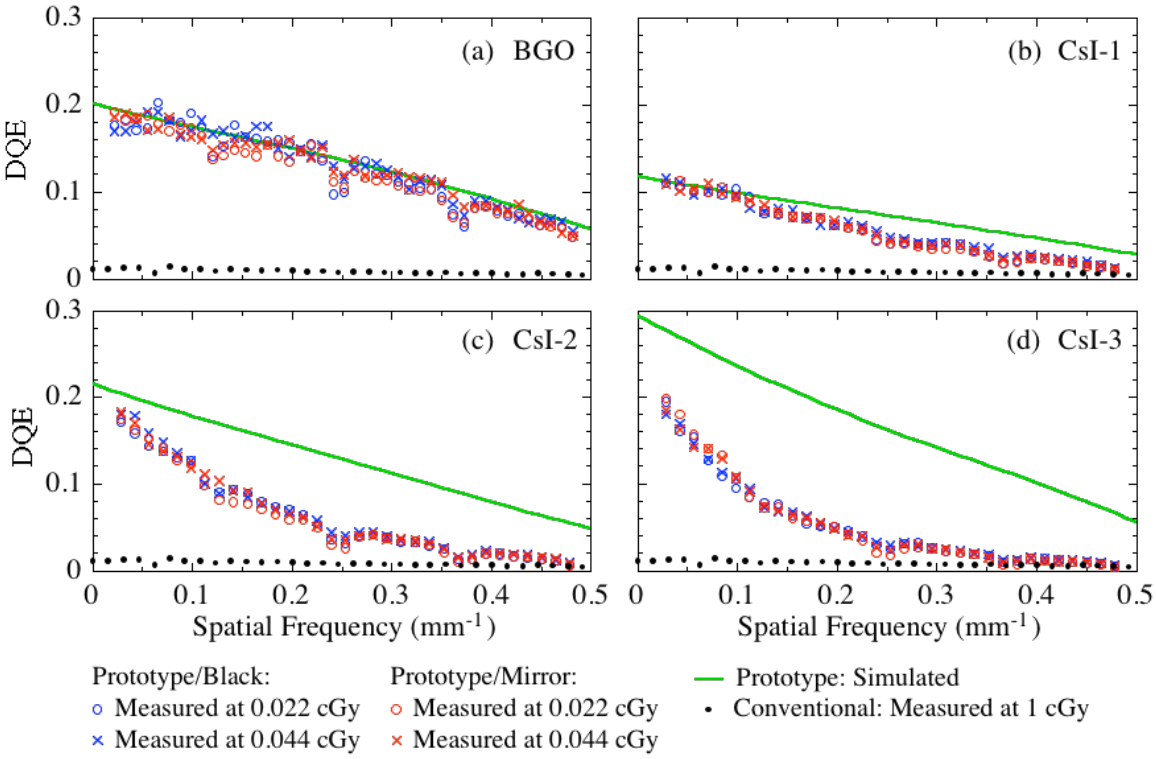

Figure 4.7. DQE for the (a) BGO, (b) CsI-1, (c) CsI-2 and (d) CsI-3 prototype EPIDs. Results are shown for configurations with the black top reflector (blue symbols) and the mirror top reflector (red symbols), at both 0.022 and 0.044 cGy. The green lines correspond to polynomial fits to the DQE results obtained through simulation. The black dots correspond to DQE results measured from the conventional EPID at 1 cGy (adapted from data appearing in Ref. 4).

As shown in Fig. 4.7(a), the measured DQE for the BGO prototype is very close to the simulated results for frequencies up to ~0.3 mm^{-1}, indicating a close-to-unity optical Swank factor. At higher frequencies, the measured DQE becomes slightly lower than the simulated results. At the Nyquist frequency, the measured DQE is ~80% of the simulated value. This is likely a consequence of the presence of some element-to-element optical crosstalk. The overall similarity of the measured and simulated DQE results suggests that the large differences between the corresponding MTF results shown in Fig. 4.5 are *primarily* due to misalignment and misregistration. Since these effects lead to deterministic noise propagation, which results in modulation of the NNPS by the square of the MTF,[12] their impact on DQE is muted, as can be anticipated through an examination of Eq. (4.2). Finally, compared with the conventional EPID, the BGO prototype provides ~20 times DQE improvement at zero frequency (i.e., ~20% compared to 1%), and ~10 times at the Nyquist frequency of 0.49 mm^{-1} (i.e., ~5% compared to 0.5%).

Figure 4.7(b) shows that the measured DQE results for the CsI-1 prototype approach the theoretical upper limit at low frequencies, indicating a close-to-unity optical Swank factor. However, at frequencies beyond ~0.1 mm^{-1}, the measured DQE is much lower than the simulated DQE due to degradation caused by lateral optical spreading. Nevertheless, the CsI-1 prototype exhibits greatly improved DQE compared to the conventional EPID at all frequencies – for example, ~12% versus ~1% at zero frequency and ~1.5% versus ~ 0.5% at the Nyquist frequency.

As shown in Figs. 4.7(c) and 4.7(d), further increases in CsI:Tl scintillator thickness leads to higher DQE at low spatial frequencies. Using polynomial extrapolation, the measured DQE for CsI-2 and CsI-3 at zero frequency is estimated to be up to ~20% and 25%, respectively. These values are lower than the corresponding simulated upper limits due to reduced optical Swank factor for thicker scintillators. In addition, the DQE results of these two prototypes show strong fall-off at higher frequencies, resulting in even larger differences from the corresponding upper limits. At the Nyquist frequency, the measured DQE for these two prototypes is not quite twice that for the conventional EPID. As a result of the more significant drop in DQE for the thicker CsI:Tl scintillators, CsI-1 exhibits higher DQE compared to CsI-2 and CsI-3 at frequencies above ~0.2 mm^{-1} and 0.1 mm^{-1}, respectively. Additionally, CsI-2 provides higher DQE than CsI-3 above ~0.03 mm^{-1}. These complicated behaviors are mainly due to the more pronounced lateral optical spreading in the thicker CsI:Tl scintillators.

E. PHANTOM IMAGES

Figure 4.8 shows x-ray images of the contrast detail phantom obtained using the prototype EPIDs configured with the mirror top reflector, as well as using the conventional EPID. As observed from Figs. 4.8(a), 4.8(c), 4.8(e), 4.8(g) and 4.8(i), at a dose of 0.022 cGy, all prototype EPIDs provide significantly improved contrast resolution compared to the conventional EPID. Moreover, even at this extremely low dose, the prototype EPIDs allow delineation of objects having contrast as low as ~0.2%. In addition, the contrast resolution offered by the BGO prototype at 0.044 cGy [Fig. 4.8(d)] is at least comparable to, and perhaps slightly better than, that provided by the

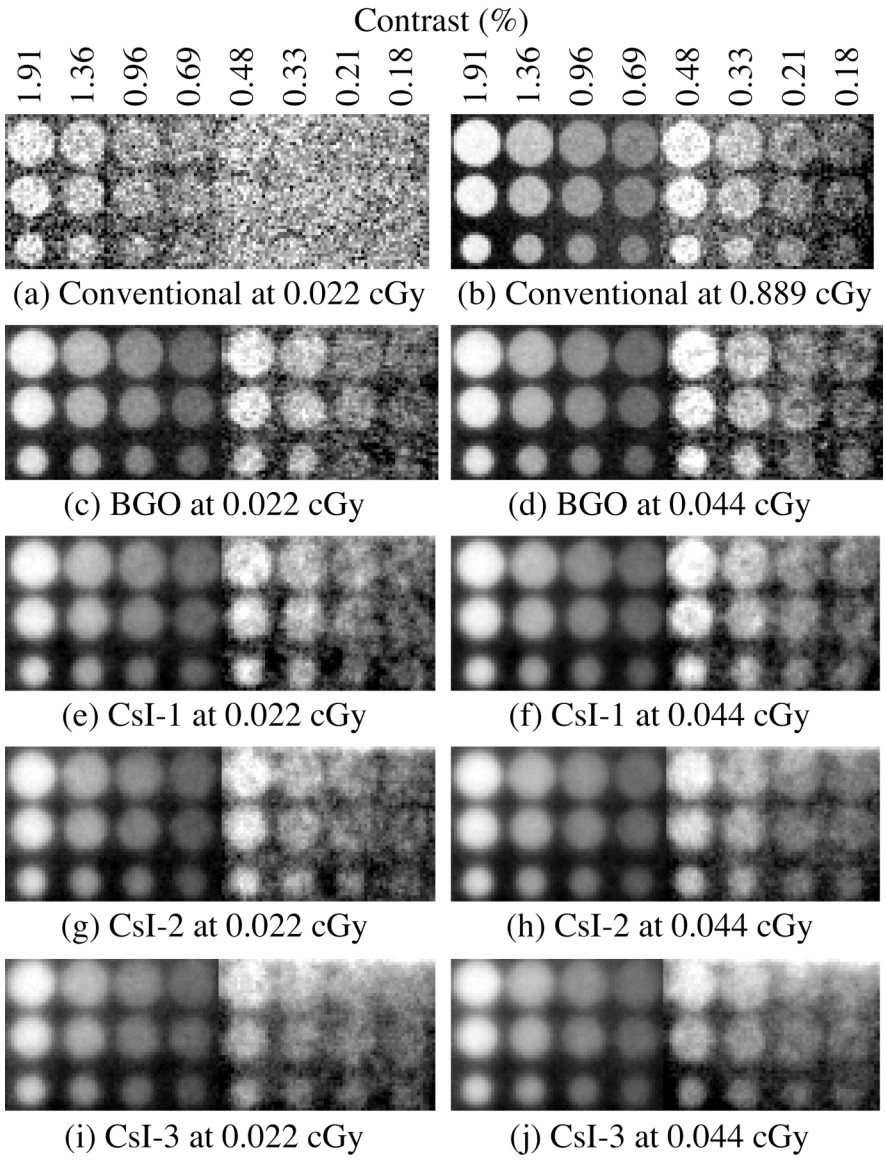

Figure 4.8. X-ray images of a contrast detail phantom. Images acquired using the conventional EPID at (a) 0.022 and (b) 0.889 cGy. Images acquired using the: (c) BGO, (e) CsI-1, (g) CsI-2 and (i) CsI-3 prototypes at 0.022 cGy; and the (d) BGO, (f) CsI-1, (h) CsI-2 and (j) CsI-3 prototypes at 0.044 cGy. All prototype EPIDs were configured with a mirror top reflector. Due to the limited size of the segmented scintillators, each prototype image is formed by stitching two separately acquired images (left and right) corresponding to adjacent parts of the phantom. In addition, in order to optimize object visibility, the two parts in each image were enhanced separately using different window and level. For consistency, the images acquired with the conventional EPID were also enhanced using the same method (but different values for the window and level). The legend above (a) and (b) indicates the estimated contrast of the holes at 6 MV.[37] The diameters of the three rows of holes are 13, 11 and 8 mm.

conventional EPID at 20 times more dose [Fig. 4.8(b)]. Although the spatial resolution provided by the BGO prototype is slightly inferior to that of the conventional EPID, the boundaries of the objects shown in Fig. 4.8(d) are still clearly distinguishable. It is also interesting to note that, despite its lower DQE, the CsI-1 prototype [Fig. 4.8(f)] provides object visibility similar to that offered by the BGO prototype [Fig. 4.8(d)]. However, the spatial resolution is noticeably inferior for the image obtained with CsI-1. For the thicker scintillators (CsI-2 and CsI-3), the objects in the corresponding images [Figs. 4.8(h) and 4.8(j)] are even more blurred. As a result, it becomes progressively more difficult to distinguish the boundaries of the low-contrast objects. For these non-optimized CsI:Tl prototypes, increasing scintillator thickness does not result in improvement in object visibility.

Figure 4.9 shows x-ray images of the human head phantom obtained using the BGO prototype configured with the mirror top reflector, as well as using the conventional EPID. A comparison of the images in Figs. 4.9(d) and 4.9(a) indicates that the BGO prototype provides significantly improved image quality compared to the conventional EPID at a dose of 0.044 cGy. Moreover, for the low-contrast features of the phantom, the BGO prototype images at doses of 0.022 and 0.044 cGy [Figs. 4.9(c) and 4.9(d)] demonstrate contrast-detail visibility similar to that obtained with the conventional EPID at 0.444 cGy [Fig. 4.9(b)], but at somewhat reduced spatial resolution.

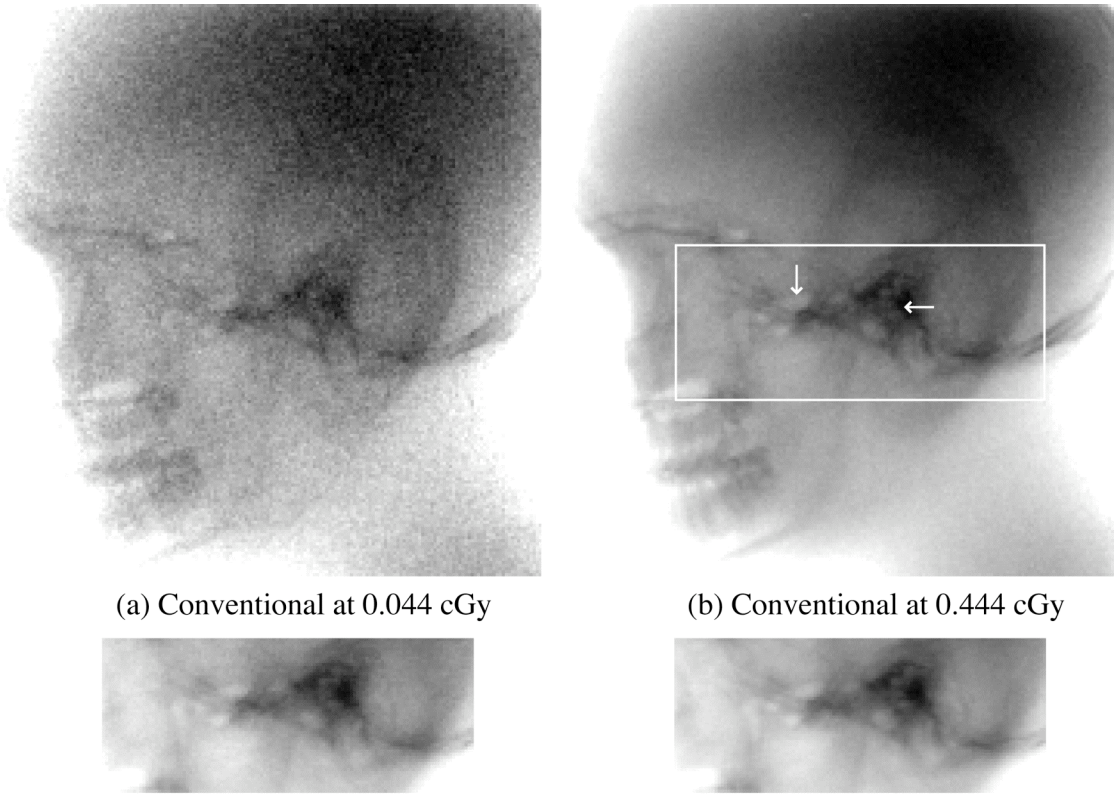

(a) Conventional at 0.044 cGy (b) Conventional at 0.444 cGy

(c) BGO at 0.022 cGy (d) BGO at 0.044 cGy

Figure 4.9. X-ray images of a human head phantom acquired using the conventional EPID at (a) 0.044 and (b) 0.444 cGy, and the BGO prototype (with the mirror top reflector) at (c) 0.022 and (d) 0.044 cGy. The white rectangle superimposed in (b) corresponds to the region imaged by the BGO prototype, while the two white arrows point to a pair of low-contrast features.

IV. DISCUSSION

The development of high-DQE EPIDs employing thick, segmented scintillators is motivated by the desire to obtain soft-tissue visualization in the treatment room. This chapter presents an empirical investigation of four prototype EPIDs employing such scintillators – a BGO scintillator (11.3 mm thick) and three CsI:Tl scintillators (11.4, 25.6 and 40.0 mm thick). The portal imaging performance of these prototypes was compared to corresponding theoretical upper limits obtained through Monte Carlo simulation, as well as to values measured from a conventional EPID.

Compared to the conventional EPID, the BGO prototype exhibits somewhat lower MTF but significantly increased DQE at all spatial frequencies, as well as the ability to delineate low-contrast objects at a dose of only 0.022 cGy (corresponding to a single LINAC beam pulse). Moreover, given the relatively modest thickness of the BGO scintillator, the performance of a large-area version of such a scintillator would not be expected to be limited by radiation incident at oblique angles[13] – removing the need for a focused geometry for the scintillator elements.[11] The three CsI:Tl prototypes also showed significantly improved low-frequency DQE and image quality at 0.022 cGy. However, the MTF and DQE of these prototypes are considerably lower than theoretical expectations at higher spatial frequencies, mainly due to the effect of lateral optical spreading. Consequently, the increasing thickness of these non-optimized CsI:Tl scintillators did not provide the progressive improvement in DQE expected at high frequencies. In order to circumvent this limitation, lateral optical spreading in such scintillators needs to be reduced through modifications of the septal walls (e.g., through use of more opaque polymer reflectors or replacing polymer reflectors with metal reflectors).[1, 11] In addition, further improvement in the alignment between scintillator elements would facilitate more accurate registration between the segmented scintillator and the underlying flat-panel array, thus improving spatial resolution.

While the BGO prototype demonstrated, by far, the best imaging performance, it also showed dose-dependent sensitivity. The sharp decline in scintillator sensitivity (~17%) within the first few hundred cGy of radiation exhibited by the prototype would

complicate clinical use of such a scintillator. Previous examinations of the effect of radiation on the performance of BGO have indicated widely varying results – ranging from negligible to significant effects[14-24] – possibly due to differences in crystal quality and irradiation conditions. Some studies suggested the possibility that high-energy X rays knock out electrons from oxygen atoms, forming color centers that increase optical absorption in the BGO crystal.[14, 16, 18] A possible way to reduce such undesirable radiation effects involves the introduction of Eu^{3+} as a doping agent, which can donate electrons to the oxygen atoms to prevent the formation of color centers.[14, 18]

REFERENCES

[1] Y. Wang, L. E. Antonuk, Y. El-Mohri and Q. Zhao, "A Monte Carlo investigation of Swank noise for thick, segmented, crystalline scintillators for radiotherapy imaging," Medical Physics, accepted for publication (2009).

[2] A. Sawant, L. E. Antonuk, Y. El-Mohri, Q. Zhao, Y. Wang, Y. Li, H. Du and L. Perna, "Segmented crystalline scintillators: empirical and theoretical investigation of a high quantum efficiency EPID based on an initial engineering prototype CsI(Tl) detector," Medical Physics **33**, 1053-1066 (2006).

[3] Y. Wang, Q. Zhao, L. E. Antonuk, Y. El-Mohri and L. Perna, "High-DQE EPIDs based on thick, segmented BGO and CsI:Tl scintillators: Performance evaluation at extremely low dose," Medical Physics, under review (2009).

[4] Y. El-Mohri, K.-W. Jee, L. E. Antonuk, M. Maolinbay and Q. Zhao, "Determination of the Detective Quantum Efficiency of a Prototype, Megavoltage Indirect Detection, Active Matrix Flat-Panel Imager," Medical Physics **28**, 2538-2550 (2001).

[5] Data sheet for Cesium Iodide scintillation materials, Saint-Gobain Crystals, OH, U.S.

[6] A. Sawant, L. E. Antonuk, Y. El-Mohri, Y. Li, Z. Su, Y. Wang, J. Yamamoto, Q. Zhao, H. Du, J. Daniel and R. A. Street, "Segmented phosphors – MEMS-based high quantum efficiency detectors for megavoltage x-ray imaging," Medical Physics **32**, 553-565 (2005).

[7] L. E. Antonuk, Y. El-Mohri, J. H. Siewerdsen, J. Yorkston, W. Huang, V. E. Scarpine and R. A. Street, "Empirical investigation of the signal performance of a high-resolution, indirect detection, active matrix flat-panel imager (AMFPI) for fluoroscopic and radiographic operation," Medical Physics **24**, 51-70 (1997).

[8] A. Sawant, L. E. Antonuk and Y. El-Mohri, "Slit design for efficient and accurate MTF measurement at megavoltage x-ray energies," Medical Physics **34**, 1535-1545 (2007).

[9] I. Kawrakow and D. W. O. Rogers, "The EGSnrc Code System: Monte Carlo Simulation of Electron and Photon Transport," Ottawa, Canada (2000).

[10] J. A. Treurniet, B. R. B. Walters and D. W. O. Rogers, "BEAMnrc, DOSXYZnrc and BEAMDP GUI User's Manual," Ottawa, Canada (2001).

[11] A. Sawant, L. E. Antonuk, Y. El-Mohri, Q. Zhao, Y. Li, Z. Su, Y. Wang, J. Yamamoto, H. Du, I. Cunningham, M. Klugerman and K. Shah, "Segmented crystalline scintillators: an initial investigation of high quantum efficiency detectors for megavoltage x-ray imaging," Medical Physics **32**, 3067-3083 (2005).

[12] I. A. Cunningham, "Applied linear-system theory," in *Handbook of medical imaging*, *Vol. 1,* edited by J. Beutel, H. L. Kundel and R. L. van Metter (SPIE, Bellingham, WA, 2000), pp. 79-160.

[13] T. T. Monajemi, B. G. Fallone and S. Rathee, "Thick, segmented CdWO4-photodiode detector for cone beam megavoltage CT: a Monte Carlo study of system design parameters," Medical Physics **33**, 4567-4577 (2006).

[14] Z. Y. Wei, R. Y. Zhu, H. Newman and Z. W. Yin, "Radiation resistance and fluorescence of europium doped BGO crystals," Nuclear Instruments and Methods in Physics Research Section A **297**, 163-163 (1990).

[15] R. Y. Zhu, H. Stone, H. Newman, T. Q. Zhou, H. R. Tan and C. F. He, "A study on radiation damage in doped BGO crystals," Nuclear Instruments and Methods in Physics Research Section A **302**, 69-75 (1991).

[16] R. Y. Zhu, D. A. Ma and H. Newman, "Scintillating crystals in a radiation environment," Nuclear Physics B **44**, 547-556 (1995).

[17] R. Y. Zhu, "Radiation damage in scintillating crystals," Nuclear Instruments and Methods in Physics Research Section A **413**, 297-311 (1998).

[18] J. H. Kim, N. E. Yu and B. M. Jin, "Eu doping effect on the radation resistance in Bi4Ge3O12 (BGO) scintillator," Journal of the Korean Physical Society **32**, S1123-S1126 (1998).

[19] R. Georgii, R. Meifll, W. Hajdas, H. Henschel, H. D. Graf, G. G. Lichti, P. v. Neumann-Cosel, A. Richter and V. Schˆnfelder, "Influence of radiation damage on BGO scintillation properties," Nuclear Instruments and Methods in Physics Research Section A **413**, 50-58 (1998).

[20] V. A. Gusev, I. N. Kupriyanov, V. D. Antsygin, Y. V. Vasiliev, V. N. Shlegel, G. N. Kuznetsov, N. V. Ivannikova, A. I. Korchagin, A. V. Lavrukhin, S. E. Petrov and S. N. Fadeev, "Features of radiation damage of BGO crystals grown by the low-thermal-gradient Czochralski technique," Nuclear Instruments and Methods in Physics Research Section A **460**, 457-464 (2001).

[21] P. Kozma and P. Kozma, "Radiation resistivity of BGO crystals due to low-energy gamma-rays," Nuclear Instruments and Methods in Physics Research Section A **501**, 499-504 (2003).

[22] P. Lecoq, P. J. Li and B. Rostaing, "BGO radiation damage effects: optical absorption, thermoluminescence and thermoconductivity," Nuclear Instruments and Methods in Physics Research Section A **300**, 240-258 (1991).

[23] K. C. Peng, R. S. Lu, K. Ueno, C. H. Wang, M. Z. Wang, F. I. Chou, Y. Y. Wei and W. S. Hou, "Low-dose radiation damage and recovery of undoped BGO crystals," Nuclear Instruments and Methods in Physics Research Section A **452**, 252-255 (2000).

[24] S. K. Sahu, K. C. Peng, H. C. Huang, C. H. Wang, Y. H. Chang, W. S. Hou, K. Ueno, F. I. Chou and Y. Y. Wei, "Radiation hardness of undoped BGO crystals," Nuclear Instruments and Methods in Physics Research **A388**, 144-148 (1997).

CHAPTER 5

SEGMENTED SCINTILLATORS: A MONTE CARLO INVESTIGATION FOR MV CBCT

I. INTRODUCTION

The theoretical and empirical investigations reported in the previous two chapters have shown that EPIDs employing thick, segmented BGO and CsI:Tl scintillators can offer significantly improved DQE performance compared to conventional EPIDs. Encouraged by these portal imaging results, it is interesting to investigate the performance of these high-efficiency scintillators for MV CBCT imaging. A Monte Carlo method was used to theoretically examine the contrast-to-noise performance provided by hypothetical MV CBCT systems incorporating 10 and 40 mm thick, segmented BGO and CsI:Tl detectors employing polymer and tungsten septal walls. The results are compared to simulation results for a MV CBCT system employing a phosphor screen detector, representing that used in conventional EPIDs. Finally, prospects for the realization of optimized scintillator designs for low dose MV CBCT are discussed. Note that the figures and table shown in this chapter were obtained from an article that the author of this dissertation published in the *International Journal of Medical Physics Research and Practice*.[1]

II. METHODS

A. OVERVIEW

In order to quantify the performance of MV CBCT systems employing a variety of hypothetical segmented scintillator designs, Monte Carlo simulations were carried out using the EGSnrc and DOSXYZnrc codes,[2, 3] which simulate radiation energy deposition in the segmented scintillators. While optical transport simulation is of interest, it was beyond the scope of this initial study.

In the simulations, the parameters of PCUT and ECUT (corresponding to cutoff energies for photons and electrons) were chosen to be 0.01 and 0.521 MeV (both corresponding to a kinetic energy of 0.01 MeV), respectively. The EXACT boundary crossing algorithm, PRESTA-II electron-step algorithm, and NIST bremsstrahlung cross sections were used. The simulations were performed using a total of 264 CPUs on two 64-bit Linux clusters with 1.8 and 2.2 GHz AMD Opteron processors, respectively, as well as a 64-bit Apple cluster with 2.0 GHz G5 processors. This study consumed a total of ~700,000 CPU hours.

B. SIMULATION SET-UP

Figure 5.1 schematically illustrates the simulated MV CBCT system based on segmented scintillating detectors. The x-ray source employed a 6 MV photon beam representing a typical spectral output along the central axis of a Varian LINAC.[4] Any changes in the spectral output across the radiation field caused by the shape of the LINAC's flattening filter were not considered in the simulations. Given the small size of

the field used in the study, these changes are minimal[5] and are not expected to significantly affect the simulation results. The source and detector tomographically scan a cylindrical CT contrast phantom over 360 degrees, at 2-degree intervals, resulting in a total of 180 projection images.

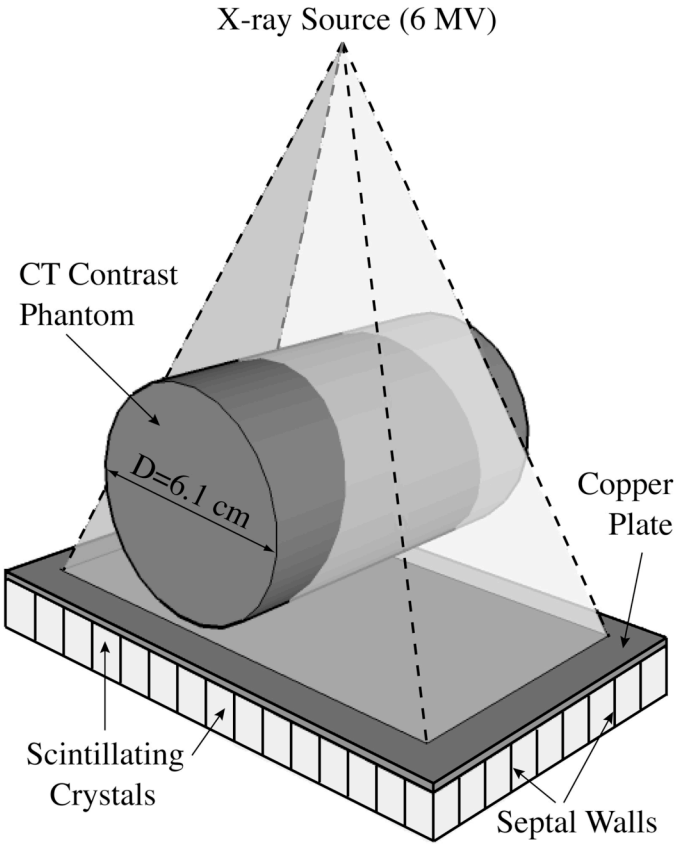

Figure 5.1. Three-dimensional schematic view of the simulated MV CBCT system employing a segmented scintillating detector.

The segmented detector consisted of a matrix of 180 × 81 scintillator elements and a 1 mm thick copper plate coupled to the x-ray side of the scintillator. In this study, a total of 12 scintillator designs, with 10 and 40 mm thick, segmented CsI:Tl and BGO scintillators, separated with low-density (polystyrene), equivalent-density (scintillator

material) and high-density (tungsten) septal walls, were studied. The scintillator element-to-element pitch was chosen to be 0.508 mm, which is equal to the pixel pitch of an indirect-detection MV AMFPI array[6] that is used in empirical evaluation of recent prototype detectors.[7] The width of the septal walls was 0.05 mm. In the simulations, the energy deposited in the septal walls was not considered to contribute to the imaging signal, even in the cases where the septal walls were assumed to be the same material as the scintillator. The use of the three septal wall types allowed examination of detector performance when the scintillator and the septal walls have greatly different, or similar, radiation attenuation properties.

The center of the CT contrast phantom and the entrance surface of the segmented detector (i.e., top surface of the Cu plate) were 126 and 130 cm from the source, respectively. The detector had an area of 9.14 × 4.12 cm^2. The beam size at the entrance of the detector was 8.46 × 3.17 cm^2, which covered the whole CT contrast phantom in the radial direction. Ideally, the scintillator elements should be focused towards the x-ray source,[8] so as to reduce the loss of spatial resolution induced by the X rays incident at oblique angles. For the present study however, due to the large source-to-detector distance and the limited detector size, the maximum incident angle of the X rays is only ~2°. Therefore, the simulated system does not suffer greatly from the effect of oblique incidence of radiation and thus, for simplicity, a non-focused geometry was used.

For comparison, simulations were also performed for a CBCT system using a conventional EPID incorporating a phosphor screen detector, which consists of a Lanex

Fast B screen (Eastman Kodak, Rochester, NY) and an overlying 1 mm thick copper plate.[9] In particular, the phosphor screen was simulated as a 362 μm thick layer of Gd_2O_2S:Tb with a mass density of 3.67 g/cm^3 and having the same area as the segmented scintillators.

Figure 5.2 illustrates the two types of CT contrast phantoms simulated in the present study. The phantoms consist of tissue-equivalent object(s) embedded in a large "background" water cylinder. The diameters of the object cylinders and the large water cylinder were 2.03 and 6.10 cm, respectively. The center of each object cylinder was positioned 1.52 cm from the center of the water cylinder. The length of all phantoms was 4.06 cm. Figure 5.2(a) illustrates the geometry for a series of phantoms, each with a single tissue-equivalent object. These phantoms were scanned with a 40 mm thick, segmented CsI:Tl detector with low-density septal walls. The properties of the tissue-equivalent materials appear in Table 5.1.[10, 11] The phantom illustrated in Fig. 5.2(b) consists of three selected tissue-equivalent objects, i.e., liver, brain and breast. This phantom, rather than the one-object phantom, was scanned by all 12 segmented detectors, as well as the phosphor screen detector. It was used to considerably reduce the total amount of computational time required for these parts of the study. Note that, in this study, due to a limitation on the maximum number of array elements allowed by the simulation codes, it was not feasible to use segmented detectors with an element pitch of 0.508 mm to perform CBCT scans of phantoms of human dimensions (e.g., 20 to 30 cm).

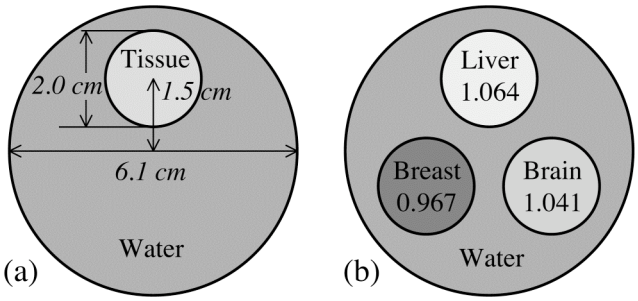

Figure 5.2. Cross-sectional view of cylindrical CT contrast phantoms with (a) one and (b) three tissue-equivalent objects embedded in water background. The geometric properties indicated in (a) also apply to (b). In (b), the electron density relative to water is shown for the three objects.

Table 5.1. Chemical composition, mass density and relative electron density of the tissue-equivalent materials used in this study.[10, 11]

Tissue-equivalent Material	Element Weight (%)										Mass Density (g/cm^3)	Relative Electron Density
	H	C	N	O	Na	P	S	Cl	K	Ca		
Breast (BR12)[10]	8.68	69.95	2.37	17.91				0.14		0.95	0.990	0.967
Lipoma[11]	10.9	71.9	3.0	13.8	0.1		0.2	0.1			0.980	0.977
Mammary Gland (Adult #1)[11]	10.9	50.6	2.3	35.8	0.1	0.1	0.1	0.1			0.990	0.987
Skin (Fetus)[11]	10.8	5.1	1.2	82.1	0.2	0.1	0.1	0.3	0.1		1.020	1.016
Brain (SR2)[10]	10.83	72.54	1.69	14.86				0.08			1.045	1.041
Liver (mix)[10]	8.09	67.00	2.47	19.99				0.14		2.31	1.095	1.064

C. MONTE CARLO SIMULATIONS

1. Correspondence of x-ray fluence to dose

In the CBCT simulations, the amount of radiation used was quantified in terms of the x-ray fluence (i.e., the number of X rays per unit area) incident on the top surface of the x-ray detector. In order to allow comparison of the irradiation conditions used in the simulations to those reported in other publications concerning MV CBCT, the equivalence between the x-ray fluence and the irradiation time, in monitor units (MU), for a therapy machine was established through a calibration simulation of the absorbed dose (in cGy) at a depth of 10 cm, in a 30 × 30 × 30 cm^3 water phantom. The surface of

the water phantom was positioned 100 cm from the x-ray source, and the field size at the surface was 10×10 cm^2. Under such calibration conditions and for an irradiation time of 1 MU, a medical LINAC is typically calibrated so as to deposit a dose of ~0.8 to 1 cGy at 6 MV. Therefore, the reported doses correspond to the irradiation time (in MU) for therapy machines so calibrated, and thus represent equivalent calibration doses. For simplicity, such equivalent calibration doses will be referred to as doses. The calibration simulation was performed using 20×10^9 X rays crossing a 10×10 cm^2 field at 100 cm and yielded a dose of ~0.09 cGy. The statistical uncertainty of this simulation is ~0.6%. The x-ray fluence used in this calibration simulation corresponds to a value for 3.17×10^9 X rays over the 8.46×3.17 cm^2 field at 130 cm (i.e., the distance between the x-ray source and the entrance surface of the x-ray detector). Thereafter, for a given CBCT simulation using N X rays, the corresponding dose is given by:

$$Dose = \frac{N}{3.17 \times 10^9} \times 0.09 \text{ (cGy)}. \tag{5.1}$$

For example, for the simulations involving the segmented detectors, when 0.6×10^9 X rays were used for each of 180 projection images, the total scan dose is 3.08 cGy. For the simulations involving the phosphor screen detector, 19.8×10^9 X rays were used per projection, resulting in a total scan dose of 101.64 cGy.

2. Removal of cupping artifact

The reconstructed CBCT images exhibited a cupping artifact, which was manifested as a general increase in signal along the radial direction from the center to the edge of the cylindrical CT phantom. This artifact arises from radiation scattering,[12-14] and can be

removed through subtracting correction factors obtained from the averaged radial signal in the reconstructed image of a uniform water phantom having the same dimensions as the contrast phantom and obtained using the same simulation set-up.[15] However, this standard method was impractical to implement for all scintillator designs examined in this study, since each design required its own correction, which consumes as much computational time as scanning the contrast phantom (i.e., an additional ~500,000 CPU hours which was beyond the available resources). In order to overcome this limitation, a simplified method was developed to determine the correction factors. Rather than simulating an additional water phantom, the simplified method utilizes the water region in the reconstructed image of the contrast phantom itself to determine the correction factors. For purpose of validation, both methods were examined and compared for the case of a 40 mm thick, segmented CsI:Tl detector with low-density septal walls.

3. Performance evaluation

a. Slice thickness and total scan dose

Using the phantom shown in Fig. 5.2(b) and a 40 mm thick, segmented CsI:Tl detector with low-density septal walls, CBCT simulations were performed at a total scan dose of 1.54, 3.08, 4.62 and 6.16 cGy. The contrast-to-noise performance of the three tissues (liver, brain and breast) was studied as a function of slice thickness for a scan dose of 3.08 cGy, and as a function of dose for a reconstructed slice thickness of 5.08 mm.

b. Tissue-equivalent objects

Using phantoms like that shown in Fig. 5.2(a) and the same CsI:Tl detector as that used in the previous sub-section, CBCT simulations were performed at 1.54 and 3.08 cGy. The contrast, noise and contrast-to-noise performance was examined as a function of the relative electron density, RED, of the tissue-equivalent materials (relative to water).

c. Segmented scintillator designs

The phantom shown in Fig. 5.2(b) was scanned with all 12 segmented scintillator designs at 1.54 and 3.08 cGy. The contrast, noise and contrast-to-noise performance of the three tissues obtained from the various detectors were compared. In addition, the contrast-to-noise performance was also studied as a function of the zero-spatial frequency DQE_{RAD} of the various detectors.

d. Segmented detectors versus phosphor screen detector

The phantom shown in Fig. 5.2(b) was also scanned with the phosphor screen detector at doses up to ~102 cGy. The contrast-to-noise performance of the three tissues obtained using the phosphor screen detector was compared to that obtained using the various segmented detectors at 1.54 cGy.

D. Analysis methods

A Feldkamp-based algorithm [16] with a ramp filter was used to reconstruct the spatial distribution of attenuation coefficients for the CT phantoms from the projection images

obtained at different angles. This algorithm calculates attenuation line integrals (l) along straight pathways from the source to the imager pixels at a given projection angle using the exponential attenuation formula,

$$e^{-l} = \frac{In_1}{In_0} \tag{5.2}$$

$$l = \ln \frac{In_0}{In_1},$$

where In_1 and In_0 are x-ray induced signals obtained from projection images with and without (i.e., flood-field image) the phantom, respectively. In order to reduce the statistical uncertainty associated with In_0, the average of 30 flood-field images, each obtained with the same dose as that used for a projection phantom image, was used to determine the value of In_0. The voxel pitch and the thickness of a single slice of the reconstructed image were both chosen to be 0.508 mm, matching the element pitch of the segmented detectors. From the reconstructed image, a number of single slices were averaged to obtain a thicker slice (e.g., 5.08 mm for 10 single slices) with better statistics.

From the reconstructed images, the mean signals (attenuation coefficients) in the water background (μ_{water}) and in the object (μ_{obj}) were extracted to evaluate performance. The selection of the regions from which data were extracted excluded the edges of the objects and the phantom, as well as the center of the phantom where the cupping artifact correction induced non-negligible statistical uncertainties. [See Eq. (D.5) in Appendix D] These signals were converted to MV CT numbers, CTN, assuming a value of 0 Hounsfield Units (HU) in water and –1000 HU in air (or vacuum). The CTN of an object, CTN_{obj}, can be expressed as:

$$CTN_{obj} = \frac{\mu_{obj} - \mu_{water}}{\mu_{water}} \times 1000 \text{ (HU)}. \tag{5.3}$$

In this study, the contrast of an object, Contrast, is defined as:

$$Contrast = \left| CTN_{obj} - CTN_{water} \right| \tag{5.4}$$

$$= \frac{\left| \mu_{obj} - \mu_{water} \right|}{\mu_{water}} \times 1000 \text{ (HU)}.$$

The noise of an object, Noise, can be expressed as:

$$Noise = \frac{\sigma_{obj}}{\mu_{water}} \times 1000, \tag{5.5}$$

where σ_{obj} is the standard deviation of the voxel signal in the object. Therefore, the contrast-to-noise ratio, CNR, of the object can be expressed as:

$$CNR = \frac{Contrast}{Noise} = \frac{\left| \mu_{obj} - \mu_{water} \right|}{\sigma_{obj}}. \tag{5.6}$$

The analysis of statistical uncertainties in Contrast, Noise and CNR, using a previously described method for CT imaging,[17] appears in Appendix D.

III. RESULTS

A. CUPPING ARTIFACT REMOVAL

Figure 5.3 shows reconstructed images of a CT contrast phantom, embedded with three tissue equivalent objects, before and after the removal of cupping artifact using the standard method. The reconstructed image and the correction factors were both obtained using a 40 mm thick, segmented CsI:Tl detector with low-density septal walls. The results indicate that cupping artifact is effectively removed through the use of the standard method.

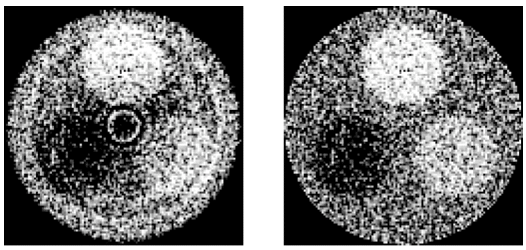

(a) (b)

Figure 5.3. Reconstructed images of the three-object phantom (a) before and (b) after the application of standard correction for the cupping artifact. The same window and level were used for both images.

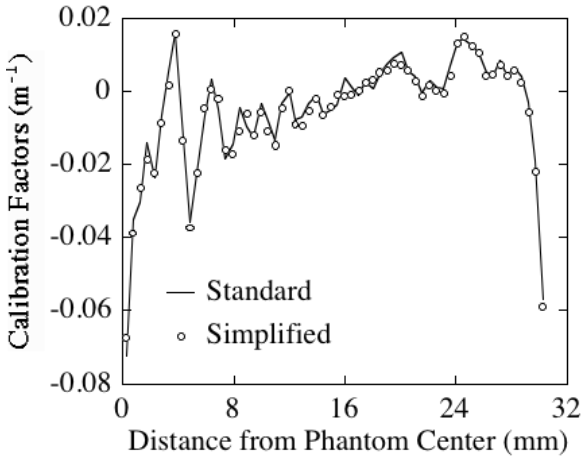

Figure 5.4. Comparison of cupping artifact correction factors obtained with the standard and the simplified method. The factors are plotted as a function of the radial distance from the center of the phantom.

In order to validate the use of the simplified method for cupping artifact removal, the correction factors obtained using the standard and simplified methods were compared in Fig. 5.4. The factors obtained using two methods are seen to be very similar, indicating that the simplified method is as effective as the standard method. In addition, the CNR results determined from reconstructed images corrected with both methods differed by only ~2% – a value that is much lower than the statistical uncertainty of ~7% for the

CNR results. Therefore, in the remainder of the Results section, unless otherwise stated, the simplified method is used for the removal of cupping artifact.

B. PERFORMANCE EVALUATION

1. Slice thickness and total scan dose

The 40 mm thick, segmented CsI:Tl detector with low-density septal walls and the three-object phantom were selected for the examination of CNR^2 performance as a function of reconstructed slice thickness and total scan dose. In Fig. 5.5(a), CNR^2 for the three tissues are plotted as a function of slice thickness at a total scan dose of 3.08 cGy. CNR^2 is observed to increase approximately linearly with increasing slice thickness. In Fig. 5.5(b), CNR^2 is shown as a function of total scan dose for a reconstructed slice thickness of 5.08 mm (obtained by averaging 10 consecutive, individual slices). These CNR^2 results also exhibit an approximately linear increase with increasing dose. The linear behaviors observed in Figs. 5.5(a) and 5.5(b) are the result of increased number of quanta sampled – an effect that linearly reduces $Noise^2$. In the remainder of the Results section, performance metrics will be studied for a reconstructed slice thickness of 5.08 mm. For the segmented detectors, the performance will be examined at 1.54 and 3.08 cGy.

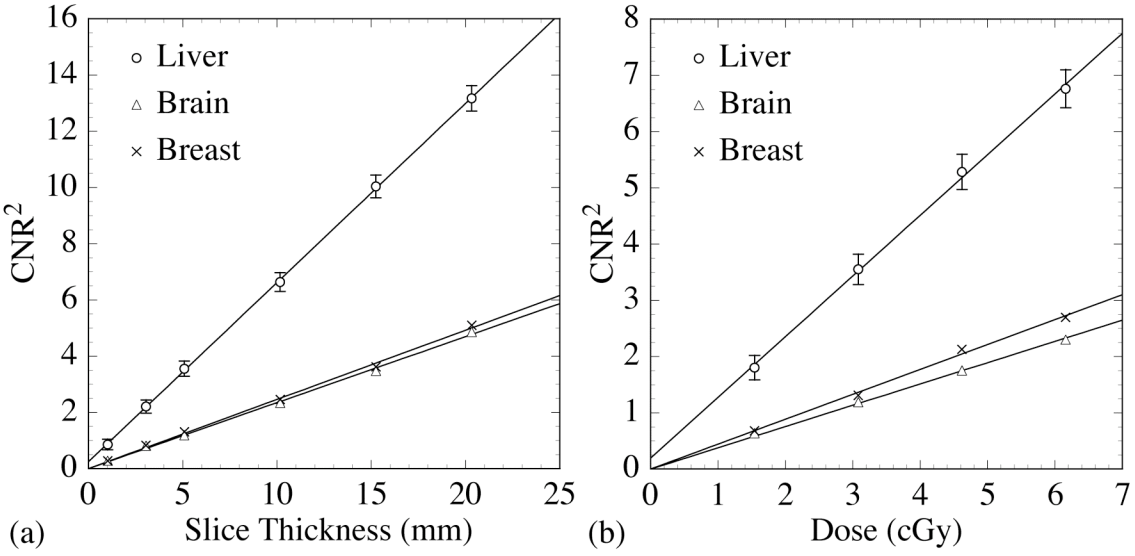

Figure 5.5. Results for CNR^2 as a function of (a) reconstructed slice thickness and (b) total scan dose. The solid lines indicate linear fits to the data. For reason of clarity, error bars are only shown for the liver-equivalent object. For a given slice thickness or dose, the errors in CNR^2 for the other two objects are approximately the same as that for the liver-equivalent object. Note that in this figure and in the remaining figures, the label "dose" refers to the equivalent calibration dose as defined in Sec. II. C. 1.

2. Tissue-equivalent objects

The 40 mm thick, segmented CsI:Tl detector with low-density septal walls was used to scan a uniform water phantom, as well as six one-object phantoms each employing a different tissue equivalent material. In the reconstructed images, the effect of the cupping artifact was removed using the standard method. In Fig. 5.6, simulation results for Contrast at 3.08 cGy, Noise at 1.54 and 3.08 cGy, as well as CNR at both doses, are plotted as a function of the relative electron density, RED, of the various tissue-equivalent objects. Note that the Contrast results at 1.54 cGy (not plotted) are almost the same as those at 3.08 cGy. As observed from Fig. 5.6(a), the results for Contrast increase approximately linearly as the RED difference between the object and background increases. Such linear behavior is the result of the dominance of Compton scattering at megavoltage energies. The slight deviations from linear behavior are probably due to the

presence of lower-probability interactions in the form of pair production, the cross-section of which is not proportional to electron density. As shown in Fig. 5.6(a), within the range of statistical uncertainty, the Noise of the various objects is almost constant at a given dose. Also, with doubled dose, the level of Noise drops by ~28%. As illustrated in Fig. 5.6(b), the CNR results behave in a pattern similar to that observed for the Contrast results. The improved CNR at the higher dose is due to a reduced level of Noise.

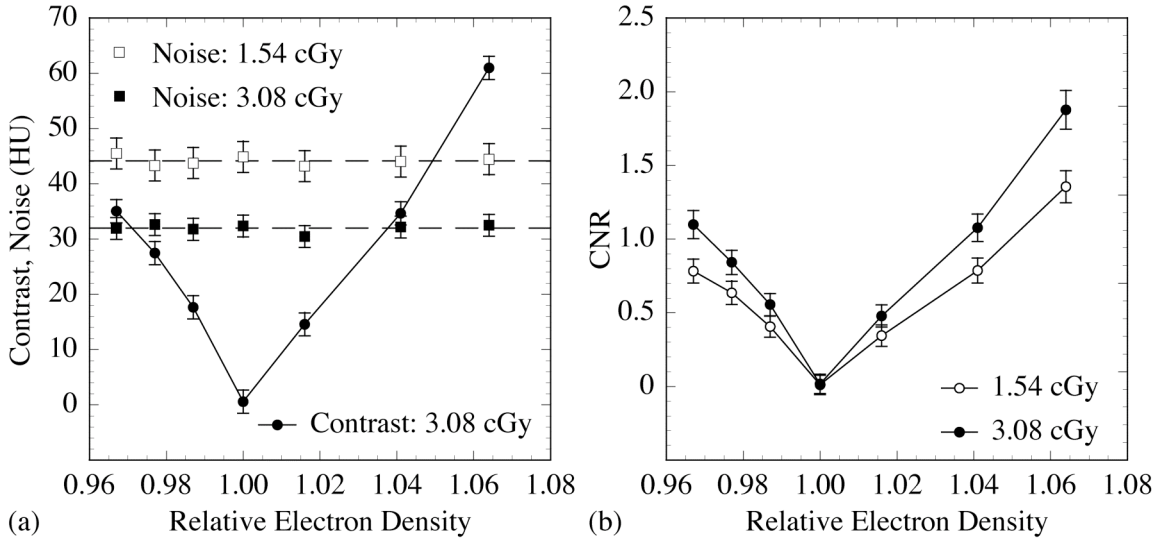

Figure 5.6. Results plotted as a function of the relative electron density of the tissue-equivalent objects. (a) Contrast at 3.08 cGy, as well as Noise at 1.54 and 3.08 cGy. The solid line joining the Contrast data points is drawn to guide the eye, whereas the dashed lines indicate the mean levels of the Noise results at two doses. (b) CNR at 1.54 and 3.08 cGy. The solid lines joining the CNR data points are drawn to guide the eye.

Fig. 5.7 shows the reconstructed images from which the results shown in Fig. 5.6 are determined. As seen in the figure, at 1.54 and 3.08 cGy, it is possible to delineate RED difference as low as 2.3% [Fig. 5.7(b)] and 1.3% [Fig. 5.7(i)], respectively. Moreover, the visibility of the objects improves with dose and with the RED difference between object and background, in line with the CNR results shown in Fig. 5.6(b).

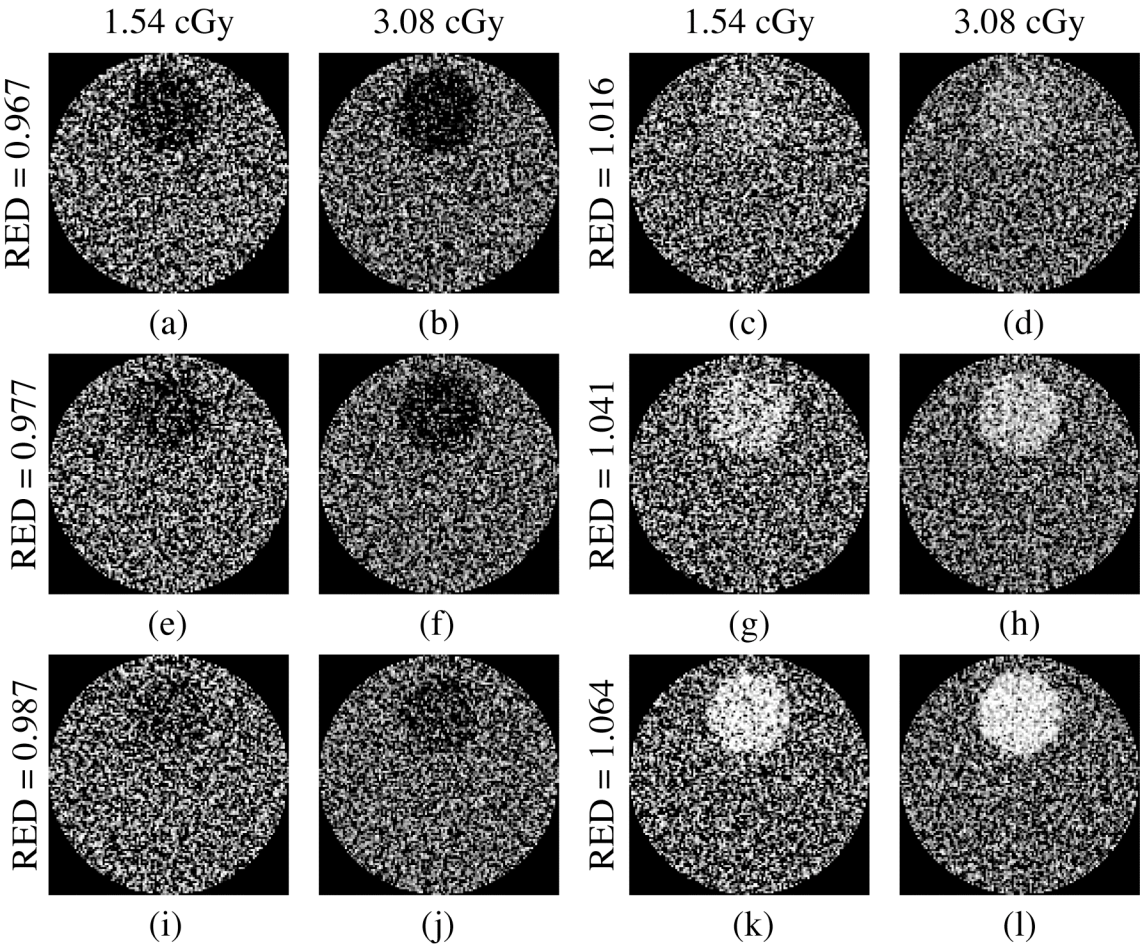

Figure 5.7. Reconstructed images of the CT contrast phantoms [as illustrated in Fig. 5.2(a)] embedded with various tissue-equivalent objects. For each phantom, images obtained at 1.54 cGy and 3.08 cGy are shown. The relative electron densities (RED) of the objects are indicated for each image phantom. The same window and level were selected for the images obtained at the same dose, whereas different window and level were selected for different doses to maximize object visibility.

3. Segmented scintillator designs

The three-object phantom was scanned by a total of 12 segmented scintillating detectors (i.e., 10 and 40 mm thick CsI:Tl and BGO detectors with low-, equivalent-, and high-density septal walls). In Fig. 5.8, Contrast, Noise and CNR results for the three tissue-equivalent objects are shown for the various detectors. As seen in Figs. 5.8(a), 5.8(b) and 5.8(c), the level of Contrast is higher for the liver-equivalent material, and

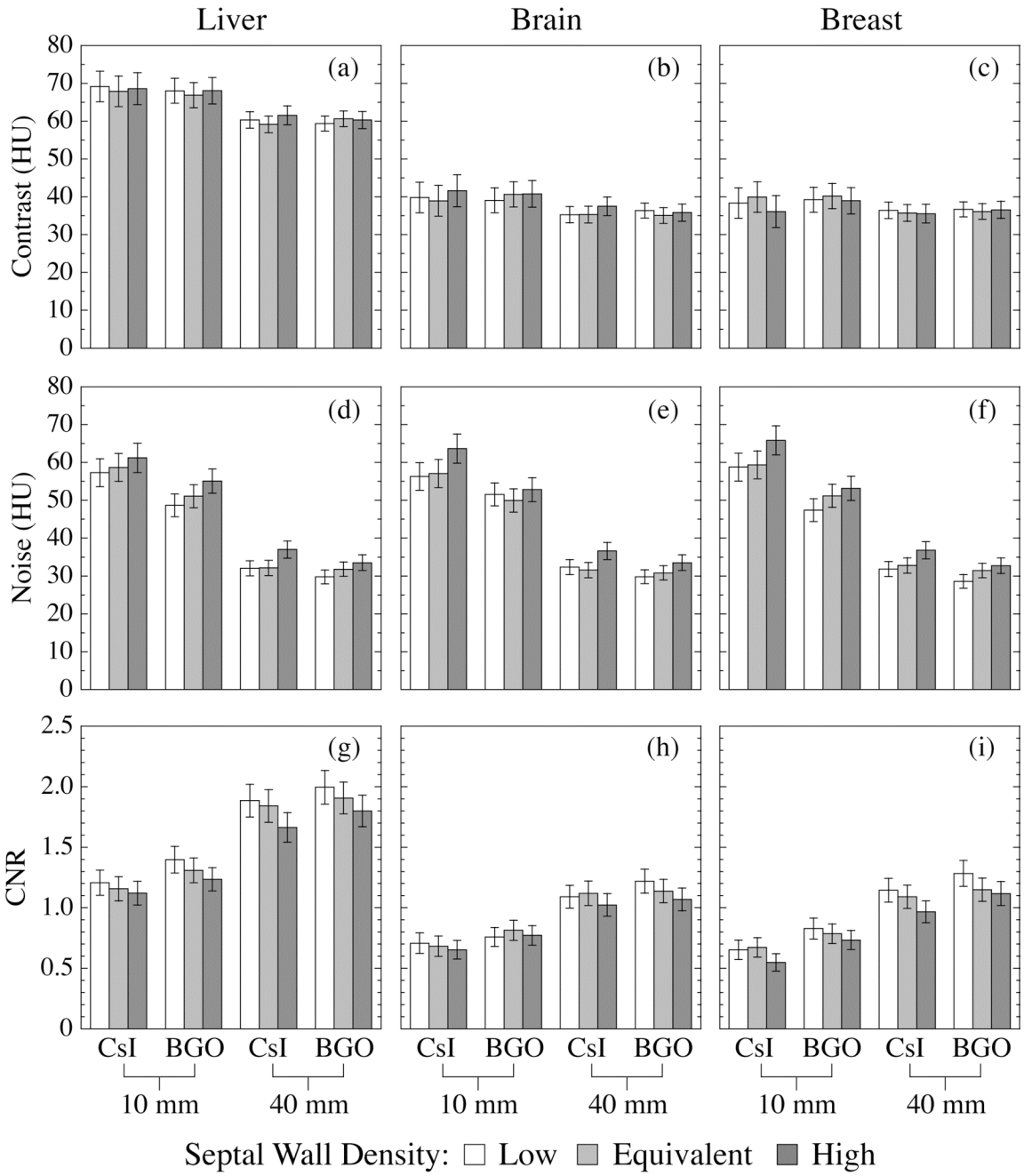

Figure 5.8. Contrast, Noise and CNR results for the liver-, brain- and breast-equivalent objects obtained using the various segmented scintillating detectors. In each figure, the results obtained using the detectors with the same scintillator material and thickness (but different septal wall material) are illustrated in one group. In each group, detectors with different septal walls are indicated by columns with different shadings.

similar for the brain- and breast-equivalent materials. Moreover, for a given object, the results obtained using the 40 mm thick detectors are slightly lower than that obtained

using the 10 mm thick detectors. This slight degradation is likely due to the higher radiation crosstalk in the thicker detectors. Furthermore, with a specific scintillator thickness, the Contrast of a given object is very similar for detectors employing different scintillator and wall materials. As shown in Figs. 5.8(d), 5.8(e) and 5.8(f), the level of Noise performance is mainly determined by the detector properties, rather than the object properties. The Noise values obtained using the same detector are almost the same for the three objects, within the range of statistical uncertainty. For each object, Noise is generally lower for detectors with larger scintillator thickness, higher scintillator density (i.e., BGO) and lower septal wall density. In particular, it is interesting to find that although the use of higher-density walls allows the detector to sample more X rays (i.e., higher QE), which improve statistics, it results in generally higher levels of Noise. This behavior is likely to be the result of the lower level of radiation crosstalk that reduces the detector element-to-element signal correlation. As observed from Figs. 5.8(g), 5.8(h) and 5.8(i), the CNR results are generally higher for objects having greater RED difference from the background, as well as for detectors with larger scintillator thickness, higher scintillator density and lower septal wall density.

Figure 5.9 illustrates the CNR^2 results for the liver-equivalent object obtained at 3.08 cGy as a function of DQE_{RAD} at zero spatial frequency (obtained from a previous Monte Carlo study of radiation transport).[8] The results are shown for 10 and 40 mm thick BGO and CsI:Tl detectors with low- and high-density septal walls. CNR^2 is observed to increase with increasing DQE_{RAD} for detectors having a specific type of septal walls. However, this increase does not follow a linear pattern. For detectors at a given thickness

and employing a specific scintillator material (*e.g.*, 40 mm BGO detectors), the use of higher-density septal walls results in a lower value of CNR^2, despite providing a higher value of DQE_{RAD}. This behavior is the result of the greater radiation attenuation provided by the higher-density walls. On the one hand, the greater attenuation results in higher QE, leading to a better DQE_{RAD} performance.[8] On the other hand, the greater attenuation also limits the lateral spread of the radiation and reduces the effect of statistical averaging, resulting in larger variation of the voxel signals in the reconstructed image (*i.e.*, $Noise^2$), and thus lower CNR^2.

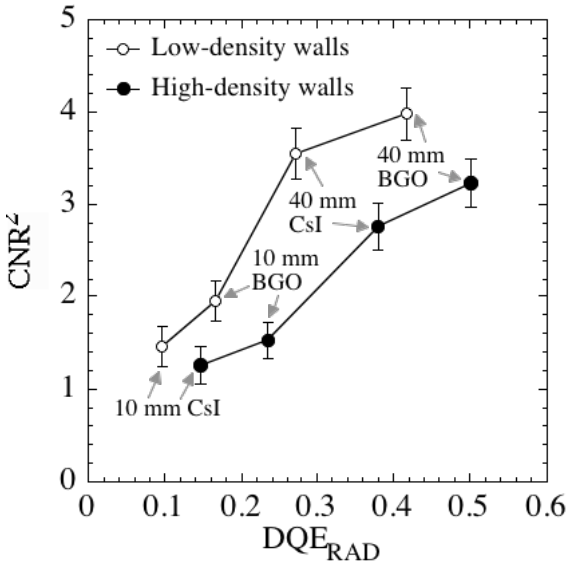

Figure 5.9. CNR^2 results for the liver-equivalent object plotted as a function of zero-frequency DQE_{RAD}. These results were obtained using the segmented detectors with low- and high-density septal walls. The scintillator thickness and scintillator material are indicated for each detector. The lines joining the data points are drawn to guide the eye.

Figure 5.10 shows reconstructed images corresponding to the results shown in Fig. 5.8. All three objects are clearly visible in all images. Moreover, the visibility of the objects improves with increasing detector thickness and scintillator density, and with decreasing septal wall density, in line with the CNR results illustrated in Fig. 5.8.

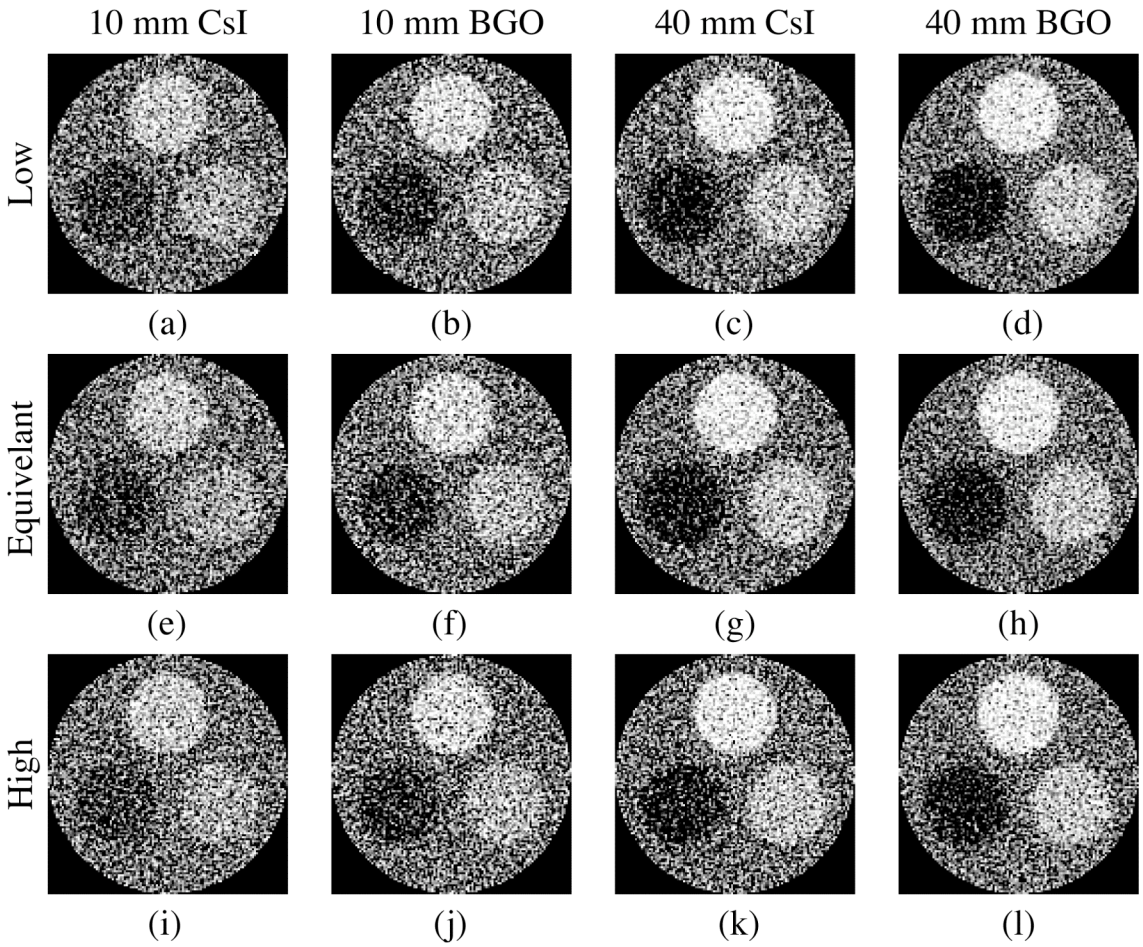

Figure 5.10. Reconstructed images of the three-object phantom obtained using various segmented detectors at 3.08 cGy. Each column represents detectors with a given scintillator material and thickness, whereas each row represents detectors with a given type of septal wall density (*i.e.*, "Low", "Equivalent" and "High"). The same window and level were selected for the images in the same column, whereas different window and level were selected for different columns to maximize the objects visibility.

4. Segmented detectors versus phosphor screen

The three-object phantom was also scanned by a phosphor screen detector, which is representative of the x-ray detector used in conventional EPIDs, at doses up to ~102 cGy. In Fig. 5.11, the results of CNR^2 for the liver-equivalent object are plotted as a function of dose for the 40 mm thick, segmented CsI:Tl detector with low-density septal walls and the phosphor screen detector. The slope of the linear fit to the data, representing the

increasing rate of CNR^2 with increasing dose, is ~49 times steeper for the segmented detector (1.121 cGy^{-1}) compared to the phosphor screen detector (0.023 cGy^{-1}). In order to provide a visual comparison for the reader, reconstructed images obtained using the segmented and the phosphor screen detector at 4.62 cGy are shown in Fig. 5.12. As seen in the figure, the segmented detector can provide impressive visibility for all three objects, while the phosphor screen detector does not provide visibility of any of the three objects at this dose level.

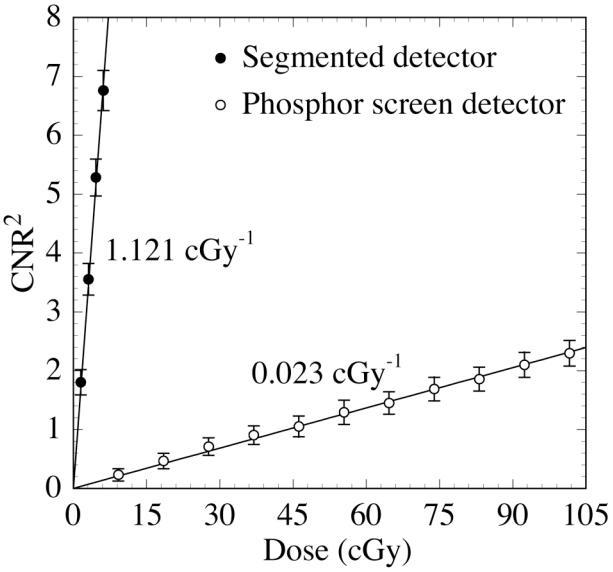

Figure 5.11. CNR^2 results for the liver-equivalent object as a function of dose. Results for the 40 mm thick CsI:Tl detector with low-density septal walls are compared to that for the phosphor detector. The solid lines indicate linear fits to the data. The slope of the linear fit, representing the sensitivity of CNR^2 to dose, is shown for each detector.

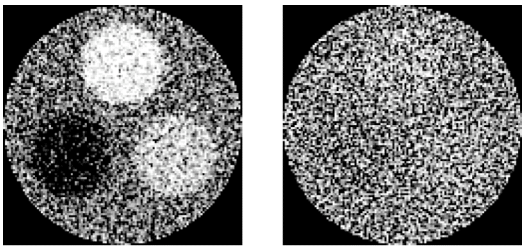

(a) (b)

Figure 5.12. Reconstructed images of the three-object phantom obtained at 4.62 cGy using (a) the 40 mm thick CsI:Tl detector with low-density septal walls and (b) the phosphor screen detector.

In Fig. 5.13, for the liver-equivalent object, the CNR^2 performance of all segmented detectors obtained at 1.54 cGy is compared to that obtained using the phosphor screen detector at higher doses. Note that the performance of the phosphor screen detector, represented by the solid line, corresponds to the linear fit to the phosphor screen detector results in Fig. 5.11, and is plotted as a function of dose (bottom x-axis scale). The values of CNR^2 for the various segmented detectors at the constant dose (cross symbols) have been positioned along the x-axis direction so as to overlie the phosphor screen detector performance curve. With this plotting convention, the dose reduction for a segmented detector offering CNR^2 performance equivalent to the phosphor screen detector is determined by the ratio of the dose requirement for the phosphor screen detector to achieve this specific CNR^2 to the constant dose of 1.54 cGy. Such dose reduction is shown by the top x-axis scale. For example, in order to achieve a CNR^2 value equivalent to that provided by the 40 mm thick, segmented BGO detector with low-density septal walls at 1.54 cGy, the phosphor screen detector requires a dose of ~90 cGy. Thus, if the phosphor screen detector were replaced by such a segmented detector, ~59 times less dose would be required to achieve an equivalent value of CNR^2.

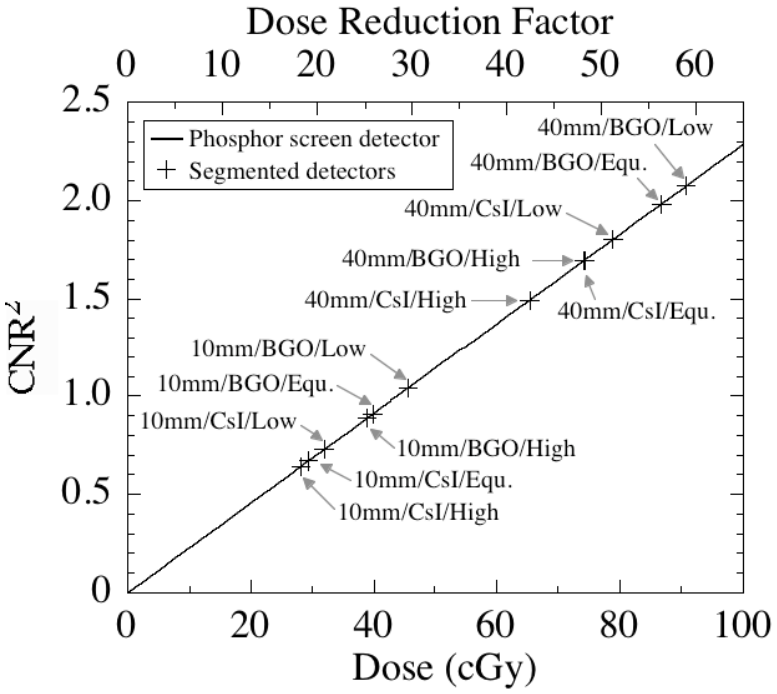

Figure 5.13. Results for CNR^2 obtained using the various segmented detectors at 1.54 cGy compared to that obtained using the phosphor screen detector at higher doses. The solid line represents the CNR^2 of the phosphor screen plotted as a function of dose (bottom x-axis scale). The cross symbols, which represent the CNR^2 values obtained using the segmented detectors at 1.54 cGy, are positioned along the x-axis direction so as to fall on the phosphor screen performance line. Thus the degree of dose reduction offered by the segmented detectors compared to the phosphor screen is represented by the top x-axis scale. The design parameters of the segmented detectors are indicated in the form of "scintillator thickness/ scintillator material/ septal wall density". Note that "Low", "Equ." and "High" refer to the low-, equivalent- and high-density walls. Also, the results for "40mm/BGO/High" and "40mm/CsI:Tl/Equ." almost overlap.

IV. DISCUSSION

This chapter presents a theoretical evaluation of the performance of thick, segmented scintillating detectors for the visualization of low contrast, soft tissues using MV CBCT at clinically acceptable doses (i.e., a few cGy) for a 6 MV x-ray energy spectrum. Reconstructed images of a water phantom embedded with various tissue-equivalent objects were obtained through simulation of energy deposition in the scintillating material. Contrast, Noise and CNR were examined as a function of reconstructed slice

thickness, total scan dose, relative electron density of the tissue-equivalent materials and various design parameters of segmented scintillators. The performance of the various scintillator designs obtained at a relatively low dose (1.54 cGy) was compared to that of the phosphor screen detector.

Within the limitation of this study (which is discussed below), the results indicate that the Contrast of a tissue-equivalent object is mainly determined by the difference in relative electron density between the object and the water background, due to the dominant effect of Compton scattering at megavoltage energies. The Contrast is not affected by the scintillator and septal wall materials, but degrades slightly for thicker scintillators. In addition, for the low contrast tissue-equivalent objects examined in this work, and for a given detector, the Noise results appear to be independent of the relative electron density within the range of statistical uncertainty. For the tissue-equivalent objects, the CNR^2 results exhibit an approximately linear increase with increasing slice thickness and scan dose, due to the reduced $Noise^2$ values as a result of the increasing number of X rays sampled. With the same slice thickness and scan dose, the segmented detectors with greater thickness, higher scintillator density, or lower septal wall density result in lower Noise, which helps to enhance CNR. As shown in the reconstructed images, for the size of the phantoms studied, a 40 mm thick, segmented CsI:Tl detector with low-density septal walls allows resolution of relative electron density differences of ~2.3% and 1.3% at 1.54 and 3.08 cGy, respectively. Also, all examined segmented detectors can delineate ~3.3% relative electron density difference at 3.08 cGy. In addition, the results indicate that, for a phosphor screen detector to achieve the same

CNR^2 performance as the segmented detectors, ~18 to 59 times more dose is required, depending on the design of the segmented scintillator.

Due to constraints imposed by the Monte Carlo codes as explained in Sec. II.B, the simulated contrast phantoms have a relatively small size of ~6 cm in diameter. Larger phantoms would result in more radiation attenuation and scatter, which is expected to degrade CNR performance, so that a higher dose would be required to maintain the same performance obtained from the smaller phantoms. Nevertheless, it is believed that, had a larger phantom been used, the CNR performance of the segmented detectors relative to the phosphor screen detector would not be significantly affected, since the degree of radiation attenuation and scattering are largely determined by the phantom.

The simulations reported in this chapter did not include optical transport, which would affect the CNR performance predicted by radiation transport. On the one hand, the inevitable optical Swank noise would increase Noise resulting in reduced CNR. On the other hand, the presence of any lateral optical spreading would increase the correlation of pixel signals, which leads to blurring and reduced levels of Noise that improves CNR. Although the direct inclusion of optical transport in the MV CBCT simulations is not feasible given the computational resources available at the time of this dissertation work, it might be possible to develop an analytical model to include the effect of optical Swank noise and lateral optical spreading in the CNR results.

REFERENCES

[1] Y. Wang, L. E. Antonuk, Y. El-Mohri, Q. Zhao, A. Sawant and H. Du, "Monte Carlo investigations of megavoltage cone-beam CT using thick, segmented scintillating detectors for soft tissue visualization," Medical Physics **35**, 145-158 (2008).

[2] I. Kawrakow and D. W. O. Rogers, "The EGSnrc Code System: Monte Carlo Simulation of Electron and Photon Transport," Ottawa, Canada (2000).

[3] J. A. Treurniet, B. R. B. Walters and D. W. O. Rogers, "BEAMnrc, DOSXYZnrc and BEAMDP GUI User's Manual," Ottawa, Canada (2001).

[4] D. Sheikh-Bagheri, Ph.D. Thesis, Carleton University, 1999.

[5] M. K. Yu, R. S. Sloboda and B. Murray, "Linear accelerator photon beam quality at off-axis points," Med Phys **24**, 233-239 (1997).

[6] L. E. Antonuk, Y. El-Mohri, W. Huang, K.-W. Jee, J. H. Siewerdsen, M. Maolinbay, V. E. Scarpine, H. Sandler and J. Yorkston, "Initial Performance Evaluation of an Indirect-Detection, Active Matrix Flat-Panel Imager (AMFPI) Prototype for Megavoltage Imaging," Int. J. Rad. Onc. Biol. Phys. **42**, 437-454 (1998).

[7] A. Sawant, L. E. Antonuk, Y. El-Mohri, Q. Zhao, Y. Wang, Y. Li, H. Du and L. Perna, "Segmented Crystalline Scintillators: Empirical and Theoretical Investigation of a High Quantum Efficiency EPID Based on an Initial Engineering Prototype CsI(Tl) Detector," Medical Physics **33**, 1053-1066 (2006).

[8] A. Sawant, L. E. Antonuk, Y. El-Mohri, Q. Zhao, Y. Li, Z. Su, Y. Wang, J. Yamamoto, H. Du, I. Cunningham, M. Klugerman and K. Shah, "Segmented Crystalline Scintillators: An Initial Investigation of High Quantum Efficiency Detectors for Megavoltage X-Ray Imaging," Medical Physics **32**, 3067-3083 (2005).

[9] L. E. Antonuk, "Electronic portal imaging devices: A review and historical perspective of contemporary technologies and research," Phys. Med. Biol. **47**, R31-R65 (2002).

[10] "Data sheet of tissue characterization phantom (Gammex 467)," Wisconsin, U.S. (2006).

[11] International Commission on Radiation Units and Measurements (ICRU) Report 46, "Photon, Electron, Proton and Neutron Interaction Data for Body Tissues," Bethesda, Maryland, U.S. (1992).

[12] G. H. Glover, "Compton scatter effects in CT reconstructions," Medical Physics **9**, 860-867 (1982).

[13] R. Ning, B. Chen, R. Yu, D. Conover, X. Tang and Y. Ning, "Flat panel detector-based cone-beam volume CT angiography imaging: system evaluation," IEEE Trans. Med. Imaging **19**, 949-963 (2000).

[14] S. A. Graham, D. J. Moseley, J. H. Siewerdsen and D. A. Jaffray, "Compensators for dose and scatter management in cone-beam computed tomography," Medical Physics **34**, 2691-2703 (2007).

[15] M. Kachelriess, K. Sourbelle and W. A. Kalender, "Empirical cupping correction: a first-order raw data precorrection for cone-beam computed tomography," Medical Physics **33**, 1269-1274 (2006).

[16] L. A. Feldkamp, L. C. Davis and J. W. Kress, "Practical cone-beam algorithm," Journal of the Optical Society of America A: Optics, Image Science, and Vision **1**, 612–619 (1984).

[17] R. H. Huesman, "The effects of a finite number of projection angles and finite lateral sampling of projections on the propagation of statistical errors in transverse section reconstruction," Phys. Med. Biol. **22**, 511-521 (1977).

CHAPTER 6

SUMMARY AND CONCLUSIONS

The development of high-DQE, AMFPI-based electronic portal imaging devices (EPIDs) is motivated by the desire to obtain soft-tissue information in the treatment room so as to help ensure the accurate execution of radiotherapy plans for 3D conformal radiation therapy and intensity modulated radiation therapy. In order to achieve high DQE performance, two detector approaches, involving the use of PIB-HgI_2 photoconductors and segmented crystalline scintillators, have been investigated in the research associated with this dissertation. Both approaches aim to significantly improve DQE through greatly increasing QE, while preserving (or even improving) MTF and limiting Swank noise.

The potential performance of hypothetical EPIDs employing HgI_2 photoconductors up to 6 mm thick was examined in Chapter 2 through Monte Carlo simulation of radiation transport. The results indicate that such direct detection EPIDs could potentially provide better MTF and up to ~5 times higher DQE than conventional EPIDs.

In Chapter 3, Monte Carlo simulations of radiation and optical transport were used to study the optical Swank factor (I_{OPT}) and zero-spatial frequency DQE for hypothetical

EPIDs employing segmented BGO and CsI:Tl scintillators up to 40 mm thick. These metrics were examined as a function of various geometric, material and optical properties. The results indicate that I_{OPT} and DQE are strongly affected by the aspect ratio of the scintillating crystals (ϕ_{SCI}), the optical absorptivity at the septal walls (α_{WALL}) and the roughness of the side surfaces of the scintillating crystals (θ_{MAX}). It is also found that 40 mm thick segmented CsI:Tl and BGO scintillators with optimum optical properties could potentially provide DQE values up to ~29% and 42%, respectively, assuming an element-to-element pitch of 1.016 mm and a septal wall thickness of 0.05 mm.

Four newly constructed prototype segmented scintillators were evaluated using a 6 MV photon beam. The scintillators include an 11.3 mm thick BGO scintillator and three CsI:Tl scintillators, referred to as CsI-1, CsI-2 and CsI-3, with thicknesses of 11.4, 25.6 and 40.0 mm, respectively. The BGO prototype exhibits DQE values of ~20% at zero frequency and ~5% at the Nyquist frequency, which are ~20 and 10 times higher than those of the conventional EPID, respectively. Also, this prototype showed an MTF of ~20% at the Nyquist frequency. As a result of the significantly improved DQE and reasonable spatial resolution, this prototype allowed visualization of low-contrast objects with distinguishable boundaries with only 1 LINAC beam pulse (0.022 cGy). The three CsI:Tl prototypes also showed significantly higher DQE than the conventional EPID at low frequencies. However, the MTF and DQE of these prototypes decline significantly at higher frequencies due to significant lateral optical spreading. While these prototypes

facilitated visualization of low-contrast objects at 1 beam pulse, the corresponding images are more blurred due to poorer spatial resolution compared to the BGO prototype.

The potential of thick, segmented BGO and CsI:Tl scintillators for visualizing soft tissues via MV CBCT was examined using Monte Carlo simulations of radiation transport. The CNR of the various tissue-equivalent objects was studied as a function of reconstructed slice thickness, total scan dose, electron density of the object relative to that of water, scintillator material and thickness, as well as septal wall material. The results demonstrate that higher CNR is observed for scintillators with higher density (i.e., BGO) and greater thickness, as well as lower-density septal walls. Hypothetical, MV CBCT systems employing 10 and 40 mm thick segmented CsI:Tl scintillators enable delineation of soft tissue objects with a relative electron density difference of ~2% using doses of ~3 and ~1.5 cGy, respectively. Moreover, higher CNR performance was observed for the BGO scintillators compared to their CsI:Tl counterparts. In addition, for the segmented scintillators to achieve the same CNR performance as the phosphor screen detector used in conventional EPIDs, ~18 to 59 times less dose is required, depending on the design of the segmented scintillator.

Future work on thick, segmented crystalline scintillators will involve the improvement of spatial resolution and DQE at high spatial frequencies through reduction of lateral optical spreading. This can be achieved by using more opaque polymer reflectors (e.g., with greater thickness) or by replacing polymer reflectors with metal reflectors. However, such modifications of septal walls must not result in a significant

increase in optical Swank noise, which would degrade DQE at all spatial frequencies. In addition, further improvement in the alignment between scintillator elements would facilitate more accurate registration between the segmented scintillator and the underlying flat-panel array, thus improving spatial resolution. In general, it is more difficult to align scintillator elements having thicker septal walls. Therefore, for future scintillators that employ thicker walls for better optical isolation, it will be necessary to improve fabrication techniques so as to, at a minimum, preserve the degree of element alignment that was achieved for the prototype scintillators reported in this dissertation.

In conclusion, the results reported in this dissertation support the hypothesis that EPIDs employing thick PIB-HgI_2 photoconductors and thick, segmented BGO and CsI:Tl scintillators can both provide much higher DQE compared to conventional EPIDs that are based on phosphor screen detectors. Perhaps most encouragingly, a prototype EPID employing a segmented BGO scintillator demonstrated impressive imaging performance at extremely low doses. It is anticipated that, using such novel EPIDs offering significantly improved DQE, MV CBCT with soft-tissue visualization will be achieved at clinically practical doses of a few cGy, which is approximately equal to the dose of one or two portal images.

APPENDICES

APPENDIX A

INPUT AND OUTPUT FILES FOR MANTIS

This appendix describes the input and output files used in MANTIS. Although such information can be found in the MANTIS tutorial and manual, a brief summary is presented to assist the user of this code.

I. INPUT FILES

The MANTIS code uses a number of files to define input parameters for the radiation and optical simulations. For a simulation named as "SIM", there is one SIM.geo file defining the geometry for both radiation and optical simulations. Note that the SIM.geo file only defines the spatial geometry of each material (e.g., MAT_i) with no information about the voxels within this material. Other input files will allow a block of material to be further divided into voxels. The radiation cross-section data for all materials used in the simulation are included in one SIM.mat file. For each of the materials (e.g. MAT_i), a MAT_i.dm2 file is used to define optical properties, including refractive index, optical absorption coefficient (μ_A) and an optical scattering coefficient (μ_S). Input parameters for the radiation simulation (e.g., energy spectrum and cut-off energies of quanta) are defined in a SIM.pen file, which also specifies the output from the radiation simulation (e.g., spectral and spatial distributions of the energy absorption). Input parameters for the

optical simulation are defined in five different files (i.e., SIM.d2c, SIM.d2d, SIM.d2m, SIM.d2s and SIM.d2x). The SIM.d2c file defines the optical gain of the scintillator, the model of light generation, the absorptivity of optical surfaces, and the pitch of the photodiode array. The SIM.d2d file defines the optical absorption spectrum of the photodiode material. The SIM.d2m file lists the various material files for the optical simulation (e.g., MAT_i.dm2). In this list, the first and second materials (MAT_1 and MAT_2) are dedicated to the scintillator and photodiode, respectively. Note that version 2.0 of the MANTIS code only allows one scintillator material and one photodiode material to be defined. The SIM.d2s file defines the optical surfaces between any two materials (see Sec. II.C. in Chapter III for details about the surface models). Finally, the SIM.d2x file specifies the emission spectrum of the scintillator.

II. OUTPUT FILES

The standard outputs from MANTIS simulations include the spectral and spatial distribution of the energy deposition, the absorbed energy distribution, the spatial distribution of the detected optical photons, the record for each step of radiation and optical transport for the first several histories (e.g., 5), as well as a simulation log file. Note that recording the detailed paths for too many histories will prohibitively slow down the simulation. In addition, for purposes of the study presented in Chapter III, two customized output files are generated, reporting the amount of energy absorbed in the scintillator, as well as the number of optical photons detected in the entire photodiode array, for each interacting X ray. These values are used to generate the absorbed energy distribution (AED) and pulse height distribution (PHD). For each x-ray history, the

number of light photons detected per unit absorbed energy is determined from the two customized outputs (calculated as the number of optical photons detected in the photodiode array divided by the amount of energy absorbed in the scintillator). This information is used to generate the optical pulse distribution (OPD).

APPENDIX B

PARALLEL PROCESSING FOR MANTIS SIMULATIONS

Version 2.0 of the MANTIS code is not adapted for parallel processing. A series of MATLAB codes were developed by the author so as to allow generation and submission of parallel jobs, as well as to combine parallel simulation results. For each simulation (for example, named as "SIM"), a code was used to generate a user specified number of .pen files (e.g., SIM_job1.pen, SIM_job2.pen, and etc.). Each .pen file corresponds to the simulation of a fraction of the total x-ray histories, with a unique pair of starting random numbers. All other input parameters are the same for all the jobs for the same simulation. In order to submit a job (e.g, SIM_job1) to a computer cluster, a SIM_job1.pbs file is generated, which specifies the queue on the cluster, the number of node requested, the length of the job, and the path of the executable code (i.e., MANTIS.exe file). For each simulation (e.g., SIM), a SIM.par file is generated so as to allow all jobs (e.g., SIM_job1) to be submitted to the cluster. Finally, after completion of all jobs, the simulated AED and PHD are combined.

APPENDIX C

VALIDATION OF USING REDUCED CONVERSION GAIN FOR THE OPTICAL SWANK NOISE STUDY

This appendix describes the conditions under which, in the present study, a 90% reduction in the conversion gain for CsI:Tl detectors will still lead to a correct determination of I_{OPT}. In the MANTIS simulations, an X ray deposits its energy in the scintillator in multiple (k) steps. Each energy deposition, E_k, generates N_k optical photons, as determined by the conversion gain and Eq. (3.3). For each interacting X ray, the total energy absorbed in the scintillator, E_A, is given by:

$$E_A = \sum_k E_k, \tag{C.1}$$

while the total number of optical photons generated, N_G, is given by:

$$N_G = \sum_k N_k. \tag{C.2}$$

Due to light loss in the x-ray detector, only a fraction, η, of the N_G optical photons are detected in the photodiode array. (η is referred to as the optical detection efficiency.) Therefore, for each interacting X ray, the number of optical photons detected, N_D, is given by:

$$N_D = \eta \times N_G, \tag{C.3}$$

so that the number of optical photons detected per unit of energy absorbed in the scintillator, N_E, may be determined from:

$$N_E = N_D / E_A . \tag{C.4}$$

As indicated in the Methods section, the distribution of N_E, $P(N_E)$, referred to as the optical pulse distribution, is used to determine I_{OPT} by means of Eqs. (1.3) and (1.4). By substituting Eqs. (3.3), (C.1), (C.2) and (C.3) into Eq. (C.4), N_E may be expressed in terms of η, E_k and G as follows:

$$N_E = \frac{\eta \times \sum_k \left(Poisson\left[Round[E_k \times G] \right] \right)}{\sum_k E_k}. \tag{C.5}$$

Since MANTIS rounds the product $E_k \times G$ to the nearest integer before generating light photons, the use of reduced conversion gain for CsI:Tl (i.e., $G = 0.1 \times G_{CsI:Tl}$) may result in a reduction in N_G greater than the intended 90%. This additional loss in N_G occurs when $0.5 \le (E_k \times G) < 5$. For this range of $E_k \times G$ values, while the nominal gain will result in generation of a few optical photons (i.e., 1 to 5), the reduced gain will lead to the generation of no light photons (since $E_k \times 0.1 \times G$ is rounded to zero). Therefore, in order to achieve the intended 90% reduction in N_G, the probability of $0.5 \le (E_k \times G) < 5$ must be negligible.

It is of interest to note that, when the nominal gain for the CsI:Tl detectors is used (i.e., when $G = G_{CsI:Tl}$), N_G is found to be very large (~40,000 to 110,000), resulting in a very small statistical uncertainty for η (~0.3% to 0.5%). This uncertainty remains small (~1.0% to 1.6%) even when N_G is reduced by 90%. Therefore, if N_G is reduced by the intended 90% when reduced gain is used, N_E will also be reduced by ~90% as intended (given that the value of η will remain relatively unchanged). As a result of the reduction

in N_E, the first and second order moments of $P(N_E)$, M_1 and M_2, will be reduced to 10% and 1% of their original values, respectively. As can be seen from Eq. (1.3), since the value of M_0 remains unchanged, the effect of such reductions in M_1 and M_2 will cancel out, leaving the value of I_{OPT} unchanged.

In summary, in order to demonstrate the validity of using reduced gain, it is necessary to show that the probability of $0.5 \le (E_k \times G) < 5$ is not high enough to affect the determination of I_{OPT}. For each CsI:Tl detector design (i.e., for a collection of CsI:Tl detector configurations offering the same radiation transport properties and the same value of G), such validation can consist of comparing I_{OPT} values determined from simulations using the nominal and reduced gain. This comparison only needs to be performed for one configuration of each design, since the value of $E_k \times G$ is the same for all configurations of that design.

APPENDIX D

ERROR ANALYSIS FOR THE MV CBCT STUDY

For a Monte Carlo simulation using a given detector and phantom combination, the statistical uncertainty in the signal of voxels in a reconstructed image ($\Delta\mu$) can be estimated from the statistical uncertainties in the signal of pixels in projection images (ΔI), using a previously described method.[1] The Monte Carlo simulation outputs the pixel signal ($I(x,y,\theta)$) and the relative statistical uncertainty ($\frac{\Delta I(x,y,\theta)}{I(x,y,\theta)}$) associated with that signal for a projection image, where x and y are the coordinates of the pixel and θ is the projection angle. It is found that, for a given projection image, the values of $\frac{\Delta I(x,y,\theta)}{I(x,y,\theta)}$ were relatively similar for all the pixels in the region of interest. Therefore, a mean value of statistical uncertainty ($\frac{\Delta I(\theta)}{I(\theta)}$), obtained by averaging $\frac{\Delta I(x,y,\theta)}{I(x,y,\theta)}$ for all the pixels in the region of interest, was used to represent the statistical uncertainty for all the pixels in this projection image. Also, it is observed that, at all projection angles, the values of $\frac{\Delta I(\theta)}{I(\theta)}$ were almost identical. Therefore, a mean value of statistical uncertainty ($\frac{\Delta I}{I}$), obtained by averaging $\frac{\Delta I(\theta)}{I(\theta)}$ for all the projection angles, was used to represent

the statistical uncertainty in the pixel signals in the projection images at all the angles for this simulation.

The line integral (l), as shown in Eq. (5.2), was obtained from the phantom image signal (I_1) and the averaged flood-field image signal (I_0). Due to the effect of this averaging, the relative statistical uncertainty in I_0 is much smaller than that in I_1. Therefore, the statistical uncertainty in the line integrals (Δl) can be estimated from:[2]

$$\Delta l = \Delta\left(\ln\frac{I_0}{I_1}\right) = \frac{\Delta\left(\frac{I_0}{I_1}\right)}{\frac{I_0}{I_1}} = \sqrt{\left(\frac{\Delta I_0}{I_0}\right)^2 + \left(\frac{\Delta I_1}{I_1}\right)^2} \approx \frac{\Delta I_1}{I_1}. \tag{D.1}$$

As shown in Eq. (13) of Ref. 1, the root mean square error of the reconstructed voxel signal ($\Delta\mu$) can be expressed using the statistical uncertainty in the line integrals:

$$\Delta\mu = \sqrt{\frac{1.59 \times D}{n \times d^3}} \times \Delta l, \tag{D.2}$$

where D is the diameter of the reconstructed cylinder (60.96 mm), d is the voxel pitch in the reconstructed image (0.508 mm), and n is the number of coplanar paths, which is equal to the product of the number of projections (180) and the number of AMFPI pixels covering the phantom in the scanning direction (128). With these parameter values and using Eq. (D.1), Eq. (D.2) becomes:

$$\Delta\mu = 0.179 \times \frac{\Delta I_1}{I_1}. \tag{D.3}$$

In this study, multiple reconstructed slices were averaged to obtain better statistics. The statistical uncertainty in an averaged slice image ($\Delta\mu_s$) can be expressed as:

$$\Delta\mu_s = \frac{\Delta\mu}{\sqrt{n_s}} = \frac{0.179}{\sqrt{n_s}} \times \frac{\Delta I_1}{I_1}, \tag{D.4}$$

where n_s is the number of slices averaged.

In addition, the cupping artifact was removed in the averaged slice image using the correction factors $\mu_c(r)$, where r is the radial distance from the center of the phantom. The statistical uncertainty in these correction factors [$\Delta\mu_c(r)$] can be expressed as:

$$\Delta\mu_c(r) = \frac{\Delta\mu_s}{\sqrt{n_c(r)}} = \frac{0.179}{\sqrt{n_c(r) \times n_s}} \times \frac{\Delta I_1}{I_1}, \tag{D.5}$$

where $n_c(r)$ is the number of voxels averaged for obtaining the correction factor at a radial distance r. In the region selected for evaluation, $n_c(r)$ is at least 32, resulting in values for $\Delta\mu_c(r)$ that are much smaller than for $\Delta\mu_s$. The statistical uncertainty in the voxel signal after cupping artifact removal ($\Delta\mu_{vox}$) can be estimated from $\Delta\mu_s$ and $\Delta\mu_c(r)$:

$$\Delta\mu_{vox} = \sqrt{(\Delta\mu_s)^2 + [\Delta\mu_c(r)]^2} \approx \Delta\mu_s = \frac{0.179}{\sqrt{n_s}} \times \frac{\Delta I_1}{I_1}. \tag{D.6}$$

Therefore, the statistical uncertainties in the mean signal of water background ($\Delta\mu_{water}$) and object ($\Delta\mu_{obj}$) can be expressed as:

$$\Delta\mu_{water} = \frac{\Delta\mu_{vox}}{\sqrt{n_{water}}} = \frac{0.179}{\sqrt{n_s \times n_{water}}} \times \frac{\Delta I_1}{I_1} \tag{D.7}$$

and

$$\Delta\mu_{obj} = \frac{\Delta\mu_{vox}}{\sqrt{n_{obj}}} = \frac{0.179}{\sqrt{n_s \times n_{obj}}} \times \frac{\Delta I_1}{I_1}, \tag{D.8}$$

where n_{water} and n_{obj} are the number of voxels in the region of the water background and the object, respectively. Note that n_{water} is equal to 7756 for the one-object phantom and 4508 for the three-object phantom, while n_{obj} is equal to 912 for all the examined objects. Moreover, the statistical uncertainty of the standard deviation of the voxel signals in the region of the object ($\Delta\sigma_{obj}$) can be expressed as:

$$\Delta\sigma_{obj} = \Delta\sqrt{\frac{\sum_{i=1}^{n_{obj}}(\mu_i - \bar{\mu})^2}{n_{obj} - 1}} = \frac{\Delta\mu_{vox}}{\sqrt{n_{obj} - 1}} = \frac{0.179}{\sqrt{n_s \times (n_{obj} - 1)}} \times \frac{\Delta I_1}{I_1}. \tag{D.9}$$

The relative error in the *Contrast* of the object can be expressed as:

$$\frac{\Delta Contrast}{Contrast} = \sqrt{\frac{(\Delta\mu_{obj})^2 + (\Delta\mu_{water})^2}{(\mu_{obj} - \mu_{water})^2} + \left(\frac{\Delta\mu_{water}}{\mu_{water}}\right)^2}. \tag{D.10}$$

Furthermore, the relative error in the *Noise* in the region of the object can be expressed as:

$$\frac{\Delta Noise}{Noise} = \sqrt{\left(\frac{\Delta\sigma_{obj}}{\sigma_{obj}}\right)^2 + \left(\frac{\Delta\mu_{water}}{\mu_{water}}\right)^2}. \tag{D.11}$$

Finally, the relative error in the *CNR* of the object can be expressed as:

$$\frac{\Delta CNR}{CNR} = \sqrt{\frac{(\Delta\mu_{obj})^2 + (\Delta\mu_{water})^2}{(\mu_{obj} - \mu_{water})^2} + \left(\frac{\Delta\sigma_{obj}}{\sigma_{obj}}\right)^2}. \tag{D.12}$$

REFERENCES

[1] R. H. Huesman, "The effects of a finite number of projection angles and finite lateral sampling of projections on the propagation of statistical errors in transverse section reconstruction," Physics in Medicine and Biology **22**, 511-521 (1977).

[2] J. R. Taylor, *An Introduction to Error Analysis: The Study of Uncertainties in Physical Measurements*, 2nd ed. (University Science Books, California, 1997).